AN ENGINEERING APPROACH TO DIRECT AND CHARACTERIZE THE STRUCTURE OF CARDIAC TISSUE

by

Richard Allen Lasher

A dissertation submitted to the faculty of
The University of Utah
in partial fulfillment of the requirements for the degree of

Doctor of Philosophy

Department of Bioengineering

University of Utah

May 2012

The University of Utah Graduate School

STATEMENT OF DISSERTATION APPROVAL

The dissertation of **Richard Allen Lasher**

has been approved by the following supervisory committee members:

Robert Hitchcock	, Chair	**12-13-2011** Date Approved
Frank Sachse	, Member	**12-13-2011** Date Approved
David Grainger	, Member	**12-14-2011** Date Approved
Patrick Tresco	, Member	**12-13-2011** Date Approved
Alonso Moreno	, Member	**12-13-2011** Date Approved

and by **Patrick Tresco**, Chair of the Department of **Bioengineering**

and by Charles A. Wight, Dean of The Graduate School.

ABSTRACT

Treatment and management of heart disease is challenging due to the heart's limited ability to self-repair. Although current approaches to manage heart disease, such as pharmacotherapy, medical devices, lifestyle changes, and heart transplantation, have improved and extended the quality of life for millions of individuals, they have inherent shortcomings. Future strategies to manage heart disease will likely be based upon a combination of biological and engineering approaches through cell therapy and tissue engineering strategies, both of which have the potential to regenerate the myocardium and improve cardiac function. However, a key hurdle in applying biological approaches is our limited ability to produce reliable tissue to study disease progression and tissue development, therapeutic intervention, drug discovery, or tissue replacement. Establishing hallmarks of the native myocardium in engineered cardiac tissue is a central goal and appears to be required for creating functional tissue that can serve as a surrogate for *in vitro* testing or the eventual replacement of diseased or injured myocardium. The objective of this research was to apply an engineering approach to develop tools and methods to produce engineered cardiac tissue and characterize both native and engineered cardiac tissue. Three phases of research included: 1) the development and utilization of a framework to characterize microstructure in living cardiac tissue using confocal microscopy and local dye delivery, 2) the development a next-generation bioreactor capable of continuously monitoring force-displacement in engineered tissue,

and 3) the application of confocal imaging and image analysis to quantitatively describe features of the native myocardium, focusing on myocyte geometry and spatial distribution of a major gap junction protein connexin-43, in both engineered tissue and native tissue.

To my wife, Sarim.

TABLE OF CONTENTS

LIST OF TABLES

LIST OF FIGURES

ACKNOWLEDGEMENTS

I gratefully acknowledge my advisor, Dr. Robert Hitchcock, who provided tremendous guidance, insight and support for my research, training and scholarship. I thank my advisory committee members: Drs. Frank Sachse, Patrick Tresco, David Grainger and Alonso Moreno for their contributions, insight and support during my graduate work. I also thank my fellow students Monir Parikh, James Kennedy, Tanner Coleman, Kylee North, Chao Huang, Bettina Schwab and Gustavo Lenis and undergraduate students Aric Pahnke, Jeff Johnson, Daniel Lackey, John Lackey, Eric Carruth, Jacob Andra, Ryan Russon, Mark Sedlacek and Chelsea Mitchell for their contributions to my graduate research. Finally, I thank my family, especially my wife Sarim Lasher, sister Jennifer Short and my parents Richard and Shelly Lasher for their love, support and encouragement.

CHAPTER 1

INTRODUCTION

1.1 Introduction

Heart disease is the number one cause of death in developed countries, accounting for more than 600,000 deaths annually in the United States alone with estimated direct and indirect costs of over $475 billion in 2009 [1]. These high costs place a heavy burden on our society and there are more than 800,000 new cases of myocardial infarction and 550,000 new cases of congestive heart failure diagnosed annually in the United States [1]. Due to the heart's limited capacity to self-repair and restore pump function following injury, treatment and management of heart disease is challenging, especially if diagnosed in late stages.

Current methods for clinical diagnosis, such as magnetic resonance imaging (MRI), computed tomography (CT), ultrasound, endoscopy, and fluoroscopy do not provide real-time cellular-level information on structure and function, which may be essential towards early detection [2]. Current approaches to manage heart disease include pharmaceutical drugs, medical devices, lifestyle changes, and surgical interventions such as heart transplantation [3]. Although these approaches have improved and extended the quality of life for millions of individuals, they have inherent shortcomings. Pharmacotherapy can delay, but not necessarily reverse, the natural course of heart

disease [4]. Commonly, medical devices are only palliative and plagued by biocompatibility and hemocompatibility issues. Organ transplants, the end-stage solution to heart failure, are in short supply for the estimated 6 million individuals living with congestive heart failure and nearly 8 million individuals affected by myocardial infarction [1].

Future strategies to manage and treat heart disease will likely be based upon biological approaches using cell therapy and tissue engineering strategies, both of which have the potential to regenerate the myocardium and improve cardiac function. A key hurdle in applying biological approaches is our limited ability to produce realistic tissue to study disease progression and tissue development, therapeutic intervention, drug discovery, or tissue replacement. Although the field of tissue engineering has moved beyond static two-dimensional (2D) surfaces towards three-dimensional (3D) environments which resemble the *in vivo* space, many shortcomings remain [5]. Some of these shortcomings are related to the need for advanced tissue culture platforms that can control environmental conditions such as mechanical, electrical and chemical factors. Furthermore, there is a need for measurement and analysis techniques to characterize structure and function in both engineered and native tissue. Establishing hallmarks of the native myocardium in engineered tissue appears essential for creating functional tissue that can serve as a surrogate for *in vitro* testing or the eventual replacement of diseased or injured myocardium [6]. Measurement and analysis techniques that provide 3D descriptions of tissue structure will allow for more realistic definition of native tissue which can serve as specifications for engineered tissue.

The overarching objective of this research was to apply an engineering approach to develop tools and methods to produce engineered cardiac tissue and characterize both native and engineered cardiac tissue. The objective was addressed through three phases of research:

1) Develop and utilize a framework to characterize microstructure in living cardiac tissue using confocal microscopy and local dye delivery.
2) Develop a next-generation bioreactor capable of continuously monitoring force-displacement in engineered tissue.
3) Apply confocal imaging and image analysis to quantitatively describe features of the native myocardium, focusing on myocyte geometry and spatial distribution of a major gap junction protein connexin-43 (Cx43), in both engineered tissue and native tissue.

Before describing the work in these research phases, background on cardiac tissue structure and function, heart disease, key approaches in cell therapy and tissue engineering, current state-of-the-art bioreactors and confocal microscopy are reviewed.

1.2 Cardiac Tissue Structure and Function

The heart is a highly metabolically active organ that beats an astonishing 2.5 billion times in an average lifespan. The mammalian heart is comprised of four chambers: two atria, which primarily serve as reservoirs for venous return and two ventricles which pump blood out of the heart (Fig. 1.1a). In many cases of heart disease, the myocardium of the left ventricle is compromised, which results in reduced pump function. The left ventricular myocardium can be viewed as a composite material comprised of fluids,

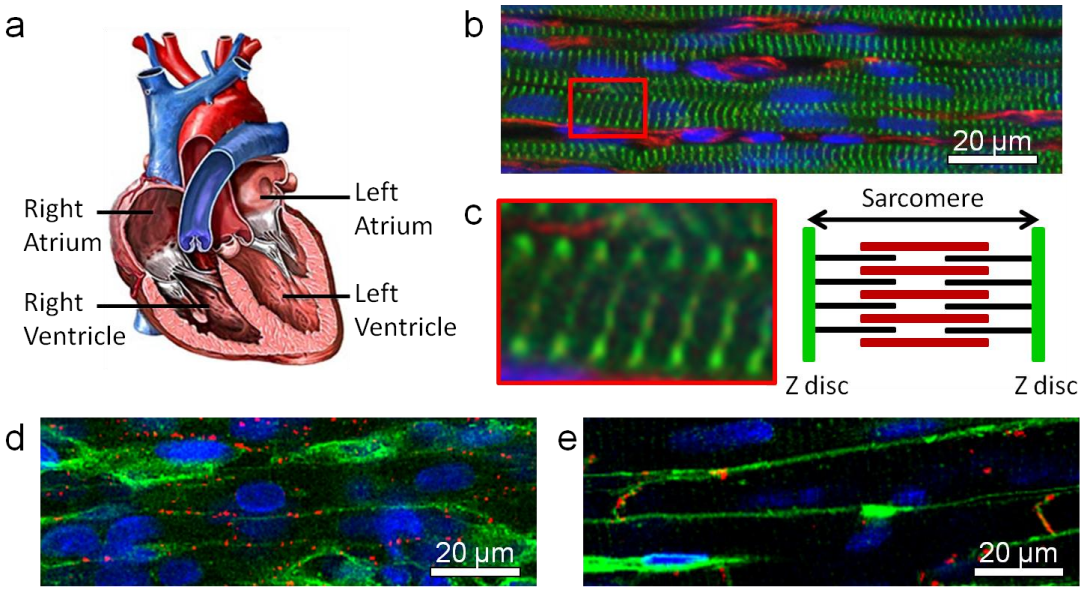

Figure 1.1 – Cardiac structure. (a) Cross-section showing four chambers of the heart. (b) Staining of postnatal day 12 left ventricular cardiac tissue of rat with α-sarcomeric actinin (green) to identify Z-discs of myocytes and vimentin (red) to identify non-myocytes (e.g. fibroblasts). (c) Zoomed region from B showing sarcomeres which are defined from Z-disc to Z-disc. (d, e) postnatal day 12 (d) and adult (e) left ventricular cardiac tissue of rat stained with wheat germ agglutinin (green) to identify cell borders and Cx43 (red) to identify gap junctions. Myocytes appear dark with Cx43 plaques located on the lateral sarcolemma in postnatal day 12 and concentrated at cell ends in adult tissue.

extracellular matrix (ECM) and cells, including myocytes, fibroblasts, endothelial, and vascular smooth muscle cells. Although myocytes only account for 20-40% of the cell population they occupy approximately 80-90% of the tissue volume [7, 8]. Fibroblasts account for the majority of cells in the heart and are in close spatial proximity to myocytes as shown in Fig. 1.1b.

Myocytes comprise sarcomeres, which are the fundamental unit of contraction and defined as multimolecular complexes between neighboring Z-discs (Fig. 1.1c). Z-discs are anchoring sites for actin and have a regular arrangement and spacing in healthy myocardium. Contraction of sarcomeres can be explained by the sliding filament theory based on myosin binding to actin in the presence of calcium and subsequent conformational changes of the myosin. Calcium concentration changes in the cytoplasm of myocytes can be described through a process known as calcium-induced calcium release (CICR) during excitation-contraction (EC) coupling. EC coupling is the process of converting an electrical stimulus (i.e., action potential) into a mechanical response. When a myocyte is depolarized, calcium ions enter the cytoplasm from the extracellular space through sarcolemmal ion channels. Cytoplasmic calcium binds to ryanodine receptors on the sarcoplasmic reticulum, which causes a further increase in the cytoplasmic calcium concentration. This process is known as CICR.

The left ventricular myocardium remodels during development and in response to environmental stress and disease [9, 10]. The remodeling is complex and can involve alterations in cell geometry, protein expression and distribution, and the extracellular matrix [9]. Remodeling can be a normal physiologic process due to development, exercise, and pregnancy or pathologic in response to hypertension, myocardial injury, and

ventricular unloading. Myocytes have been shown to increase in length, width, area and volume by 9%, 28%, 39% and 78%, respectively during hypertrophic remodeling [11], and decrease in volume by 50-75% with little change in length during atrophy [12]. Furthermore, early stages of ischemia are known to decrease the extracellular resistance and increase conduction velocity, which is indicative of reduced interstitial space [13].

Myocytes form a 3D syncytium by coupling via gap junction channels, which allows rapid propagation of electrical signals between cells and synchronous contraction. Cx43, the predominant gap junction channel isoform in ventricular myocytes [14, 15], has a half-life of approximately 2 hours [16, 17] and undergoes significant changes in density and distribution during development and disease [14, 18-23]. For example, in left ventricular neonatal rat cardiac tissue Cx43 clusters are lateralized as they are found to be distributed over the lateral sarcolemma of myocytes as shown in Fig. 1.1d. As the heart matures, Cx43 becomes polarized and organized at the cell ends after approximately 90 days postbirth as showed in Fig. 1.1e [18]. Gap junction channels also remodel due to disease in the adult heart. For example, as human cardiac hypertrophy progresses into heart failure Cx43 expression decreases and the distribution of Cx43 changes from being polarized to lateralized [9, 14, 19]. Gap junction channels can be coerced to rearrange *in vitro*. A recent study in 2D monolayers of neonatal rat myocytes indicated polarization of Cx43 localization by mechanical stretching [24]. The functional importance and dynamic nature of Cx43 makes it a target for analysis in both native and engineered cardiac tissue. However, most analyses are based on quantifying expression levels through Western blots or producing qualitative descriptions from 2D images in both native [15, 18, 19, 21, 25-27] and engineered tissues [28-32]. The complex spatial arrangement and

rearrangement may be better described and understood by quantitative 3D analysis techniques.

Fibroblasts account for the majority of nonmyocyte cells in the heart. Recent studies revealed the importance of fibroblasts in normal cardiac function [33, 34]. In addition to maintaining the ECM, fibroblasts are involved in paracrine signaling [34] and cell-cell communication between myocytes and other fibroblasts [35]. They are a main contributor to tissue remodeling in many forms of myocardial disease [34]. Following injury, such as infarction, fibroblasts secrete extracellular matrix to replace diseased myocardium with stiff, fibrotic tissue that leads to deleterious effects on cardiac function [36]. This deposition of collagen not only occurs in the infarcted region, but in the surrounding regions as well. The importance of fibroblasts is also becoming apparent in cardiac tissue engineering. In a study using co-cultures of myocytes and fibroblasts, myocyte elongation, alignment, and viability was shown to depend on the presence of fibroblasts [37].

The numerous structural and functional changes that occur during development and disease demonstrate a need to understand the complex structure-function relationships in cardiac tissue. This understanding may provide insights into onset, progression, prevention and therapy of heart disease.

1.3 Heart Disease

Although the heart is considered an engineering marvel by nature with complex structure and function, it is prone to fail beyond repair [5]. Heart disease is a general term used to categorize a variety of pathologies that adversely affect the heart. Coronary heart

disease is the most common form and accounts for more than two-thirds of heart related deaths in the United States [1]. Oftentimes, coronary heart disease can lead to myocardial infarction, which occurs due to lack of blood supply to the heart most commonly caused by blockage of the coronary artery. The lack of blood supply during myocardial infarction initiates a wound healing response that involves inflammation, myocyte death and formation of a collagen scar [38, 39]. Loss of myocardium not only occurs in the infracted region but the surrounding regions of the left ventricle as well. This loss causes an increase in mechanical stress on the left ventricle, triggering a biochemical cascade of intracellular signaling, which modulates a structural and functional remodeling process [39]. Myocytes are replaced by fibroblasts which deposit collagen to form a scar. The mechanical properties of the scar tissue counterbalance the distending forces on the left ventricular wall. This loss of contractile tissue deteriorates pump function, reduces stroke volume and can lead to congestive heart failure.

Congestive heart failure, defined as the inability of the heart to supply sufficient blood flow to the body, is not only caused by myocardial infarction, but can also be caused by hypertension, valvular diseases and other cardiomyopathies such as dilated and hypertrophic cardiomyopathy [40]. The many forms of heart disease are not mutually exclusive, and often patients have one or more forms of cardiovascular disease [1]. Another form of heart disease is congenital heart defects which occur in 9 of every 1000 births and are the leading cause of death in the first year of life [1]. Congenital heart defects are commonly ventricular septal defects, atrial septal defects, valvular pulmonary stenosis, or other malformations [1, 41]. These defects often require reconstructive

surgery and in cases of severe malformation, surgical reconstruction is not sufficient to sustain life [41].

Treatment and management of heart disease is challenging due to the limited capacity of the heart to repair following injury. Although current strategies such as pharmaceutical drugs, medical devices and lifestyle changes have improved and extended the life for millions of individuals, they are commonly targeted to managing heart disease as opposed to treatment [3]. Although organ transplants are successful in treating end-stage heart failure, they are in short supply [1]. Future strategies to manage and treat heart disease will likely be based upon biological approaches using cell therapy and tissue engineering strategies, both of which have the potential to regenerate the myocardium and improve cardiac function.

1.4 Biological Approaches to Treat Heart Disease

Biological strategies for treatment of heart disease can be categorized into cell therapy and tissue engineering approaches. Cardiac cell therapy, also known as *in situ* cardiomyoplasty, is based on introducing progenitor or stem cells into the myocardium to treat infarction and congestive heart failure and has been in the clinical arena since early 2000 [42, 43]. Tissue engineering approaches to treat heart disease are much further from clinical evaluation and are based on either *in vitro* cultivation of cells with or without biomaterials and subsequent implantation or *in situ* approaches which combine cells with injectable biomaterials [44]. However, tissue engineering not only aims to provide organ replacement. Cardiac tissue produced *in vitro* can serve as a surrogate for testing pharmaceutics and understanding cardiovascular physiology, pathophysiology and

developmental processes [45-47]. In fact, the original definition of tissue engineering established at a conference by the National Science Foundation in Lake Tahoe, 1988 reflects this concept [48]: "tissue engineering is the application of principles and methods of engineering and life sciences toward fundamental understanding of structure-function relationships in normal and pathological mammalian tissues and the development of biological substitutes to restore, maintain, or improve tissue function." The following sections discuss the current status of cell therapy and tissue engineering.

1.4.1 Cell Therapy

Cardiac cell therapy is based on introducing progenitor or stem cells into the myocardium to treat acute and chronic heart failure [42, 43]. The benefits of cell therapy are controversial and the majority of studies only show a modest improvement in patient outcomes [43, 49]. When clinical trials first began in early 2000, the central dogma was that the delivered cells would exhibit or acquire *in situ* phenotypic features of myocytes and thus replace the irreversibly lost myocytes [42]. However, most of the favorable outcomes have been attributed to paracrine effects of the donor cells and angiogenesis as opposed to myogenesis [42]. Cytokines and growth factors released by the donor cells induce protective signaling pathways in the host myocardium to promote angiogenesis, reduce apoptosis, encourage favorable matrix remodeling and in some cases coerce resident native cells to differentiate into myocytes [50, 51]. The hypothesis that paracrine signaling is responsible for the improvement in cardiac function is supported by a recent study which demonstrated that injection of mesenchymal stem cell conditioned media had equivalent effects to injected cells [52].

Several types of progenitor and stem cells have been applied in human clinical trials including: skeletal myoblast, circulating progenitor cells, CD133-positive cells, CD34-positive cells, endothelial progenitor cells and bone marrow derived cells such as mononuclear cells, hematopoietic stem cells and mesenchymal stem cells [49, 53]. Early clinical trials started with skeletal myoblasts because of their favorable results in animal studies [43]. Although skeletal myoblasts do not differentiate directly into cardiac myocytes, they differentiate into myotubes which are resistant to ischemic environments [54, 55]. Furthermore, they offer a favorable immune response due to their autologous origin and have a restricted lineage which provides a safety factor against tumorogenesis. However, incidence of cardiac arrhythmias in patients with skeletal myoblasts injections has raised concern [56]. Since skeletal myoblasts and myotubes do not express Cx43, they do not integrate electrically with the host myocardium and consequently beat asynchronously [57].

Embryonic stem cells are the classical stem cells and hold the potential to self renew and differentiate into any cell type. However, they have not been applied clinically due to their potential to form teratomas and induce an immune response due to their allogenic origin [58, 59]. More recently, induced pluripotent stem cells have been developed from human origin and resemble many features of embryonic stem cells [60, 61]. Although induced pluripotent stem cells have successfully been differentiated into cardiac myocytes [62], their potential application to human cardiac cell therapy is still in its infancy as reprogramming efficiency is low and costly [63].

A major shortcoming with cell therapy is poor cell retention and engraftment [64]. Less than 10% of the donor cells are retained in the myocardium within 24 hours of

delivery [63, 65, 66]. Ultimately, donor cells are injected into an unfavorable, hostile environment that does not support cell survival. Methods to successfully increase retention and engraftment have been implemented such as preconditioning cells with pharmaceutical agents, introducing prosurvival cocktails and delivering cells within hydrogels which polymerize *in situ* [64, 67]. However, cell retention and engraftment are still unfavorable. In addition, a general consensus in the field of cell therapy is the lack of a mechanistic understanding on how donor cells improve cardiac function and patient outcomes [53, 54, 68].

1.4.2 Cardiac Tissue Engineering

Traditionally, cardiac tissue engineering is perceived as an approach for replacement or repair of diseased or injured myocardium. However, there are a variety of alternative applications for *in vitro* cardiac tissue engineering, including applications in pharmaceutics that require high throughput techniques for drug screening and safety testing [45, 46], physiological genomics [69], and cardiovascular physiology to understand disease and developmental processes [47]. Studying cardiac tissue *in vitro* requires tissue culture platforms that allow for control over environmental conditions to direct cells into healthy and diseased tissue and analytical tools for understanding structure and function.

A central goal in cardiac tissue engineering is to establish the 3D architecture of native tissue. Although 2D culture has been utilized to successfully probe at many scientific questions, 3D tissue samples provide a more realistic environment. Three-dimensional tissue constructs more closely mimic the cellular microenvironment, which

has profound effects on the properties, behavior and functions of resident cells [6, 70, 71]. Capturing this microenvironment through 3D tissue samples may provide a more realistic test sample that can better predict *in vivo* results. However, replicating the 3D structure and function of cardiac tissue *in vitro* is challenging due to the inherent complexity of cardiac tissue. Compounding this complexity is the dynamic nature of cardiac tissue. As pointed out above, remodeling of structural properties, such as myocyte geometry and protein distributions, occurs during development and disease. Therefore, choosing an appropriate native target for tissue engineering is not trivial and requires careful selection based on requirements.

Several approaches have been applied to establish 3D tissue samples, each with some level of success. The current state-of-the-art for developing cardiac tissue *in vitro* can be categorized into four techniques: 1) seeding scaffold materials with cells, 2) entrapping cells in a 3D environment, 3) creating cell sheets, and 4) decellularizing and recellularizing tissue [41]. Scaffolding materials can serve as a substrate to direct cell proliferation and differentiation and are usually porous and fibrous to allow for cell seeding and diffusion. Degradable synthetic scaffolds, such as polyglyocolic acid [72, 73] and polyglycerol sebacate [32], and natural scaffolds, such as collagen foam sponges [28], alginate [74] and gelatin [75], have been used to engineer cardiac tissue. Synthetic materials have the advantage of engineering control, but are limited in their biocompatibility *in vivo*. Natural materials can provide signaling to cells through surface receptors, but are often limited in their ability to be engineered for a specific purpose.

The formation of 3D spontaneously contracting cardiac constructs has been created by entrapping cardiac cells in a hydrogel comprised of Matrigel (extracellular

matrix from Engelbreth-Holm-Swarm tumors), collagen [76], and more recently fibrinogen [77]. This encapsulation approach is arguably the most successful for creating densely packed and highly aligned myocytes as found in native tissue. The addition of mechanical stimulation can improve structural organization and increase force of contraction [78-80]. Cells entrapped in collagen/Matrigel mixtures have been shown to electrically and mechanically couple with the host myocardium in rats [81, 82] and improve cardiac function following infarction [83]. More recently, fibrin-based samples have been fabricated using either neonatal cardiac cells [77] or human embryonic stem cells [84]. These fibrin-based samples are cultured in a multiwell plate format and proposed to serve as models to study pharmaceutical agents and probe at physiological processes.

Cell sheet cardiac tissue engineering is a scaffold-free approach to tissue engineering and utilizes a temperature-sensitive poly(N-isopropylacrylamide) (PIPAAm) coated surface seeded with cells [85]. During culture at 37°C PIPAAm is hydrophobic, as the temperature is lowered below its lower critical solution temperature (LCST) of 32°C the polymer becomes hydrophilic to release a monolayer of cells. The cell sheets spontaneously contract and can be stacked to form 3D engineered constructs which are electrically coupled [85]. This approach allows for cells to detach without disrupting gap junctions and other surface proteins that are destroyed during enzymatic digestion. To overcome limitations of the construct thickness “polysurgery” has been performed on rats, which involves repeated implantation of sheets comprised of three cell layers [86]. Although this approach requires repeated access to the surgical site, up to 10 sheets (each three layers thick) have been implanted and shown to become vascularized and

electrically couple with the host myocardium [86]. Moreover, the cell sheet approach in an infracted rat model resulted in a much higher survival rate and improvement in cardiac function over direct cell injection techniques [87].

The recellularization approach relies on decellularizing harvested organs and tissues to remove immunogenic substances and repopulating with cells to form tissue [88]. The composition, architecture and mechanical properties of the decellularized ECM are preserved by this process. This approach has been applied to adult rat hearts, which were reseeded with intramural injections of neonatal cardiac cells and after 8 days of cultivation were able to generate pressures at approximately 2% of the adult heart [89]. Although this is an appealing approach, complete reseeding and functionality of a native heart has not been demonstrated.

Many of the developed *in vitro* approaches rely on bioreactors to control environmental conditions and characterize the engineered tissue. A bioreactor can be defined as an apparatus that attempts to mimic and reproduce physiological conditions in order to grow and maintain biological cells or tissues [90]. Bioreactors are an attractive option to provide 3D tissue culture environments to allow for cell-cell and cell-matrix interactions. Current bioreactors for cardiac tissue engineering can be categorized based on their design [91, 92].

Spinner-flask bioreactors overcome mass transfer limitations of static culture environments and have shown to improve cell seeding and development of cardiac tissue constructs [73, 93]. Similarly, rotating wall vessels are capable of producing low levels of shear stress while improving mass transfer rates, and have demonstrated the ability to create elongated myocytes, establish intracellular communication, and form

spontaneously contracting cardiac tissue constructs [29, 72, 94, 95]. Direct perfusion systems have overcome limitations of poor cell infiltration and nonuniform cell coverage in 3D tissue constructs and have been shown to enhance cell survival, growth, and function [93, 96-98]. Environmental features of bioreactors for cardiac tissue engineering include mechanical conditioning such as cyclic strain [78-80, 99] and electrical stimulation [28, 99-102]. Mechanical conditioning was found to enhance cell proliferation and matrix organization of human heart cells [103], and structural organization and force of contraction in neonatal rat cardiac constructs [78-80, 104-106]. Electrical stimulation was shown to induce myocyte alignment, increase electrical coupling via Cx43 up-regulation, and increase conduction velocity [28, 107]. However, only little is known about the specific mechanical force and pacing regime that is responsible for promoting development to a specific tissue phenotype [91, 108].

Although several approaches have been used to engineer cardiac tissue with some level of success, many shortcomings remain [5]. Some of these shortcomings are related to the need for advanced tissue culture platforms that can control environmental conditions such as mechanical, electrical and chemical factors and integrate analysis techniques to continuously characterize the response of cells to environmental stimuli. Moreover, current bioreactors are often unique designs used in a series of targeted studies. Although they meet their intended function there is no emerging standard [5]. Many of these designs are limited in function, complex, unreliable and difficult to set up and operate [91, 109]. They have not been designed for low cost, ease of use, and reliability. Furthermore, current bioreactors for cardiac tissue engineering are not outfitted for analysis of engineered tissue during culture. Characterizing tissue samples

during development can provide feedback without destroying tissue samples. A bioreactor that is designed with common cell culture equipment, off the shelf components, and reproducible parts to address these limitations and includes cyclic stretching and tools for nondestructive analyses, such as force measurement and confocal imaging capabilities, would be desirable.

In addition, a central goal in cardiac tissue engineering is to establish hallmarks of the native myocardium. Applying an engineering approach to meet this goal requires a set of requirements and specifications. The engineering paradigm relies on specifications, which are derived directly from a set of requirements. When applying the engineering paradigm to the field of tissue engineering, specifications for the target tissue would logically be derived from native tissue. However, few studies apply the same analysis techniques used to characterize their engineered tissue to native cardiac tissue for comparison purposes. Ideally, native tissue samples would be characterized to establish quantitative specifications for engineered cardiac tissue.

Evaluation of engineered cardiac tissue structure and function is commonly constrained to endpoint analyses [110, 111]. Most analyses of structure are based on 2D images from light microscopy, confocal microscopy, scanning electron microscopy and transmission electron microscopy [112]. The 2D images provide information on the expression and distribution of troponin I and myosin heavy chain for presence and maintenance of the cardiac phenotype [28, 37]; α-actin for cell alignment [28, 37, 113]; Cx43 [28, 114] and β-integrin [28] for determining cell-cell and cell-matrix communication, respectively; cell nuclei for cell density [37, 114]; and live/dead assays for cell viability [114]. Real-time polymermerase chain reaction (RT-PCR) and Western

blot techniques have been used to quantify the gene and protein expression, respectively, of α-actin, α-myosin heavy chain (MHC), β-MHC, Cx43, and β-integrin [28]. However, an outstanding goal in cardiac tissue engineering is to establish structural hallmarks of the native myocardium. The native myocardium exhibits a complex 3D architecture where analysis techniques which allow for 3D characterization would be beneficial.

1.5 Confocal Microscopy and Image Processing

Confocal imaging is one technique that has the capability of producing high resolution 3D images. Recent advances in imaging technologies combined with new developments in fluorescent markers [115, 116] have established microscopic imaging as a major research tool to measure structure and function of cells and tissues [117-122]. Unlike traditional microscopic imaging modalities, such as bright field microscopy, confocal laser scanning microscopy (CLSM) has the ability to distinguish in-focus from out-of-focus light [123]. The concept of confocal microscopy was pioneered by Marvin Minsky in 1955 when he was trying to overcome limitations of bright field microscopy [124]. Minsky found that by illuminating and collecting light from a single point avoided the scattered light found to obscure bright field images. Fig. 1.2a demonstrates the principle of confocal microscopy. A point source of light is focused on a specimen through an objective (blue lines in Fig. 1.2a). Emitted light is collected from only the point source by passing through a pinhole (blue lines in Fig. 1.2a). Light that is not emitted from the focal point is excluded (red dashed lines in Fig. 1.2a).

This ability to reject out-of-focus light allows CLSM to control the depth of field (slice resolution of <1 μm) and acquire sequential optical sections from thick specimens

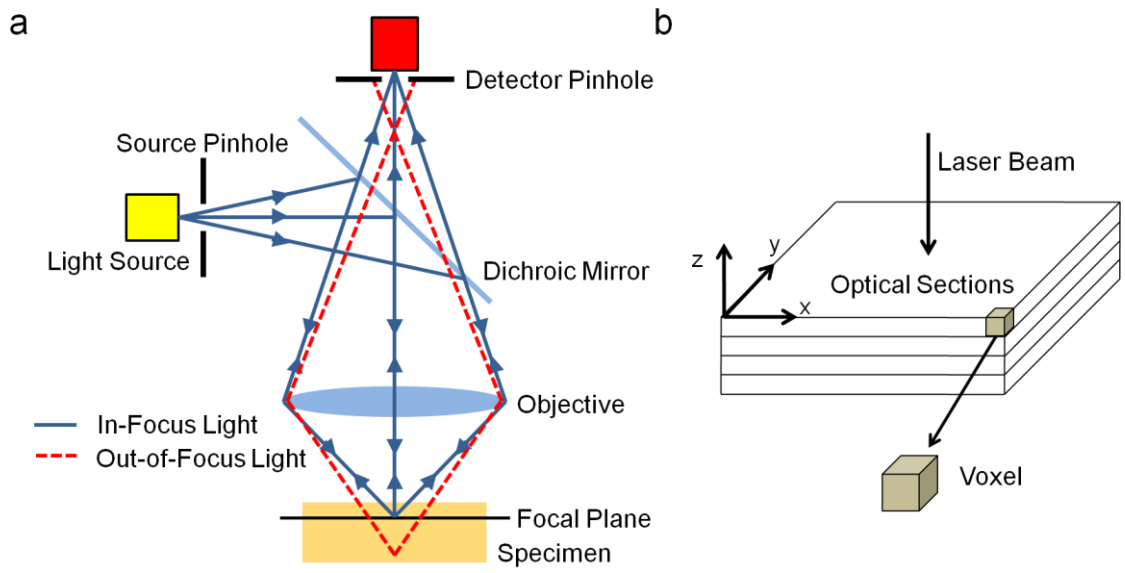

Figure 1.2 – Confocal microscopy. (a) Schematic demonstrating principle of confocal microscopy. (b) Serial 2D optical sections can be acquired to obtain 3D image data.

[125]. Images are acquired point-by-point (i.e., pixel-by-pixel) by rastering a laser over an image plane. Sequential optical sections can be stacked to create a 3D image volume where pixels become volumetric elements known as voxels (Fig. 1.2b). These advantages have established CLSM as a major research technique used to gain insights into cellular and molecular physiology and pathophysiology.

In addition to producing high resolution images of fixed tissue samples, CLSM is particularly well suited for providing real-time, noninvasive data on sub-cellular and cellular processes of living tissue [110]. Living tissue can be probed with structural or functional markers and imaged on conventional upright or inverted confocal microscopes or the recently developed fiber-optics based confocal imaging systems [126-131]. Fiber-optics based confocal imaging systems consist of an objective placed at the end of a 3 meter long, thin optical fiber. This portable technology allows for *in situ* and *in vivo* imaging in human patients and laboratory animal testing. However, since confocal imaging relies on fluorescence and most tissues do not exhibit significant autofluorescence, a fluorescent marker must be present in the imaged region. There are currently few, if any, techniques to apply dye directly to the imaged area of living tissue in a controlled and efficient manner.

Images from confocal microscopy suffer from various imaging artifacts. These artifacts are caused by several factors such as heterogeneous refractive indices within the specimen, mismatches in the refractive index of the specimen, objective, glass slide and the material between those, and chromatic and spherical aberrations introduced by the optical elements in the microscope [125]. The resulting scattering, absorption and refraction of light degrade image quality, for instance, signal-to-noise ratio and image

resolution. An approach to characterize imaging artifacts is to measure the response of the confocal imaging system to a point source of light, yielding the so-called point spread function (PSF). The PSF describes how the confocal imaging system responds to a point source of light. PSFs are measured by imaging objects of a known size, commonly fluorescent beads [125, 132, 133]. Fig. 1.3 shows an example of a measured PSF from a confocal imaging system (Zeiss LSM 5, Jena, Germany) using a 40x oil immersion lens with a numerical aperture of 1.3 and 543 nm laser line for excitation. Fluorescent beads with a 100 nm diameter were imaged at a 100 nm isometric resolution. Although the beads are similar in size as a single voxel, the resultant images portray the beads to be larger than a single voxel (Figs. 1.3a and c), in particular, parallel to the laser beam direction. The effective resolution of the confocal microscope can be estimated from the PSF. The full width at half maximum (FWHM) intensity of the PSF describes the minimum size in which an object can be spatially resolved [134]. As shown in Figs. 1.3b and d the FWHM are two to three times larger in the direction of the laser beam compared to the FWHM in the image plane.

Image quality can be improved based on the measured PSFs. The response *g* of an imaging system to given sources can be described by convolution of the source image *f* with the PSF *h*:

$$g(x) = (f * h)(x) = \int\int\int_{-\infty}^{\infty} f(x')h(x - x')dx'$$

Deconvolution algorithms, such as the iterative Richardson-Lucy algorithm [135], can be applied to reconstruct the source image *f* from the image *g*:

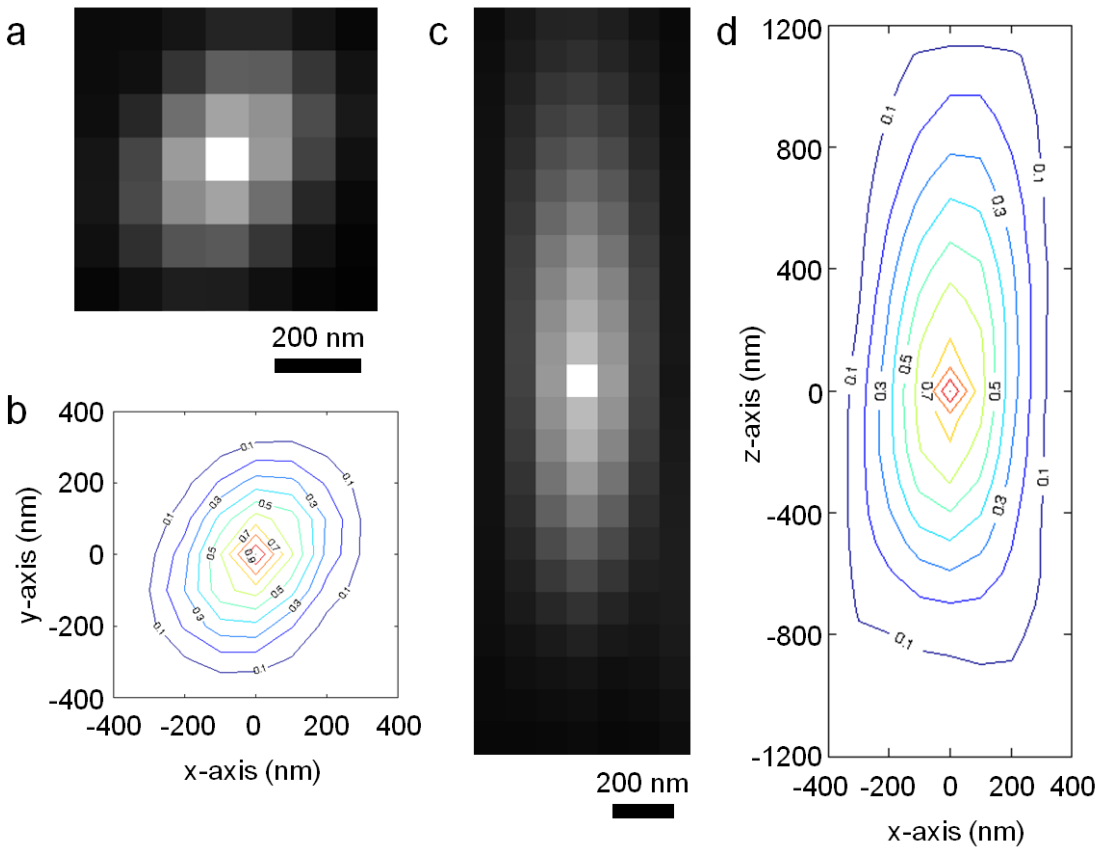

Figure 1.3 – Example of a measured PSF. (a, c) Central cross-section through 3D image stack from 100 nm fluorescent beads imaged at 100 nm resolution in the plane perpendicular to laser beam direction (a) and parallel to laser beam direction (c). (b, d) Intensity maps with isolines representing fall off of signal intensity.

$$g_{n+1} = g_n\left(\frac{g_0}{g_n * h} \otimes h\right)$$

with the cross-correlation operator $\otimes$ and $g_0 \equiv g$.

Three-dimensional confocal microscopy is based on acquiring sequential serial 2D images of the specimen. Acquiring sequential optical sections from thick specimens results in lower signal intensity at increased depths. Several factors are responsible for depth-dependent attenuation such as absorption and scattering of excitation and emission light, photobleaching, and uneven fluorescent labeling. Regardless of the cause, decay in signal intensity can be estimated empirically by fitting an exponential function of the form:

$$I_z = I_0 e^{-az}$$

where I_z is the intensity, I_0 is intensity at slice 0, a is the attenuation coefficient estimating intensity loss, and z is the image depth [136-139]. Applying a slice-wise correction factor to 3D image data is essential when applying thresholding to segment objects within the image stacks. Commonly, segmentation is based on thresholding and in order to have a constant threshold value through the 3D image volume, images acquired at deeper depths must be corrected [132, 138, 140, 141].

Three-dimensional reconstructions of cardiac structure can be obtained from 3D confocal image data using segmentation and thresholding approaches [117, 118, 121, 142]. For example, the structure of transverse tubules which are invaginations in the sarcolemma of myocytes, [121] and the collagenous microstructure of ventricular

trabeculae carneae [142] have been described using 3D reconstructions from confocal image data. These 3D reconstructions can serve as a basis for performing quantitative measures to describe cellular and subcellular features. Establishing a cohesive framework that includes methods for labeling tissue, image processing and extracting quantitative features from both living and fixed cardiac tissue specimens will help direct our understanding in order to engineer and specify cultured tissue.

1.6 Introduction to this Dissertation

In this work, an engineering approach was applied to develop and utilize tools and methods to produce engineered cardiac tissue, characterize both native and engineered cardiac tissue and test the hypothesis that the structure of age-matched native cardiac tissue serves as a representative control for engineered cardiac tissue. Establishing hallmarks of the native myocardium in engineered cardiac tissue is a central goal and appears to be required for creating functional tissue that can serve as a surrogate for *in vitro* testing or the eventual replacement of diseased or injured myocardium [6]. We worked towards this longstanding goal by developing and applying confocal imaging techniques and analyses to characterize the 3D architecture of native and engineered cardiac tissue. In addition, we engineered and developed specialized cultureware to meet the needs of our studies. This type of customized cultureware is essential for controlling environmental conditions, integrating analysis techniques to characterize tissue during development and directing cells into functional tissue [5]. Three phases of research were conducted to address unmet needs in the field of cardiac tissue engineering.

In Chapter 2, a confocal microscopy based framework was developed and utilized to characterize the microstructure in living cardiac tissue. Previous studies have applied confocal microscopy *ex vivo* to characterize normal and pathological alterations in cardiac microstructure for analysis and modeling purposes [21, 118-120, 143]. However, most of these studies were performed using fixed tissue and time consuming immunochemistry procedures which require excision, fixation, sectioning and cell membrane perforation [112]. Our developed framework includes a method for local dye delivery to living cardiac tissue, confocal microscopy techniques and image processing tools for the 3D analysis of myocyte geometry and the extracellular space. In living tissue preparations we demonstrated that our hydrogel-based dye delivery method provided dye in sufficient concentration to obtain images with both standard and fiber-optics based confocal imaging systems. Image processing and myocyte segmentation was applied to extract individual myocytes from 3D image data. The developed framework for image processing and analysis served as a foundation for the research performed in Chapter 4. An important perspective of the developed imaging approach and analysis is the future application to diagnosis and patient-specific modeling of cardiac tissue structure.

In Chapter 3, a bioreactor capable of continuously monitoring force-displacement in engineered tissue was developed. Although other laboratory bioreactors meet their intended function, they are typically developed to meet the needs of a single laboratory and targeted towards a specific series of experiments. Bioreactors that are reproducible, modifiable and easy to use have the potential to be adopted by multiple laboratories and become a type of open-source design platform for tissue engineering. Toward this end, our bioreactor was designed with common cell culture equipment and off the shelf and

easily reproducible components. A full bill of materials and associated engineering drawings are available for our bioreactor. A novelty of the developed bioreactor is in the ability to nondestructively characterize tissue samples during development. Forces from inside the bioreactor are translated to an external transducer through a magnet-diaphragm assembly, which allows for characterization of mechanical properties of the tissue samples during culture. Bench top testing and tissue culture experiments were performed to validate bioreactor performance. The ability to characterize passive and active forces in engineered tissue is important for high throughput monitoring techniques in pharmaceutical testing [45, 46] and cardiac tissue engineering [78, 99]. Our ability to quickly design and implement custom bioreactors was key to the work described in Chapters 3 and 4. This capability comes at a low cost and high value due to using standard off the shelf cultureware as starting material.

In Chapter 4, approaches for confocal imaging and image analysis were developed and applied to quantitatively describe features of the native myocardium, focusing on myocyte geometry and spatial distribution of a major gap junction protein Cx43, in both engineered tissue and native tissue. A central goal in cardiac tissue engineering is to establish structural features of the native myocardium. As described in Chapter 1, native tissue is complex and structurally remodels during development and disease. Therefore, choosing an appropriate native target for tissue engineering is not trivial and requires careful selection based on requirements. Moreover, many studies describe structural features qualitatively from 2D images. In our study, we quantitatively compared engineered cardiac tissue with and without electrical stimulation to both age-matched and adult native myocardium using 3D confocal imaging. We addressed the

hypothesis that the application of environmental cues directs engineered tissue towards a phenotype resembling that of age-matched native myocardium. The results of the study support this hypothesis and reveal that electrical stimulation produces tissue with myocyte geometries and the spatial distributions of Cx43 which more closely resemble age-matched native myocardium as opposed to mature adult tissue.

1.7 References

[1] D. Lloyd-Jones, R. Adams, M. Carnethon, G. De Simone, T. B. Ferguson, K. Flegal, E. Ford, K. Furie, A. Go, and K. Greenlund, "Heart Disease and Stroke Statistics--2009 Update. A Report From the American Heart Association Statistics Committee and Stroke Statistics Subcommittee," *Circulation,* vol. 119, pp. e21-e181, 2009.

[2] M. J. Budoff, *Cardiac CT Imaging: Diagnosis of Cardiovascular Disease*. London: Springer Verlag, 2010.

[3] R. O. Bonow, D. L. Mann, D. P. Zipes, and P. Libby, *Braunwald's Heart Disease: A Textbook of Cardiovascular Medicine*, 9th ed. Philadelphia Elselvier Saunders, 2012.

[4] H. Krum and J. R. Teerlink, "Medical therapy for chronic heart failure," *Lancet,* vol. 378, pp. 713-721, 2011.

[5] G. Vunjak-Novakovic, N. Tandon, A. Godier, R. Maidhof, A. Marsano, T. P. Martens, and M. Radisic, "Challenges in cardiac tissue engineering," *Tissue Eng Part B Rev,* vol. 16, pp. 169-187, 2010.

[6] N. T. Elliott and F. Yuan, "A review of three-dimensional in vitro tissue models for drug discovery and transport studies," *J Pharm Sci,* vol. 100, pp. 59-74, 2011.

[7] A. C. Nag, "Study of non-muscle cells of the adult mammalian heart: a fine structural analysis and distribution," *Cytobios,* vol. 28, pp. 41-61, 1980.

[8] P. Camelliti, T. K. Borg, and P. Kohl, "Structural and functional characterisation of cardiac fibroblasts," *Cardiovasc Res,* vol. 65, pp. 40-51, 2005.

[9] J. A. Hill and E. N. Olson, "Cardiac plasticity," *N Engl J Med,* vol. 358, pp. 1370-1380, 2008.

[10] P. Ahuja, P. Sdek, and W. R. MacLellan, "Cardiac myocyte cell cycle control in development, disease, and regeneration," *Physiol Rev,* vol. 87, pp. 521-544, 2007.

[11] H. W. Vliegen, A. Laarse, J. A. N. Huysman, E. C. Wijnvoord, M. Mentar, C. J. Cornelisse, and F. Eulderink, "Morphometric quantification of myocyte dimensions validated in normal growing rat hearts and applied to hypertrophic human hearts," *Cardiovasc Res,* vol. 21, pp. 352-357, 1987.

[12] S. E. Campbell, B. Korecky, and K. Rakusan, "Remodeling of myocyte dimensions in hypertrophic and atrophic rat hearts," *Circ Res,* vol. 68, pp. 984-996, 1991.

[13] W. E. Cascio, G. X. Yan, and A. G. Kleber, "Passive electrical properties, mechanical activity, and extracellular potassium in arterially perfused and ischemic rabbit ventricular muscle. Effects of calcium entry blockade or hypocalcemia," *Circ Res,* vol. 66, pp. 1461-1473, 1990.

[14] B. E. J. Teunissen, H. J. Jongsma, and M. F. A. Bierhuizen, "Regulation of myocardial connexins during hypertrophic remodelling," *Eur Heart J,* vol. 25, pp. 1979-1989, 2004.

[15] N. J. Severs, E. Dupont, S. R. Coppen, D. Halliday, E. Inett, D. Baylis, and S. Rothery, "Remodelling of gap junctions and connexin expression in heart disease," *Biochim Biophys Acta,* vol. 1662, pp. 138-148, 2004.

[16] H. A. Fozzard, "Gap junctions and liminal length in hypertrophy: something old and something new," *J Cardiovasc Electrophysiol,* vol. 12, pp. 836-837, 2001.

[17] M. A. Beardslee, J. G. Laing, E. C. Beyer, and J. E. Saffitz, "Rapid turnover of connexin43 in the adult rat heart," *Circ Res,* vol. 83, pp. 629-635, 1998.

[18] B. D. Angst, L. U. R. Khan, N. J. Severs, K. Whitely, S. Rothery, R. P. Thompson, A. I. Magee, and R. G. Gourdie, "Dissociated spatial patterning of gap junctions and cell adhesion junctions during postnatal differentiation of ventricular myocardium," *Circ Res,* vol. 80, pp. 88-94, 1997.

[19] S. Kostin, S. Dammer, S. Hein, W. P. Klovekorn, E. P. Bauer, and J. Schaper, "Connexin 43 expression and distribution in compensated and decompensated cardiac hypertrophy in patients with aortic stenosis," *Cardiovasc Res,* vol. 62, pp. 426-436, 2004.

[20] R. Sepp, N. J. Severs, and R. G. Gourdie, "Altered patterns of cardiac intercellular junction distribution in hypertrophic cardiomyopathy," *Heart,* vol. 76, pp. 412-417, 1996.

[21] N. S. Peters, "New insights into myocardial arrhythmogenesis: distribution of gap-junctional coupling in normal, ischaemic and hypertrophied human hearts," *Clin Sci (Lond),* vol. 90, pp. 447-452, 1996.

[22] E. Dupont, T. Matsushita, R. A. Kaba, C. Vozzi, S. R. Coppen, N. Khan, R. Kaprielian, M. H. Yacoub, and N. J. Severs, "Altered connexin expression in human congestive heart failure," *J Mol Cell Cardiol,* vol. 33, pp. 359-371, 2001.

[23] J. Jin, S. I. Jeong, Y. M. Shin, K. S. Lim, H. Shin, Y. M. Lee, H. C. Koh, and K. S. Kim, "Transplantation of mesenchymal stem cells within a poly (lactide-co-{varepsilon}-caprolactone) scaffold improves cardiac function in a rat myocardial infarction model," *Eur J Heart Fail,* vol. 11, pp. 147-153, 2009.

[24] A. Salameh, A. Wustmann, S. Karl, K. Blanke, D. Apel, D. Rojas-Gomez, H. Franke, F. W. Mohr, J. Janousek, and S. Dhein, "Cyclic mechanical stretch induces cardiomyocyte orientation and polarization of the gap junction protein connexin43," *Circ Res,* vol. 106, pp. 1592-1602, 2010.

[25] N. S. Peters, N. J. Severs, S. M. Rothery, C. Lincoln, M. H. Yacoub, and C. R. Green, "Spatiotemporal relation between gap junctions and fascia adherens junctions during postnatal development of human ventricular myocardium," *Circulation,* vol. 90, pp. 713-725, 1994.

[26] F. G. Akar, R. D. Nass, S. Hahn, E. Cingolani, M. Shah, G. G. Hesketh, D. DiSilvestre, R. S. Tunin, D. A. Kass, and G. F. Tomaselli, "Dynamic changes in conduction velocity and gap junction properties during development of pacing-induced heart failure," *Am J Physiol Heart Circ Physiol,* vol. 293, pp. H1223-1230, 2007.

[27] C. Sasano, H. Honjo, Y. Takagishi, M. Uzzaman, L. Emdad, A. Shimizu, Y. Murata, K. Kamiya, and I. Kodama, "Internalization and dephosphorylation of connexin43 in hypertrophied right ventricles of rats with pulmonary hypertension," *Circ J,* vol. 71, pp. 382-389, 2007.

[28] M. Radisic, H. Park, H. Shing, T. Consi, F. J. Schoen, R. Langer, L. E. Freed, and G. Vunjak-Novakovic, "Functional assembly of engineered myocardium by electrical stimulation of cardiac myocytes cultured on scaffolds," *Proc Natl Acad Sci U S A,* vol. 101, pp. 18129-18134, 2004.

[29] N. Bursac, M. Papadaki, J. A. White, S. R. Eisenberg, G. Vunjak-Novakovic, and L. E. Freed, "Cultivation in rotating bioreactors promotes maintenance of cardiac myocyte electrophysiology and molecular properties," *Tissue Eng,* vol. 9, pp. 1243-1253, 2003.

[30] L. L. Chiu, R. K. Iyer, J. P. King, and M. Radisic, "Biphasic electrical field stimulation aids in tissue engineering of multicell-type cardiac organoids," *Tissue Eng Part A,* vol. 17, pp. 1465-1477, 2008.

[31] Y. C. Huang, L. Khait, and R. K. Birla, "Contractile three-dimensional bioengineered heart muscle for myocardial regeneration," *J Biomed Mater Res A,* vol. 80, pp. 719-731, 2007.

[32] M. Radisic, H. Park, T. P. Martens, J. E. Salazar-Lazaro, W. Geng, Y. Wang, R. Langer, L. E. Freed, and G. Vunjak-Novakovic, "Pre-treatment of synthetic elastomeric scaffolds by cardiac fibroblasts improves engineered heart tissue," *J Biomed Mater Res A,* vol. 86, pp. 713-724, 2008.

[33] C. A. Souders, S. L. K. Bowers, and T. A. Baudino, "Cardiac fibroblast: the renaissance cell," *Circ Res,* vol. 105, pp. 1164-1176, 2009.

[34] R. Kakkar and R. T. Lee, "Intramyocardial fibroblast myocyte communication," *Circ Res,* vol. 106, pp. 47-57, 2010.

[35] S. Zlochiver, V. Muñoz, K. L. Vikstrom, S. M. Taffet, O. Berenfeld, and J. Jalife, "Electrotonic myofibroblast-to-myocyte coupling increases propensity to reentrant arrhythmias in two-dimensional cardiac monolayers," *Biophys J,* vol. 95, pp. 4469-4480, 2008.

[36] B. Swynghedauw, "Molecular mechanisms of myocardial remodeling," *Physiol Rev,* vol. 79, pp. 215-262, 1999.

[37] J. W. Nichol, G. C. Engelmay, M. Cheng, and L. E. Freed, "Co-culture induces alignment in engineered cardiac constructs via MMP-2 expression," *Biochem Biophys Res Commun,* vol. 373, pp. 360-365, 2008.

[38] M. A. Pfeffer and E. Braunwald, "Ventricular remodeling after myocardial infarction. Experimental observations and clinical implications," *Circulation,* vol. 81, pp. 1161-1172, 1990.

[39] M. G. Sutton and N. Sharpe, "Left ventricular remodeling after myocardial infarction: pathophysiology and therapy," *Circulation,* vol. 101, pp. 2981-2988, 2000.

[40] J. J. McMurray and M. A. Pfeffer, "Heart failure," *Lancet,* vol. 365, pp. 1877-1889, 2005.

[41] W. H. Zimmermann and R. Cesnjevar, "Cardiac tissue engineering: implications for pediatric heart surgery," *Pediatr Cardiol,* vol. 30, pp. 716-723, 2009.

[42] P. Menasché, "Stem cell therapy for chronic heart failure. Lessons from a 15-year experience," *C R Biol,* vol. 334, pp. 489-496, 2011.

[43] P. Menasché, "Cardiac cell therapy: Lessons from clinical trials," *J Mol Cell Cardiol,* vol. 50, pp. 258-265, 2011.

[44] G. Vunjak-Novakovic, K. O. Lui, N. Tandon, and K. R. Chien, "Bioengineering heart muscle: A paradigm for regenerative medicine," *Annu Rev Biomed Eng,* vol. 15, pp. 245-267, 2011.

[45] D. D. Allen, R. Caviedes, A. M. Cárdenas, T. Shimahara, J. Segura-Aguilar, and P. A. Caviedes, "Cell lines as in vitro models for drug screening and toxicity studies," *Drug Dev Ind Pharm,* vol. 31, pp. 757-768, 2005.

[46] M. T. Donato, A. Lahoz, J. V. Castell, and M. J. Gomez-Lechon, "Cell lines: a tool for in vitro drug metabolism studies," *Curr Drug Metab,* vol. 9, pp. 1-11, 2008.

[47] Y. Zhang, R. B. Sekar, A. D. McCulloch, and L. Tung, "Cell cultures as models of cardiac mechanoelectric feedback," *Prog Biophys Mol Biol,* vol. 97, pp. 367-382, 2008.

[48] R. Skalak and C. F. Fox, "Tissue engineering," Lake Tahoe, CA, 343, 1988.

[49] A. Abdel-Latif, R. Bolli, I. M. Tleyjeh, V. M. Montori, E. C. Perin, C. A. Hornung, E. K. Zuba-Surma, M. Al-Mallah, and B. Dawn, "Adult bone marrow-derived cells for cardiac repair: a systematic review and meta-analysis," *Arch Intern Med,* vol. 167, pp. 989-997, 2007.

[50] M. Perez-Ilzarbe, O. Agbulut, B. Pelacho, C. Ciorba, E. S. Jose-Eneriz, M. Desnos, A. A. Hagège, P. Aranda, E. J. Andreu, and P. Menasché, "Characterization of the paracrine effects of human skeletal myoblasts transplanted in infarcted myocardium," *Eur J Heart Fail,* vol. 10, pp. 1065-1072, 2008.

[51] M. Gnecchi, H. He, N. Noiseux, O. D. Liang, L. Zhang, F. Morello, H. Mu, L. G. Melo, R. E. Pratt, and J. S. Ingwall, "Evidence supporting paracrine hypothesis for Akt-modified mesenchymal stem cell-mediated cardiac protection and functional improvement," *FASEB J,* vol. 20, pp. 661-669, 2006.

[52] L. Timmers, S. K. Lim, F. Arslan, J. S. Armstrong, I. E. Hoefer, P. A. Doevendans, J. J. Piek, R. M. El Oakley, A. Choo, and C. N. Lee, "Reduction of myocardial infarct size by human mesenchymal stem cell conditioned medium," *Stem Cell Res,* vol. 1, pp. 129-137, 2008.

[53] V. F. M. Segers and R. T. Lee, "Stem-cell therapy for cardiac disease," *Nature*, vol. 451, pp. 937-942, 2008.

[54] M. A. Laflamme and C. E. Murry, "Regenerating the heart," *Nat Biotechnol*, vol. 23, pp. 845-856, 2005.

[55] P. Menasché, "Skeletal myoblasts as a therapeutic agent," *Prog Cardiovasc Dis*, vol. 50, pp. 7-17, 2007.

[56] P. Menasché, O. Alfieri, S. Janssens, W. McKenna, H. Reichenspurner, L. Trinquart, J. T. Vilquin, J. P. Marolleau, B. Seymour, and J. Larghero, "The Myoblast Autologous Grafting in Ischemic Cardiomyopathy (MAGIC) trial: first randomized placebo-controlled study of myoblast transplantation," *Circulation*, vol. 117, pp. 1189-1200, 2008.

[57] M. R. Abraham, C. A. Henrikson, L. Tung, M. G. Chang, M. Aon, T. Xue, R. A. Li, B. O'Rourke, and E. Marban, "Antiarrhythmic engineering of skeletal myoblasts for cardiac transplantation," *Circ Res*, vol. 97, pp. 159-167, 2005.

[58] C. E. Murry and G. Keller, "Differentiation of embryonic stem cells to clinically relevant populations: lessons from embryonic development," *Cell*, vol. 132, pp. 661-680, 2008.

[59] J. Nussbaum, E. Minami, M. A. Laflamme, J. A. I. Virag, C. B. Ware, A. Masino, V. Muskheli, L. Pabon, H. Reinecke, and C. E. Murry, "Transplantation of undifferentiated murine embryonic stem cells in the heart: teratoma formation and immune response," *FASEB J*, vol. 21, pp. 1345-1357, 2007.

[60] J. Yu, M. A. Vodyanik, K. Smuga-Otto, J. Antosiewicz-Bourget, J. L. Frane, S. Tian, J. Nie, G. A. Jonsdottir, V. Ruotti, and R. Stewart, "Induced pluripotent stem cell lines derived from human somatic cells," *Science*, vol. 318, pp. 1917-1920, 2007.

[61] K. Takahashi, K. Tanabe, M. Ohnuki, M. Narita, T. Ichisaka, K. Tomoda, and S. Yamanaka, "Induction of pluripotent stem cells from adult human fibroblasts by defined factors," *Cell*, vol. 131, pp. 861-872, 2007.

[62] T. J. Nelson, A. Martinez-Fernandez, and A. Terzic, "Induced pluripotent stem cells: developmental biology to regenerative medicine," *Nat Rev Cardiol*, vol. 7, pp. 700-710, 2010.

[63] K. Malliaras, M. Kreke, and E. Marbán, "The stuttering progress of cell therapy for heart disease," *Clin Pharmacol Ther*, vol. 90, pp. 532-541, 2011.

[64] K. H. Wu, X. M. Mo, Z. C. Han, and B. Zhou, "Stem cell engraftment and survival in the ischemic heart," *Ann Thorac Surg*, vol. 92, pp. 1917-1925, 2011.

[65] J. Terrovitis, R. Lautamäki, M. Bonios, J. Fox, J. M. Engles, J. Yu, M. K. Leppo, M. G. Pomper, R. L. Wahl, and J. Seidel, "Noninvasive quantification and optimization of acute cell retention by in vivo positron emission tomography after intramyocardial cardiac-derived stem cell delivery," *J Am Coll Cardiol,* vol. 54, pp. 1619-1626, 2009.

[66] D. Hou, E. A. S. Youssef, T. J. Brinton, P. Zhang, P. Rogers, E. T. Price, A. C. Yeung, B. H. Johnstone, P. G. Yock, and K. L. March, "Radiolabeled cell distribution after intramyocardial, intracoronary, and interstitial retrograde coronary venous delivery: implications for current clinical trials," *Circulation,* vol. 112, pp. I150-I156, 2005.

[67] T. P. Martens, A. F. G. Godier, J. J. Parks, L. Q. Wan, M. S. Koeckert, G. M. Eng, B. I. Hudson, W. Sherman, and G. Vunjak-Novakovic, "Percutaneous cell delivery into the heart using hydrogels polymerizing in situ," *Cell Transplant,* vol. 18, pp. 297-304, 2009.

[68] S. Dimmeler, A. M. Zeiher, and M. D. Schneider, "Unchain my heart: the scientific foundations of cardiac repair," *J Clin Invest,* vol. 115, pp. 572-583, 2005.

[69] M. C. Petersen, J. Lazar, H. J. Jacob, and T. Wakatsuki, "Tissue engineering: a new frontier in physiological genomics," *Physiol Genomics,* vol. 32, pp. 28-32, 2007.

[70] L. G. Griffith and M. A. Swartz, "Capturing complex 3D tissue physiology in vitro," *Nat Rev Mol Cell Biol,* vol. 7, pp. 211-224, 2006.

[71] A. G. Mikos, S. W. Herring, P. Ochareon, J. Elisseeff, H. H. Lu, R. Kandel, F. J. Schoen, M. Toner, D. Mooney, and A. Atala, "Engineering complex tissues," *Tissue Eng,* vol. 12, pp. 3307-3339, 2006.

[72] R. L. Carrier, M. Papadaki, M. Rupnick, F. J. Schoen, N. Bursac, R. Langer, L. E. Freed, and G. Vunjak-Novakovic, "Cardiac tissue engineering: Cell seeding, cultivation parameters, and tissue construct characterization," *Biotechnol Bioeng,* vol. 64, pp. 580-589, 1999.

[73] N. Bursac, M. Papadaki, R. J. Cohen, F. J. Schoen, S. R. Eisenberg, R. Carrier, G. Vunjak-Novakovic, and L. E. Freed, "Cardiac muscle tissue engineering: toward an in vitro model for electrophysiological studies," *Am J Physiol,* vol. 277, pp. 433-444, 1999.

[74] J. Leor, S. Aboulafia-Etzion, A. Dar, L. Shapiro, I. M. Barbash, A. Battler, Y. Granot, and S. Cohen, "Bioengineered cardiac grafts: A new approach to repair the infarcted myocardium?," *Circulation,* vol. 102, pp. III56-III61, 2000.

[75] R. K. Li, Z. Q. Jia, R. D. Weisel, D. A. G. Mickle, A. Choi, and T. M. Yau, "Survival and function of bioengineered cardiac grafts," *Circulation,* vol. 100, pp. II63-II69, 1999.

[76] T. Eschenhagen, C. Fink, U. Remmers, H. Scholz, J. Wattchow, J. Weil, W. Zimmermann, H. H. Dohmen, H. Schafer, and N. Bishopric, "Three-dimensional reconstitution of embryonic cardiomyocytes in a collagen matrix: a new heart muscle model system," *FASEB J,* vol. 11, pp. 683-694, 1997.

[77] A. Hansen, A. Eder, M. Bonstrup, M. Flato, M. Mewe, S. Schaaf, B. Aksehirlioglu, A. Schworer, J. Uebeler, and T. Eschenhagen, "Development of a drug screening platform based on engineered heart tissue," *Circ Res,* vol. 107, pp. 35-44, 2010.

[78] C. Fink, S. Ergun, D. Kralisch, U. T. E. Remmers, J. Weil, and T. Eschenhagen, "Chronic stretch of engineered heart tissue induces hypertrophy and functional improvement," *FASEB J,* vol. 14, pp. 669-679, 2000.

[79] H. Naito, I. Melnychenko, M. Didie, K. Schneiderbanger, P. Schubert, S. Rosenkranz, T. Eschenhagen, and W. H. Zimmermann, "Optimizing engineered heart tissue for therapeutic applications as surrogate heart muscle," *Circulation,* vol. 114, pp. I72-I78, 2006.

[80] W. H. Zimmermann, K. Schneiderbanger, P. Schubert, M. Didie, F. Munzel, J. F. Heubach, S. Kostin, W. L. Neuhuber, and T. Eschenhagen, "Tissue engineering of a differentiated cardiac muscle construct," *Circ Res,* vol. 90, pp. 223-230, 2002.

[81] W. H. Zimmermann, M. Didie, G. H. Wasmeier, U. Nixdorff, A. Hess, I. Melnychenko, O. Boy, W. L. Neuhuber, M. Weyand, and T. Eschenhagen, "Cardiac grafting of engineered heart tissue in syngenic rats," *Circulation,* vol. 106, pp. 151-157, 2002.

[82] Y. Yildirim, H. Naito, M. Didie, B. C. Karikkineth, D. Biermann, T. Eschenhagen, and W. H. Zimmermann, "Development of a biological ventricular assist device: Preliminary data from a small animal model," *Circulation,* vol. 116, pp. I16-I23, 2007.

[83] W. H. Zimmermann, I. Melnychenko, G. Wasmeier, M. Didié, H. Naito, U. Nixdorff, A. Hess, L. Budinsky, K. Brune, and B. Michaelis, "Engineered heart tissue grafts improve systolic and diastolic function in infarcted rat hearts," *Nat Med,* vol. 12, pp. 452-458, 2006.

[84] S. Schaaf, A. Shibamiya, M. Mewe, A. Eder, A. Stöhr, M. N. Hirt, T. Rau, W. H. Zimmermann, L. Conradi, and T. Eschenhagen, "Human engineered heart tissue

as a versatile tool in basic research and preclinical toxicology," *PloS One,* vol. 6, p. e26397, 2011.

[85] T. Shimizu, M. Yamato, Y. Isoi, T. Akutsu, T. Setomaru, K. Abe, A. Kikuchi, M. Umezu, and T. Okano, "Fabrication of pulsatile cardiac tissue grafts using a novel 3-dimensional cell sheet manipulation technique and temperature-responsive cell culture surfaces," *Circ Res,* vol. 90, p. e40, 2002.

[86] T. Shimizu, H. Sekine, J. Yang, Y. Isoi, M. Yamato, A. Kikuchi, E. Kobayashi, and T. Okano, "Polysurgery of cell sheet grafts overcomes diffusion limits to produce thick, vascularized myocardial tissues," *FASEB J,* vol. 20, pp. 708-710, 2006.

[87] H. Sekine, T. Shimizu, I. Dobashi, K. Matsuura, N. Hagiwara, M. Takahashi, E. Kobayashi, M. Yamato, and T. Okano, "Cardiac cell sheet transplantation improves damaged heart function via superior cell survival in comparison with dissociated cell injection," *Tissue Eng Part A.,* vol. 17, pp. 2973-2980, 2011.

[88] K. A. Robinson, J. Li, M. Mathison, A. Redkar, J. Cui, N. A. F. Chronos, R. G. Matheny, and S. F. Badylak, "Extracellular matrix scaffold for cardiac repair," *Circulation,* vol. 112, pp. I135-I143, 2005.

[89] H. C. Ott, T. S. Matthiesen, S. K. Goh, L. D. Black, S. M. Kren, T. I. Netoff, and D. A. Taylor, "Perfusion-decellularized matrix: using nature's platform to engineer a bioartificial heart," *Nat Med,* vol. 14, pp. 213-221, 2008.

[90] K. Bilodeau and D. Mantovani, "Bioreactors for tissue engineering: focus on mechanical constraints. A comparative review," *Tissue Eng,* vol. 12, pp. 2367-2383, 2006.

[91] I. Martin, D. Wendt, and M. Heberer, "The role of bioreactors in tissue engineering," *Trends Biotechnol,* vol. 22, pp. 80-86, 2004.

[92] H. C. Chen and Y. C. Hu, "Bioreactors for tissue engineering," *Biotechnol Lett,* vol. 28, pp. 1415-1423, 2006.

[93] R. L. Carrier, M. Rupnick, R. Langer, F. J. Schoen, L. E. Freed, and G. Vunjak-Novakovic, "Perfusion improves tissue architecture of engineered cardiac muscle," *Tissue Eng,* vol. 8, pp. 175-188, 2002.

[94] M. J. A. van Luyn, R. A. Tio, X. J. Gallego y van Seijen, J. A. Plantinga, L. de Leij, M. J. L. DeJongste, and P. B. van Wachem, "Cardiac tissue engineering: characteristics of in unison contracting two-and three-dimensional neonatal rat ventricle cell (co)-cultures," *Biomaterials,* vol. 23, pp. 4793-4801, 2002.

[95] R. E. Akins, R. A. Boyce, M. L. Madonna, N. A. Schroedl, S. R. Gonda, T. A. McLaughlin, and C. R. Hartzell, "Cardiac organogenesis in vitro: reestablishment of three-dimensional tissue architecture by dissociated neonatal rat ventricular cells," *Tissue Eng,* vol. 5, pp. 103-118, 1999.

[96] A. Lichtenberg, G. Dumlu, T. Walles, M. Maringka, S. Ringes-Lichtenberg, A. Ruhparwar, H. Mertsching, and A. Haverich, "A multifunctional bioreactor for three-dimensional cell (co)-culture," *Biomaterials,* vol. 26, pp. 555-562, 2005.

[97] M. Radisic, A. Marsano, R. Maidhof, Y. Wang, and G. Vunjak-Novakovic, "Cardiac tissue engineering using perfusion bioreactor systems," *Nat Protoc,* vol. 3, pp. 719-738, 2008.

[98] M. Radisic, H. Park, F. Chen, J. E. Salazar-Lazzaro, Y. Wang, R. Dennis, R. Langer, L. E. Freed, and G. Vunjak-Novakovic, "Biomimetic approach to cardiac tissue engineering: oxygen carriers and channeled scaffolds," *Tissue Eng,* vol. 12, pp. 2077-2091, 2006.

[99] Z. Feng, T. Matsumoto, Y. Nomura, and T. Nakamura, "An electro-tensile bioreactor for 3D culturing of cardiomyocytes," *IEEE Eng Med Biol Mag,* vol. 24, pp. 73-79, 2005.

[100] N. Tandon, C. Cannizzaro, P. H. G. Chao, R. Maidhof, A. Marsano, H. T. H. Au, M. Radisic, and G. Vunjak-Novakovic, "Electrical stimulation systems for cardiac tissue engineering," *Nat Protoc,* vol. 4, pp. 155-173, 2009.

[101] C. Cannizzaro, N. Tandon, E. Figallo, H. Park, S. Gerecht, M. Radisic, N. Elvassore, and G. Vunjak-Novakovic, "Practical aspects of cardiac tissue engineering with electrical stimulation," *Methods Mol Med,* vol. 140, pp. 291-307, 2007.

[102] Y. Kawahara, K. Yamaoka, M. Iwata, M. Fujimura, T. Kajiume, T. Magaki, M. Takeda, T. Ide, K. Kataoka, and M. Asashima, "Novel electrical stimulation sets the cultured myoblast contractile function to 'on'," *Pathobiology,* vol. 73, pp. 288-294, 2006.

[103] P. Akhyari, P. W. M. Fedak, R. D. Weisel, T. Y. J. Lee, S. Verma, D. A. G. Mickle, and R. K. Li, "Mechanical stretch regimen enhances the formation of bioengineered autologous cardiac muscle grafts," *Circulation,* vol. 106, pp. I137-I142, 2002.

[104] R. K. Birla, Y. C. Huang, and R. G. Dennis, "Development of a novel bioreactor for the mechanical loading of tissue-engineered heart muscle," *Tissue Eng,* vol. 13, pp. 2239-2248, 2007.

[105] J. Zhuang, K. A. Yamada, J. E. Saffitz, and A. G. Kleber, "Pulsatile stretch remodels cell-to-cell communication in cultured myocytes," *Circ Res,* vol. 87, pp. 316-322, 2000.

[106] M. Gonen-Wadmany, L. Gepstein, and D. Seliktar, "Controlling the cellular organization of tissue-engineered cardiac constructs," *Ann NY Acad Sci,* vol. 1015, pp. 299-311, 2004.

[107] M. Radisic, V. G. Fast, O. F. Sharifov, R. K. Iyer, H. Park, and G. Vunjak-Novakovic, "Optical mapping of impulse propagation in engineered cardiac tissue," *Tissue Eng Part A,* vol. 15, pp. 851-860, 2009.

[108] M. Radisic, H. Park, S. Gerecht, C. Cannizzaro, R. Langer, and G. Vunjak-Novakovic, "Biomimetic approach to cardiac tissue engineering," *Philos Trans R Soc Lond B Biol Sci,* vol. 362, pp. 1357-1368, 2007.

[109] L. G. Griffith and G. Naughton, "Tissue engineering--current challenges and expanding opportunities," *Science,* vol. 295, pp. 1009-1014, 2002.

[110] J. J. Pancrazio, F. Wang, and C. A. Kelley, "Enabling tools for tissue engineering," *Biosens Bioelectron,* vol. 22, pp. 2803-2811, 2007.

[111] R. A. Lasher, F. B. Sachse, and R. W. Hitchcock, "Towards Online Monitoring of Engineered Tissue Using Confocal Microscopy and Image Processing," in *Society for Biomaterials,* San Antonio, TX, 2009.

[112] R. Zeller, "Fixation, embedding, and sectioning of tissues, embryos, and single cells," in *Curr Protoc Mol Biol,* 2001.

[113] Y. S. Zhao, C. Y. Wang, D. X. Li, X. Z. Zhang, Y. Qiao, X. M. Guo, X. L. Wang, C. M. Dun, L. Z. Dong, and Y. Song, "Construction of a Unidirectionally Beating 3Dimensional Cardiac Muscle Construct," *J Heart Lung Transplant,* vol. 24, pp. 1091-1097, 2005.

[114] J. D. Fromstein, P. W. Zandstra, C. Alperin, D. Rockwood, J. F. Rabolt, and K. A. Woodhouse, "Seeding bioreactor-produced embryonic stem cell-derived cardiomyocytes on different porous, degradable, polyurethane scaffolds reveals the effect of scaffold architecture on cell morphology," *Tissue Eng Part A,* vol. 14, pp. 369-378, 2008.

[115] R. Yuste, "Fluorescence microscopy today," *Nat Methods,* vol. 2, pp. 902-904, 2005.

[116] N. C. Shaner, P. A. Steinbach, and R. Y. Tsien, "A guide to choosing fluorescent proteins," *Nat Methods,* vol. 2, pp. 905-909, 2005.

[117] E. Savio-Galimberti, F. B. Sachse, J. I. Goldhaber, C. Soeller, and J. H. Bridge, "Relationship of ryanodine receptors to the sarcolemma in rabbit ventricular myocytes," in *Biophys J (Annual Meeting Abstracts)*, 2009.

[118] G. Sands, M. Trew, D. Hooks, I. Le Grice, A. Pullan, and B. Smaill, "Constructing a tissue-specific model of ventricular microstructure," in *Conf Proc IEEE Eng Med Biol Soc*, vol. 5, pp. 3589-3592, 2004.

[119] B. H. Smaill, I. J. LeGrice, D. A. Hooks, A. J. Pullan, B. J. Caldwell, and P. J. Hunter, "Cardiac structure and electrical activation: Models and measurement," *Clin Exp Pharmacol Physiol*, vol. 31, pp. 913-919, 2004.

[120] D. A. Hooks, K. A. Tomlinson, S. G. Marsden, I. J. LeGrice, B. H. Smaill, A. J. Pullan, and P. J. Hunter, "Cardiac microstructure implications for electrical propagation and defibrillation in the heart," *Circ Res*, vol. 91, pp. 331-338, 2002.

[121] E. Savio-Galimberti, J. Frank, M. Inoue, J. I. Goldhaber, M. B. Cannell, J. H. Bridge, and F. B. Sachse, "Novel features of the rabbit transverse tubular system revealed by quantitative analysis of three-dimensional reconstructions from confocal images," *Biophys J*, vol. 95, pp. 2053-2062, 2008.

[122] F. B. Sachse, E. Savio-Galimberti, J. I. Goldhaber, and J. H. Bridge, "Towards computational modeling of excitation-contraction coupling in cardiac myocytes: Reconstruction of structures and proteins from confocal imaging," in *Pacific Symposium on Biocomputing*, vol. 14, pp. 328-339, 2009.

[123] J. A. Conchello and J. W. Lichtman, "Optical sectioning microscopy," *Nat Methods*, vol. 2, pp. 920-931, 2005.

[124] M. Minsky, "Memoir on inventing the confocal scanning microscope," *Scanning*, vol. 10, pp. 128-138, 1988.

[125] A. Diaspro, *Confocal and Two-Photon Microscopy: Foundations, Applications, and Advances*. New York: Wiley, 2002.

[126] F. Berier, S. Bourriaux, M. Genet, B. Viellerobe, A. Loiseau, and B. Abrat, "Miniaturized focusing optical head in particular for endoscope," Mauna Kea Technologies (Paris FR), 2002.

[127] S. Anandasabapathy, "Endoscopic imaging: emerging optical techniques for the detection of colorectal neoplasia.," *Curr Opin Gastroenterol*, vol. 24, pp. 64-69, 2008.

[128] B. Viellerobe, M. Genet, F. Berier, F. Lacombe, A. Perchant, G. Le Goualher, S. Marti, and S. Bourriaux, "Confocal imaging equipment in particular for endoscope," Mauna Kea Technologies (Paris FR), 2002.

[129] R. Kiesslich and M. F. Neurath, "Endoscopic confocal imaging," *Clin Gastroenterol Hepato,* vol. 3, pp. 58-60, 2005.

[130] M. Goetz, A. Hoffman, P. R. Galle, M. F. Neurath, and R. Kiesslich, "Confocal laser endoscopy: new approach to the early diagnosis of tumors of the esophagus and stomach," *Future Oncol.,* vol. 2, pp. 469-476, 2006.

[131] A. L. Polglase, W. J. McLaren, S. A. Skinner, R. Kiesslich, M. F. Neurath, and P. M. Delaney, "A fluorescence confocal endomicroscope for in vivo microscopy of the upper-and the lower-GI tract," *Gastrointest Endosc,* vol. 62, pp. 686-695, 2005.

[132] R. C. Gonzalez and R. E. Woods, *Digital Image Processing*. Reading, MA: Addison-Wesley, 1992.

[133] E. Savio, J. I. Goldhaber, J. H. B. Bridge, and F. B. Sachse, "A framework for analyzing confocal images of transversal tubules in cardiomyocytes," *Lect Notes Comput Sci,* vol. 4466, pp. 110-119, 2007.

[134] S. Bolte and F. P. Cordelieres, "A guided tour into subcellular colocalization analysis in light microscopy," *J Microsc,* vol. 224, pp. 213-232, 2006.

[135] W. H. Richardson, "Bayesian-based iterative method of image restoration," *J. Opt. Soc. Am,* vol. 62, pp. 55-59, 1972.

[136] J. P. Rigaut and J. Vassy, "High-resolution three-dimensional images from confocal scanning laser microscopy. Quantitative study and mathematical correction of the effects from bleaching and fluorescence attenuation in depth," *Anal Quant Cytol Histol,* vol. 13, pp. 223-232, 1991.

[137] J. B. Pawley, *Handbook of Biological Confocal Microscopy*. New York: Springer Verlag, 2006.

[138] C. Kervrann, D. Legland, and L. Pardini, "Robust incremental compensation of the light attenuation with depth in 3D fluorescence microscopy," *J Microsc,* vol. 214, pp. 297-314, 2004.

[139] M. Capek, J. Janácek, and L. Kubínová, "Methods for compensation of the light attenuation with depth of images captured by a confocal microscope," *Microsc Res Tech,* vol. 69, pp. 624-635, 2006.

[140] D. E. S. Ortiz, "Segmentation of confocal microscope images of cell nuclei in thick tissue sections," *J Microsc,* vol. 193, pp. 212-226, 1999.

[141] J. B. Xavier, A. Schnell, S. Wuertz, R. Palmer, D. C. White, and J. S. Almeida, "Objective threshold selection procedure (OTS) for segmentation of scanning laser confocal microscope images," *J Microbiol Methods*, vol. 47, pp. 169-180, 2001.

[142] G. Sands, S. Goo, D. Gerneke, I. LeGrice, and D. Loiselle, "The collagenous microstructure of cardiac ventricular trabeculae carneae," *J Struct Biol*, vol. 173, pp. 110-116, 2010.

[143] M. S. Spach, J. F. Heidlage, R. C. Barr, and P. C. Dolber, "Cell size and communication: Role in structural and electrical development and remodeling of the heart," *Heart Rhythm*, vol. 1, pp. 500-515, 2004.

CHAPTER 2

TOWARDS MODELING OF CARDIAC MICRO-STRUCTURE WITH CATHETER- BASED CONFOCAL MICROSCOPY: A NOVEL APPROACH FOR DYE DELIVERY AND TISSUE CHARACTERIZATION

Reprinted with permission from *IEEE Trans Med Imaging*. 2009;28(8):1156-64.

1156 IEEE TRANSACTIONS ON MEDICAL IMAGING, VOL. 28, NO. 8, AUGUST 2009

Towards Modeling of Cardiac Micro-Structure With Catheter-Based Confocal Microscopy: A Novel Approach for Dye Delivery and Tissue Characterization

Richard A. Lasher, Robert W. Hitchcock, and Frank B. Sachse*, *Member, IEEE*

***Abstract*—This work presents a methodology for modeling of cardiac tissue micro-structure. The approach is based on catheter-based confocal imaging systems, which are emerging as tools for diagnosis in various clinical disciplines. A limitation of these systems is that a fluorescent marker must be available in sufficient concentration in the imaged region. We introduce a novel method for the local delivery of fluorescent markers to cardiac tissue based on a hydro-gel carrier brought into contact with the tissue surface. The method was tested with living rabbit cardiac tissue and applied to acquire three-dimensional image stacks with a standard inverted confocal microscope and two-dimensional images with a catheter-based confocal microscope. We processed these image stacks to obtain spatial models and quantitative data on tissue microstructure. Volumes of atrial and ventricular myocytes were 4901 ± 1713 and 10299 ± 3598 μm^3 (mean$\pm$sd), respectively. Atrial and ventricular myocyte volume fractions were $72.4 \pm 4.7\%$ and $79.7 \pm 2.9\%$ (mean $\pm$ sd), respectively. Atrial and ventricular myocyte density was 165571 ± 55836 and 86957 ± 32280 cells/mm^3 (mean $\pm$ sd), respectively. These statistical data and spatial descriptions of tissue microstructure provide important input for modeling studies of cardiac tissue function. We propose that the described methodology can also be used to characterize diseased tissue and allows for personalized modeling of cardiac tissue.**

***Index Terms*—Biomedical image processing, cardiac tissue, confocal microscopy, fluorescent labeling, patient-specific modeling.**

I. Introduction

ADVANCES in scanning confocal microscopy combined with new developments in fluorescent markers have made it possible to image structure and function of living cells and tissue [1], [2]. Scanning confocal microscopy is based on optical sectioning and fluorescence, and has several advantages over traditional microscopic imaging modalities [3]. In particular, confocal microscopy features the ability to control the depth of field, reject out-of-focus light, and collect sequential optical sections from thick specimens [4]. These advantages have established confocal microscopy as a major research technique used to gain insights into cell and tissue physiology and pathophysiology. Furthermore, image data obtained from confocal microscopy enables spatial modeling of cells and tissues [5]–[7]. Recently, catheter-based confocal microscopic systems have been developed, which allow for *in vivo* imaging [8]–[11]. In principle, these systems allow microscopic imaging inside living subjects. Hence, these systems have been proposed for clinical applications, in particular for diagnosis of human diseases [8]–[11].

This work is focused on confocal microscopic imaging of cardiac tissue, its spatial modeling, and quantitative analysis. Cardiac tissue can be viewed as a composite material comprised of fluids and cells, including myocytes, fibroblasts, endothelial, vascular smooth muscle, and neuronal cells. Myocytes occupy most of the volume in cardiac tissue and are responsible for cardiac contraction. The (interstitial) space between cardiac cells is filled with fluid and an interconnected extracellular matrix comprised mostly of collagen and capillary vessels [12], [13]. Quantity, density, and morphology of cardiac cells vary significantly during development, amongst species, for each cardiac tissue and in heart disease [14]–[16]. Many diseases, such as hypertrophy, atrophy, infarction, and ischemia, are known to be associated with alterations in cell geometry and density. For instance, in cardiac hypertrophy, human epicardial left ventricular myocytes have been shown to increase in length, width, area, and volume by approximately 9%, 28%, 39%, and 78%, respectively, and rabbit right ventricular myocytes are known to increase in length and width by approximately 7.5% and 36%, respectively [17]. In atrophic hearts, left ventricular myocytes decrease in volume by 50%–75%, with little change in myocyte length [18]. Cardiac diseases are also known to alter the extracellular environment. Following myocardial infarction, fibrosis (excessive deposition of extracellular matrix mediated by fibroblasts) occurs not only in the infarcted region, but in the surrounding regions as well [19]. Furthermore, early stages of ischemia are known to decrease the extracellular resistance, which is indicative of reduced interstitial space [20]. A more comprehensive understanding of these pathologic cellular and tissue alterations could allow the recently developed catheter-

Manuscript received October 06, 2008; revised February 23, 2009. First published March 24, 2009; current version published July 29, 2009. This work was supported in part by the Richard A. and Nora Eccles Fund for Cardiovascular Research, in part by the Nora Eccles Treadwell Foundation, and in part by a microgrant from the Technology Commercialization Office, University of Utah. *Asterisk indicates corresponding author.*

R. A. Lasher and R. W. Hitchcock are with the Department of Bioengineering, University of Utah, Salt Lake City, UT 84112 USA.

*F. B. Sachse is with the Cardiovascular Research and Training Institute, University of Utah, Salt Lake City, UT 84112 USA and also with the Department of Bioengineering, University of Utah, Salt Lake City, UT 84112 USA (e-mail: fs@cvrti.utah.edu).

Color versions of one or more of the figures in this paper are available online at http://ieeexplore.ieee.org.

Digital Object Identifier 10.1109/TMI.2009.2017376

based confocal systems and optical imaging techniques to provide a new set of diagnostic tools in cardiology.

In previous studies, pathologic alterations of cardiac microstructure have been characterized *ex vivo* with confocal microscopy [6], [7], [21], [22]. In principle, the recently developed catheter-based confocal imaging systems enable similar studies to be performed *in vivo*. However, the application of confocal microscopy requires that fluorescent dye for labeling of proteins or structures is available in sufficient concentration in the region of interest. Dye delivery is commonly a time-consuming immunochemistry procedure, requiring excision, fixation, and sectioning of tissue as well as cell membrane disruption [23]. In particular, *in vivo* dye delivery is an unresolved issue that impedes the application of catheter-based confocal imaging in these studies.

Image data from both living and fixed tissue specimens have been used to develop models that describe physical and physiological properties of cardiac tissue. For instance, models that describe mechanical and electrophysiological properties in normal and diseased cells and tissues have been developed [24], [25]. Most of these models do not directly account for the detailed tissue microstructure, but describe tissue properties with lumped parameters or homogenization approaches [24], [26]. A small number of models have been introduced, which are based on an analytical description of microstructure [27] or on two-dimensional microscopic images [5], [21].

In this study, we describe an approach for modeling and analyzing cardiac tissue with confocal microscopy. The approach is characterized with studies on living cardiac tissue from rabbits; specifically, dissected right ventricular papillary muscle, subepicardial ventricular and atrial tissue. We introduce a novel method for fluorescent dye delivery, which allows for acquisition of three-dimensional stacks of confocal images of living cardiac tissue. These image stacks are processed to remove background signals and correct for depth-dependent attenuation. Furthermore, image stacks are deconvolved and processed to yield detailed spatial models and quantitative data on cardiac microstructure. Our quantitative values on myocyte geometry are compared with literature values. In addition, we characterized the method for local dye delivery with a catheter-based confocal system and a living rabbit heart preparation. We propose that the described methodology can be used for personalized modeling of cardiac tissue microstructure and diagnosis based on catheter-based confocal microscopy.

II. Materials and Methods

A. Tissue Section Preparation

All experiments were approved by the Institutional Animal Care and Use Committee (IACUC) at the University of Utah. Adult rabbits were anesthetized with pentobarbital (30 mg/kg) and anticoagulated with heparin (2500 USP units/kg). Following thoracotomy hearts were quickly excised and placed in a modified oxygenated Tyrode's solution (in mM: 126 NaCl, 11 Dextrose, 0.1 $CaCl_2$, 13.2 KCl, 1 $MgCl_2$, 12.9 NaOH, 24 HEPES) at room temperature. The hearts were dissected into tissue sections of three types: right ventricular papillary muscle ($\approx$1 mm $\times$ 1 mm $\times$ 5 mm), subepicardial ventricular ($\approx$6 mm $\times$ 2 mm) and atrial tissue ($\approx$6 mm $\times$ 2 mm). The sections were secured to a polycarbonate holder with sutures as shown in Fig. 1 and stored in the solution until imaging.

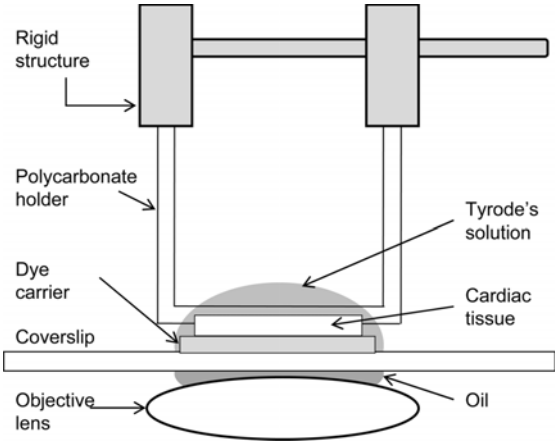

Fig. 1. Experimental setup for confocal imaging of cardiac tissue.

B. Image Acquisition

Images were obtained within 6 h of heart isolation. Tissue sections were covered by oxygenated Tyrode's solution during the imaging (Fig. 1). Tissue sections were imaged on an 8-bit BioRad MRC-1024 laser-scanning confocal microscope (BioRad, Hercules, CA) with a 40x oil-immersion objective lens (Nikon, Tokyo, Japan). Three-dimensional image stacks with a spatial resolution of 200 $\times$ 200 $\times$ 200 nm were obtained with a field-of–view ($X \times Y$) of 204.8 $\times$ 153.6 μm extending up to 80 μm into the myocardium (Z direction). The Z-axis was parallel to the laser beam direction.

C. Dye Delivery

Thin hydrogel slices (4 mm $\times$ 4 mm $\times$ 40 μm thick) were created using 6.5% agar (GenePure LE Agarose, ISC BioExpress, Kaysville, UT) in water. These slices were placed in solutions of fluorescent dyes and the dye was allowed to diffuse into the agar hydrogel. Dextran-conjugated, lysine-fixable Texas Red with a molecular weight of 3 kDa and excitation/emission wavelengths of 595/615 nm was used at concentrations of 6–12 mg/mL (Molecular Probes, Eugene, OR). This dye and other dextran-conjugated dyes allow for specific labeling of the extracellular space [28], [29]. An imaging chamber was created by cutting an aperture from the bottom of a polystyrene weighing dish and gluing a size #0 glass slide over the opening. The dye-loaded hydrogel slice was placed on the glass slide and dye was delivered by gently pressing the tissue onto the slide. Precautions were taken to ensure that the tissue sample was not compressed in the imaged region. We selected image regions with a distance of at least 10 μm between the glass slide and tissue surface. Images were acquired by imaging through the glass slide and hydrogel (Fig. 1).

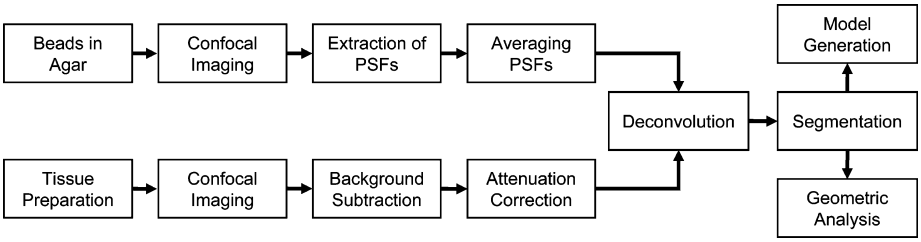

Fig. 2. Schematic of experimental and processing methods.

D. Measurement of Point Spread Functions and Deconvolution

Image stacks were deconvolved with the iterative Richardson–Lucy algorithm using a measured point spread function (PSF) as previously described [30]. Briefly, the response g of an imaging system to given sources can be described by convolution of the source image f with the point spread function h

$$g(x) = (f * h)(x) = \int\int\int_{-\infty}^{\infty} f(x')h(x - x')\mathrm{d}x'. \quad (1)$$

The iterative Richardson–Lucy algorithm was used to reconstruct the source image f

$$g_{n+1} = g_n \left(\frac{g_0}{g_n * h} \otimes h \right) \quad (2)$$

with the cross-correlation operator $\otimes$ and $g_0 \equiv g$. The three-dimensional PSF was characterized by imaging 100-nm fluorescent beads embedded in agar. Images of 15 beads were extracted, aligned and averaged to obtain the PSF, which allowed us to quantitatively characterize our imaging approach. Finally, the PSF was filtered by applying an average filter and resampled with a resolution of 200 nm $\times$ 200 nm $\times$ 200 nm. The PSF was applied to deconvolve the image stacks.

E. Image Processing, Segmentation and Geometric Analysis

Signal-to-noise ratios in the raw images were estimated to characterize image stacks. Regions of 300 voxels were sampled inside myocytes to calculate variances of signal intensity and in the extracellular space to calculate mean signal intensity. The signal-to-noise ratio was calculated from the mean signal intensity divided by the variance.

Raw image stacks were processed using a combination of C++ and MatLab software (MathWorks, Natick, MA) to remove background signals and correct for depth-dependent attenuation (Fig. 2). The background signal was estimated by averaging signals in small regions where the expected intensity is zero (i.e., inside myocytes). Depth-dependent attenuation of signal intensity was calculated by selecting lines in the Z-axis (laser beam) direction with the smallest standard deviation of the associated intensity. Intensities along these lines were fit to an exponential function using least square optimization to obtain a slice-wise scaling factor as a function of depth.

Myocytes were segmented by manually deforming a surface mesh [31] followed by iterative thresholding. An initially ellipsoid-shaped mesh comprised of 5120 triangles was wrapped around each myocyte in the field of interest (Fig. 6). Histograms of voxel intensities were created for the volume enclosed by each mesh to calculate the mode and standard deviation of voxel intensities. Threshold values were chosen independently for each myocyte based on the calculated mode and standard deviation to distinguish between intramyocyte and extracellular spaces.

After thresholding, geometric analysis was performed on the extracted whole myocytes. Principal component analysis (PCA) was used to determine the principal axis of each segmented myocyte [32]. A bounding box was created around each myocyte based on the PCA as illustrated in Fig. 6(d). The bounding box dimensions in direction of the first, second, and third principal axis were considered to be the myocyte length, width, and height, respectively. Myocyte volume was calculated by counting the intramyocyte voxels. Average cross-sectional area was determined by dividing cell volume by length. The volume fraction of tissue occupied by myocytes was determined by sampling random volumes of 300 $\times$ 300 $\times$ 30 voxels within regions of the image stack where all myocytes were segmented. Myocyte density was defined as mean of the myocyte volume fraction (MVF) divided by the volume of each cell (V_i)

$$\text{Myocyte Density} = \frac{1}{n} \sum \frac{\text{MVF}}{V_i}. \quad (3)$$

F. Catheter-Based Confocal Imaging of Heart Preparations

For some imaging studies, excised hearts were mounted and perfused with the modified Tyrode's solution (above) at 8 mL/min retrogradely through the aorta using the Langendorff method [33]. Two-dimensional images with a field-of-view of 176.3 $\times$ 124.9 μm and a lateral resolution of 0.48 μm were acquired from the Langendorff preparation with a catheter-based confocal system (FCM1000, Leica, Wetzlar, Germany) and a microprobe (M/30). The microprobe tip diameter was 4.2 mm and the working distance was 30 μm. A hydrogel dye carrier was configured as an agar sheath that fit over the catheter tip, as shown in Fig. 3(a).

III. Results

A. Dye Delivery and Image Acquisition

We characterized our approach for dye delivery and image acquisition in experimental studies with living cardiac tissue of various types. Upon gently pressing the tissue sections onto the hydrogel carrier, the dextran-conjugated Texas Red dye diffused

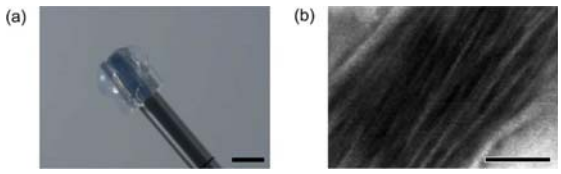

Fig. 3. Imaging with catheter-based confocal microscopy system (Leica FCM 1000). (a) M/30 confocal microprobe with hydrogel carrier loaded with dye. (b) Image of atrial tissue acquired with catheter-based confocal microscopy system and the modified microprobe. Scale: 5 mm in (a) and 50 μm in (b).

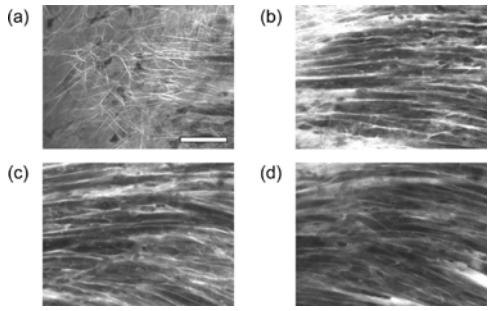

Fig. 4. Exemplary raw *XY* images from a three-dimensional stack of atrial tissue. The images are from the (a) epicardial surface and a depth of (b) 10 μm, (c) 20 μm, and (d) 30 μm into the myocardium. Scale: 50 μm in (a) applies to (a)–(d).

rapidly through the endo- or epicardial layers and into the myocardium. The dye was immediately available in sufficient concentration for confocal imaging of the cardiac microstructure.

Exemplary two-dimensional images of atrial and ventricular tissue sections acquired with the BioRad confocal microscope are shown in Figs. 4 and 5, respectively. These images originate from three-dimensional stacks covering approximately 1 μm outside of the tissue surface and up to 80 μm into the myocardium. Fluorescence appeared to be associated with clefts between cells (interstitial space), collagen fibers, transverse tubules and capillary vessels; whereas darker regions appeared to be associated with cells. Image slices through the epicardial and endocardial network of thin collagen fibers in atrial and ventricular tissue are shown in Fig. 4(a) and Fig. 5(a), respectively. The fibers are brighter than their surroundings and appear to be, to some degree, orientated parallel to the myocytes. The image through the ventricular endocardium [Fig. 5(a)] includes endothelial cells. Image slices into atrial and ventricular myocardium are presented in Fig. 4(b)–(d) and Fig. 5(b)–(d), respectively. These image slices are from depths of 10, 20, and 30 μm into the myocardium with respect to the epicardial or endocardial surface layer [Fig. 4(a) and Fig. 5(a)]. The density of the network of collagen fibers appeared to be larger in the endo- and epicardium than within the myocardium. Furthermore, images extending further into the myocardium exhibited less overall fluorescence.

Optical properties of the BioRad confocal microscopy system were characterized by measurement of PSFs as described above. The PSF exhibited full widths at half maximum of 0.30 μm in the *XY* plane (transverse to the laser-beam) and 1.85 μm in the Z direction (parallel to the laser beam).

We also acquired two-dimensional images with a catheter-based confocal microscope (FCM1000, Leica Microsystems, Wetzlar, Germany). The dye carrier was attached to the catheter tip and gently pressed on the epicardial surface of the atria and ventricles of a Langendorff-perfused heart. An exemplary two-dimensional image of atrial tissue is shown in Fig. 3(b). As in our studies of tissue sections with the BioRad confocal microscope, the dye was immediately available for imaging. High and low fluorescence intensities were associated with the extra- and intracellular spaces, respectively.

B. Image Quantification and Modeling of Tissue

We applied methods of digital image processing and analysis to quantitatively describe and model cardiac tissue microstructure from three-dimensional image data. For this purpose, we acquired 19 image stacks from a total of nine rabbits for subsequent analysis. Fourteen of these stacks were rejected from analysis due to low signal-to-noise ratios, discontinuities within the image stack by motion and/or poor tissue quality. Signal-to-noise ratios below 3 were considered low. We removed background signals, corrected for depth-dependent attenuation, and deconvolved the image stacks as described. Fig. 5(e) and (f) illustrates the effect of this processing on the image stacks. Processed image stacks exhibit fine details of myocytes such as the transverse tubular system [Fig. 5(f)], which were difficult to identify in the unprocessed image data [Fig. 5(e)].

Individual myocytes were segmented from three-dimensional image stacks (Fig. 6), which allowed for subsequent spatial modeling (Figs. 7 and 8) and quantitative analysis of myocytes (Tables I and II). Segmentation was performed on 50 atrial myocytes and 36 ventricular myocytes. Quantitative analysis was only performed on whole myocytes, which included 28 atrial myocytes and 20 ventricular myocytes.

An exemplary segmentation of a single myocyte from a three-dimensional stack of atrial tissue is shown in Fig. 6. The manually deformed surface mesh is illustrated in three orthogonal planes in Fig. 6(a)–(c). Threshold values to distinguish between intramyocyte and extracellular space were chosen to be the mode plus two standard deviations of signal intensity for each segmented myocyte. Fig. 6(d) shows the segmented myocyte after thresholding and in a bounding box aligned to the principal axes of the myocyte. The dimensions of the bounding box determined the length, width and height of the myocyte. Three-dimensional spatial models of segmented myocytes from three-dimensional stacks of atrial and ventricular tissue are shown in Figs. 7 and 8, respectively. Fig. 7(d) shows a three-dimensional visualization of the atrial model overlaid with orthogonal confocal images.

Quantitative analysis revealed mean and standard deviation $(\text{mean} \pm \text{sd})$ of lengths, widths and heights of atrial myocytes to be $105.0 \pm 10.6, 13.1 \pm 1.7$, and 9.7 ± 1.6 μm, respectively, and ventricular myocytes to be $112.3 \pm 14.3, 18.4 \pm 2.3$, and 14.1 ± 2.7 μm, respectively (Table I). Average volumes of atrial and ventricular myocytes were 4901 ± 1713 and 10299 ± 3598 μm^3, respectively. Furthermore, the myocyte volume fractions for atrial and ventricular tissue were $72.4 \pm$

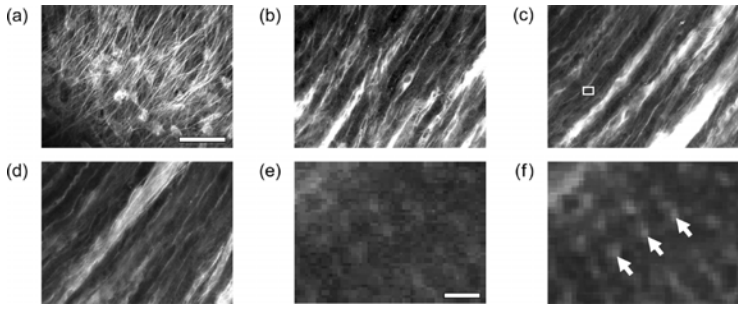

Fig. 5. Exemplary raw *XY* images from a three-dimensional stack of ventricular tissue. The images are from the (a) endocardial surface and a depth of (b) 10 μm, (c) 20 μm, and (d) 30 μm into the myocardium. (e) Zoomed view of region marked by white box in (c). (f) Processed image from region marked by white box in (c). White arrows indicate cross-sections of transverse tubules. Scale: 50 μm in (a) applies to (a)–(d), 2 μm in (e) applies also to (f).

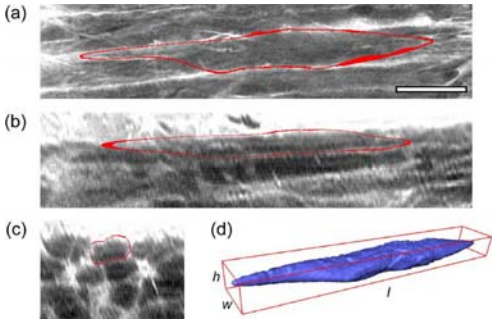

Fig. 6. Exemplary segmentation of a single cardiac myocyte in (a) XY, (b) XZ, and (c) YZ images of atrial tissue. (d) Three-dimensional model of myocyte created by manual segmentation and thresholding. Scale: 20 μm applies to (a)–(c).

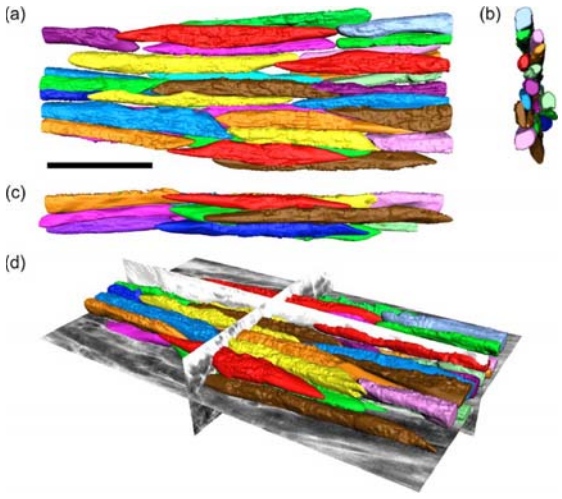

Fig. 7. Three-dimensional model of atrial tissue shown (a) from epicardial surface, (b) in fiber direction, and (c) from lateral side. (d) The model is shown overlaid with exemplary confocal images in three orthogonal planes. The model includes 17 complete and 21 partial myocytes. Scale: 50 μm applies to (a)–(c).

4.7% and 79.7 ± 2.9%, respectively (Table II). Myocyte density was 165 571 ± 55 836 and 86 957 ± 32 280 cells/mm^3 for atrial

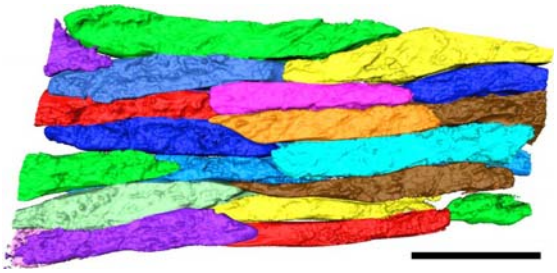

Fig. 8. Three-dimensional model of ventricular tissue shown from endocardial surface. The model includes 11 complete myocytes and 11 partial myocytes. Scale: 50 μm.

and ventricular tissue, respectively. Principal component analysis demonstrated that the long (first principal) axis of myocytes was parallel to the surface of atrial and ventricular tissue (Figs. 7 and 8) within 6° and 3° deviation to the surface plane, respectively. Furthermore, the majority of ventricular myocytes (70%) had their second principal axis approximately parallel ($<25°$) to the tissue surface. In contrast, atrial tissue did not show parallel orientation of the second principal axis with respect to the surface.

IV. Discussion and Conclusion

We described an approach for spatial modeling and analysis of living cardiac tissue based on three-dimensional image data obtained by scanning confocal microscopy. For that purpose, we developed a novel method for the local delivery of fluorescent dye and labeling of cardiac tissue, which we characterized with standard inverted and catheter-based confocal microscopy systems. We introduced a methodology to process stacks of microscopic images and applied it to obtain detailed spatial models and quantitative data on cardiac microstructure. These models and data promise to constitute important input for tissue characterization and computational modeling of cardiac function.

In studies with living cardiac tissue, we demonstrated that our novel hydrogel-based dye delivery method provided dye in sufficient concentration to yield high contrast images up to a depth of ~80 μm. We used dextran-conjugated, lysine-fixable Texas Red dye with a molecular weight of 3 kDa. This dye is

TABLE I
QUANTITATIVE VALUES ON RABBIT MYOCYTE GEOMETRY. VALUES ARE MEAN ± SD

	Tissue	Length (μm)	Width (μm)	Height (μm)	Volume (μm^3)	Area (μm^2)
This Study	Atrial (n=28)	105.0±10.6	13.1±1.7	9.7±1.6	4901±1713	46.0±13.3
	Vent. (n=20)	112.3±14.3	18.4±2.3	14.1±2.7	10,299±3598	91.0±26.3
Clemo and Baumgarten [36]	Atrial	140.8±8.0	11.9±0.7		20,500±2400	
Shaffer et al. [35]	Atrial	107.9±7.3	16.6±1.3		33,000±6800	
Duan et al. [37]	Atrial	123±13	9.5±0.4		9056±1514	
Hamrell et al. [38]	Vent.	107.4±6.8	16.0±1.9			
Satoh et al. [39]	Vent.	142.8±29.5	31.9±9.5	12.2±1.7	30,400±7300	

TABLE II
RABBIT MYOCYTE DENSITY. VALUES ARE MEAN ± SD

	Tissue	Myocyte Volume Fraction	Myocyte Density (cells/mm^3)
This Study	Atrial	72.4±4.7%	165,571±55,836
	Vent.	79.7±2.9%	86,957±32,280
Frank and Langer [12]	Vent.	75.4%	
Polimeni* [13]	Vent.	81.0%	

*Data from rat.

hydrophilic and penetrated the endo- and epicardium, but not intact cell membranes. We obtained similar results with other dextran-based dyes (data not shown), such as 10 kDa lysine-fixable Texas Red, and 3 and 10 kDa Alexa Fluor 488 (Molecular Probes, Eugene, OR). These findings are related to those of Andries and Brutsaert [28], who demonstrated that dextran-conjugated Lucifer Yellow with a molecular weight of 10 kDa diffused through the ventricular endothelium of rat hearts. Their study also demonstrated that a dye with a molecular weight of 40 kDa did not penetrate the endothelium.

Our studies revealed that the dye delivery method enables imaging of tissue sections at micrometer resolution immediately after contact of the tissue surface with the dye carrier. The applied dye resulted in high contrast between the intracellular and extracellular space; showing myocytes and the extracellular space as regions with low and high signal intensities, respectively [Fig. 4(b)–(d) and Fig. 5(b)–(d)]. In the endo- and epicardium, collagen fibers appeared bright in comparison to the surrounding space [Fig. 4(a) and Fig. 5(a)]. We suggest that the large signal intensity of collagen fibers is caused by binding of collagen to lysine residues of the dye [34]. In the interstitial space, larger strands of collagen fibers appeared to be parallel to myocytes [Fig. 4(b)–(d) and Fig. 5(b)–(d)].

We tested our method for dye delivery also with a catheter-based confocal imaging system (FCM1000, Leica, Wetzlar, Germany) applied to an isolated rabbit heart mounted and Langendorff-perfused. We demonstrated that the dye delivery method can be used in this type of preparation, and obtained two-dimensional images of atrial tissue [Fig. 3(b)]. The applied catheter-based system has a lower resolution than standard confocal imaging systems, and is not capable of acquiring three-dimensional stacks of images. These technical limitations of the current catheter-based systems are expected to be overcome in the near future and catheter-based high resolution, three-dimensional confocal imaging systems will provide data similar to standard systems [9], [11]. Thus, an important perspective of the described approach is related to established clinical catheterization techniques, which allow minimally invasive access to the heart of patients and are commonly used for electrophysiology and interventional cardiology. We suggest that a combination of the presented approach of dye delivery with catheter-based confocal microscopy and clinical catheterization techniques will allow for patient-specific modeling of cardiac tissue structure.

Using a standard confocal imaging system, the approach allowed us to spatially reconstruct and characterize myocyte arrangements in atrial and ventricular tissue. The reconstructions can serve as spatial domains for simulations of cardiac conduction using methods developed previously [21], [27]. Furthermore, we presented statistical data on myocyte geometry, volume fraction and density. These data can be used in mono- or bidomain models of cardiac conduction as described by Smaill *et al.* [7] and Hooks *et al.* [6], as well as for discrete multidomain models that use idealized geometry such as Roberts *et al.* [27].

Analysis of myocyte geometry yielded lengths, widths and heights similar to those reported in literature for rabbit cardiac tissue (Table I). The atrial myocyte length of 105.0 ± 10.6 μm was slightly lower than previously reported lengths between 107.9 and 140.8 μm [35], [36]. The atrial myocyte width is within the reported range [35]–[37]. Also, the ventricular length and width are within the reported range [38], [39]. Previously reported myocyte volumes are in general larger than our calculated volumes. Specifically, our average atrial myocyte volume of 4901 μm^3 is below the reported range of 9056 to 33 000 μm^3, and our average ventricular myocyte volume of 10 299 μm^3 is approximately one-third of the value reported in literature of 30 400 μm^3. This difference in volume can be explained by the method for approximating myocyte geometry. Our method is based on a geometrically accurate reconstruction, whereas others approximated myocytes to be brick- or

cylinder-shaped with cell height equal to cell width. Assuming brick- or cylinder-shaped myocytes and calculating myocyte volume based on our calculated length and width, our myocyte volume would increase approximately three-fold. Thus, these approximations and the lengths and widths determined in this study would give similar values to those reported in literature. Differences in myocyte geometry might also be related to our experimental approach. Most literature values of myocyte geometry were from isolated cells, which was suggested to be different in tissue [35]. Furthermore, most previous studies on myocyte geometry were based on analysis of two-dimensional image data, which do not allow for complete three-dimensional characterization.

Further analysis quantified myocyte volume fraction and myocyte density in atrial and ventricular tissue sections (Table II). These data are important parameters in modeling studies of electrical conduction in cardiac tissue [21]. The ventricular myocyte volume fraction of 79.7% is similar to the reported 75.4% for rabbit tissue [12] and 81.0% for rat tissue [13]. An underestimation of myocyte volume fraction can be expected with our experimental approach, because it applied tissue sections which were not arterially perfused (see Limitations). Myocyte volume fractions in rabbit atrial tissue have not been reported previously. Myocyte density was approximately double in atrial tissue compared to ventricular tissue ($165\,571 \pm 55\,836$ versus $86\,957 \pm 32\,280$ cells/mm^3). This is mainly caused by the smaller size of atrial myocytes (4901 μm^3 in atrial versus 10 299 μm^3 in ventricular). The volume fraction of ventricular myocytes was 10.1% larger than atrial myocytes. The overestimation of myocyte volumes in previous studies as well as the difference between atrial and ventricular myocyte volume fractions are noteworthy, in particular, with respect to improving computational modeling of cardiac electro-mechanics.

The approach enables quantification of myocyte geometry, volume fraction and density, which are known to be altered in aging cardiac tissue and cardiac diseases such as hypertrophy, atrophy, infarction and ischemia (see Section I). We suggest that the described approach can also be applied to create models and quantitative descriptions of microstructures in diseased tissue. In particular, the labeling of collagen that was demonstrated might allow spatial characterization of the extent of fibrosis. In aging atrial bundles, fibrosis is a common phenomenon and responsible for the side-to-side decoupling of atrial myocytes [21]. Furthermore, fibrosis is known to occur not only in infarcted regions of the heart but in surrounding regions as well [19]. Similarly, we expect that the approach can be used to model and quantify effects of ischemia and edema on cardiac microstructure.

Limitations: Several limitations of this study are related to optical properties of confocal imaging systems. Spatial resolution is arguably the most significant of these limitations for our application. The spatial resolution can be estimated from measured PSFs. In general, PSFs from confocal imaging systems are anisotropic, but transversally isotropic. Typically, the full width at half-maximum is 2–3 times larger in the direction of the laser beam compared to directions orthogonal to it [40]. Our measurement of PSFs for the BioRad MRC-1024 suggest that we can separate points having a distance of 1.85 and 0.30 μm in the laser beam direction and transvere to it, respectively, in the unprocessed data. With our manual approach this resolution proved to be sufficient for myocyte segmentation and characterization. However, reconstruction of small structures, such as the transverse tubular system, appear to be difficult. In previous studies, we used a 60x oil-immersion objective lens and shorter excitation/emission wavelengths for imaging of isolated living ventricular myocytes [31]. These imaging conditions caused a higher spatial resolution and enabled us to reconstruct the transverse tubular system. Similar conditions could be useful for imaging of tissue with submicrometer resolution. Further limitations are related to depth-dependent attenuation of signal intensity and our compensation approach; a mono-exponential description of attenuation. This model fits the signal from our tissue studies, but appears rather coarse with respect to the various causes of attenuation. In an attempt to estimate attenuation of our optical imaging system, we imaged regions of homogenous dye concentration and similar depth as in our tissue studies. Again, the signal fit our monoexponential model, but the analysis indicates that only one-third of attenuation in our tissue studies is caused by system properties. The analysis suggests that other causes contribute significantly to attenuation. A probable cause is dye diffusion from the carrier into the tissue, which can be expected to establish depth-dependent dye concentrations [41]. Furthermore, attenuation might differ in tissue and water. While these limitations did not inhibit our ability to obtain the presented models, improved signal quantification appears possible by more detailed modeling of attenuation, in particular separating dye diffusion-related attenuation from attenuation caused by system and media properties.

A limitation of our evaluation of the imaging approach is related to contractility of cardiac tissue. Motion caused by tissue contraction will introduce artifacts, especially for three-dimensional imaging. Similar difficulties from motion are common with other cardiac imaging techniques such as magnetic resonance imaging and computed tomography. Methods for triggered image acquisition and *a posteriori* selection of image data, commonly based on electrocardiography, have been developed in the past to attenuate this problem [42]. We suggest that similar methods will allow for reduction of motion artifacts in confocal imaging of tissue microstructure.

Further limitations include our experimental approach using isolated tissue sections. Tissue dissection causes damage to superficial cells. To circumvent this limitation we did not image near regions where cuts were made. Furthermore, our tissue sections were not arterially perfused, but instead submerged in solution. This lack of perfusion pressure on the tissue can cause reduction of the extracellular space and degrade tissue viability. Some image stacks exhibited myocyte-shaped regions of high signal intensity [Fig. 5(c), bottom right]. We suggest that these are cells with a compromised membrane allowing dye to penetrate into the intracellular space. Additionally, some of these image stacks with myocyte-shaped regions of high signal intensity exhibited motion artifacts. The motion appears to be caused by apoptosis related membrane damage, calcium influx and contracture of the affected cells. We rejected images with motion artifacts from further processing. Additionally, some of our image stacks exhibited low SNR, which resulted from difficulties in

moving the tissue surface in close proximity to the coverslip. These difficulties are caused by irregularity of the surfaces of the cardiac tissue samples. Overall, these limitations do not affect the application of our described method.

Other limitations are associated to our image processing approach. Automated approaches for myocyte segmentation in the described image data are currently not available. Our first step for segmentation of myocytes was based on manual deformation of triangular meshes. This manual process was accomplished with the user's discretion. Furthermore, threshold values to distinguish intra- from extracellular space were chosen from histograms of voxel intensity. A bimodal distribution of voxel intensity would facilitate the separation of the intra- from the extracellular space. However, intensity distribution was not bimodal, but showed a normal to right-skewed distribution. Although threshold values were ultimately based on mode and standard deviation for each segmented myocyte, the value used was based on qualitative evaluation of the spatially modeled myocytes.

Another limitation is related to the usage of other dyes with the described dye delivery approach. With this approach, the applied dye readily diffused from the hydrogel carrier through the endo- or epicardium into the myocardium. We did not test the delivery approach with other dyes (see exceptions above). We expect that hydrophobicity of fluorescent dyes and their Stokes' radius, which takes into account size and shape, will determine their applicability using our approach. Of particular interest are dyes for functional characterization of cardiac tissue. Labeling with voltage and calcium sensitive dyes are established approaches for characterizing cardiac wave conduction and excitation-contraction coupling, respectively.

ACKNOWLEDGMENT

The authors would like to thank Dr. E. Savio-Galimberti, Dr. J. Bridge, and Dr. P. Jones for useful discussions and their help in the presented studies.

REFERENCES

[1] R. Yuste, "Fluorescence microscopy today," *Nat. Methods*, vol. 2, pp. 902–904, 2005.

[2] N. C. Shaner, P. A. Steinbach, and R. Y. Tsien, "A guide to choosing fluorescent proteins," *Nat. Methods*, vol. 2, pp. 905–909, 2005.

[3] J. A. Conchello and J. W. Lichtman, "Optical sectioning microscopy," *Nat. Methods*, vol. 2, pp. 920–931, 2005.

[4] A. Diaspro, *Confocal and Two-Photon Microscopy: Foundations, Applications, and Advances*. New York: Wiley, 2002.

[5] M. S. Spach, J. F. Heidlage, P. C. Dolber, and R. C. Barr, "Extracellular discontinuities in cardiac muscle: Evidence for capillary effects on the action potential foot," *Circ. Res.*, vol. 83, pp. 1144–1164, 1998.

[6] D. A. Hooks, K. A. Tomlinson, S. G. Marsden, I. J. LeGrice, B. H. Smaill, A. J. Pullan, and P. J. Hunter, "Cardiac microstructure implications for electrical propagation and defibrillation in the heart," *Circ. Res.*, vol. 91, pp. 331–338, 2002.

[7] B. H. Smaill, I. J. LeGrice, D. A. Hooks, A. J. Pullan, B. J. Caldwell, and P. J. Hunter, "Cardiac structure and electrical activation: Models and measurement," *Clin. Exp. Pharmacol. Physiol.*, vol. 31, pp. 913–919, 2004.

[8] H. Inoue, S. Kudo, and A. Shiokawa, "Novel endoscopic imaging techniques toward in vivo observation of living cancer cells in the gastrointestinal tract," *Dig. Dis.*, vol. 22, pp. 334–337, 2004.

[9] S. Anandasabapathy, "Endoscopic imaging: Emerging optical techniques for the detection of colorectal neoplasia.," *Curr. Opin. Gastoroenterol.*, vol. 24, pp. 64–69, 2008.

[10] M. Goetz, A. Hoffman, P. R. Galle, M. F. Neurath, and R. Kiesslich, "Confocal laser endoscopy: New approach to the early diagnosis of tumors of the esophagus and stomach," *Future Oncol.*, vol. 2, pp. 469–476, 2006.

[11] R. Kiesslich and M. F. Neurath, "Endoscopic confocal imaging," *Clin. Gastroenterol. Hepato.*, vol. 3, pp. 58–60, 2005.

[12] J. S. Frank and G. A. Langer, "The myocardial interstitium: Its structure and its role in ionic exchange," *J. Cell Biol.*, vol. 60, pp. 586–601, 1974.

[13] P. I. Polimeni, "Extracellular space and ionic distribution in rat ventricle," *Am J. Physiol.*, vol. 227, pp. 676–683, 1974.

[14] J. A. Hill and E. N. Olson, "Cardiac plasticity," *N. Eng. J. Med.*, vol. 358, pp. 1370–1380, 2008.

[15] P. Ahuja, P. Sdek, and W. R. MacLellan, "Cardiac myocyte cell cycle control in development, disease, and regeneration," *Physiol. Rev.*, vol. 87, pp. 521–544, 2007.

[16] I. Banerjee, J. W. Fuseler, R. L. Price, T. K. Borg, and T. A. Baudino, "Determination of cell types and numbers during cardiac development in the neonatal and adult rat and mouse," *Am J. Physiol. Heart Circ. Physiol.*, vol. 293, pp. H1883–1891, 2007.

[17] H. W. Vliegen, A. Laarse, J. A. N. Huysman, E. C. Wijnvoord, M. Mentar, C. J. Cornelisse, and F. Eulderink, "Morphometric quantification of myocyte dimensions validated in normal growing rat hearts and applied to hypertrophic human hearts," *Cardiovasc. Res.*, vol. 21, pp. 352–357, 1987.

[18] S. E. Campbell, B. Korecky, and K. Rakusan, "Remodeling of myocyte dimensions in hypertrophic and atrophic rat hearts," *Circ. Res.*, vol. 68, pp. 984–996, 1991.

[19] B. Swynghedauw, "Molecular mechanisms of myocardial remodeling," *Physiol. Rev.*, vol. 79, pp. 215–262, 1999.

[20] W. E. Cascio, G. X. Yan, and A. G. Kleber, "Passive electrical properties, mechanical activity, and extracellular potassium in arterially perfused and ischemic rabbit ventricular muscle. Effects of calcium entry blockade or hypocalcemia," *Circ. Res.*, vol. 66, pp. 1461–1473, 1990.

[21] M. S. Spach, J. F. Heidlage, R. C. Barr, and P. C. Dolber, "Cell size and communication: Role in structural and electrical development and remodeling of the heart," *Heart Rhythm*, vol. 1, pp. 500–515, 2004.

[22] N. S. Peters, "New insights into myocardial arrhythmogenesis: Distribution of gap-junctional coupling in normal, ischaemic and hypertrophied human hearts," *Clin. Sci.*, vol. 90, pp. 447–452, 1996.

[23] R. Zeller, "Fixation, embedding, and sectioning of tissues, embryos, and single cells," in *Curr. Protoc. Mol. Biol.*, 2001.

[24] F. B. Sachse, *Computational Cardiology: Modeling of Anatomy, Electrophysiology, And Mechanics*. Heidelberg, Germany: Springer, 2004.

[25] A. J. Pullan, L. K. Cheng, and M. L. Buist, *Mathematically Modelling the Electrical Activity of the Heart: From Cell to Body Surface and Back Again*. Singapore: World Scientific, 2005.

[26] J. P. Keener and J. Sneyd, *Mathematical Physiology*. New York: Springer, 1998.

[27] S. F. Roberts, J. G. Stinstra, and C. S. Henriquez, "Effect of nonuniform interstitial space properties on impulse propagation: A discrete multidomain model," *Biophys. J.*, vol. 95, pp. 3724–3737, 2008.

[28] L. J. Andries and D. L. Brutsaert, "Endocardial endothelium in the rat: Junctional organization and permeability," *Cell Tissue Res.*, vol. 277, pp. 391–400, 1994.

[29] R. G. Thorne and C. Nicholson, "In vivo diffusion analysis with quantum dots and dextrans predicts the width of brain extracellular space," *Proc. Nat. Acad. Sci. USA*, vol. 103, pp. 5567–5572, 2006.

[30] E. Savio, J. I. Goldhaber, J. H. B. Bridge, and F. B. Sachse, "A framework for analyzing confocal images of transversal tubules in cardiomyocytes," in *Lecture Notes Computer Science*. New York: Springer, 2007, vol. 4466, pp. 110–119.

[31] E. Savio-Galimberti, J. Frank, M. Inoue, J. I. Goldhaber, M. B. Cannell, J. H. Bridge, and F. B. Sachse, "Novel features of the rabbit transverse tubular system revealed by quantitative analysis of three-dimensional reconstructions from confocal images," *Biophys. J.*, vol. 95, no. 4, pp. 2053–2062, 2008.

[32] R. C. Gonzalez and R. E. Woods, *Digital Image Processing*. Reading, MA: Addison-Wesley, 1992.

[33] O. Langendorff, "Untersuchungen am überlebenden Säugetierherzen," *Pflügers Arch.*, vol. 61, pp. 291–332, 1895.

[34] J. Greilberger, O. Schmut, and G. Jurgens, "In vitro interactions of oxidatively modified LDL with type I, II, III, IV, and V collagen, laminin, fibronectin, and poly-d-lysine," *Arterioscler. Thromb. Vasc. Biol.*, vol. 17, pp. 2721–2728, 1997.

[35] R. F. Shaffer, C. M. Baumgarten, and R. J. Damiano, "Prevention of cellular edema directly caused by hypothermic cardioplegia: Studies in isolated human and rabbit atrial myocytes," *J. Thorac. Cardiovasc. Surg.*, vol. 115, pp. 1189–1193, 1998.

[36] H. F. Clemo and C. M. Baumgarten, "cGMP and atrial natriuretic factor regulate cell volume of rabbit atrial myocytes," *Circ. Res.*, vol. 77, pp. 741–749, 1995.

[37] D. Duan, B. Fermini, and S. Nattel, "Alpha-adrenergic control of volume-regulated Cl-currents in rabbit atrial myocytes. Characterization of a novel ionic regulatory mechanism," *Circ. Res.*, vol. 77, pp. 379–393, 1995.

[38] B. B. Hamrell, E. T. Roberts, J. L. Carkin, and C. L. Delaney, "Myocyte morphology of free wall trabeculae in right ventricular pressure overload hypertrophy in rabbits," *J. Mol. Cell Cardiol.*, vol. 18, pp. 127–138, 1986.

[39] H. Satoh, L. M. Delbridge, L. A. Blatter, and D. M. Bers, "Surface: Volume relationship in cardiac myocytes studied with confocal microscopy and membrane capacitance measurements: Species-dependence and developmental effects," *Biophys J.*, vol. 70, pp. 1494–1504, 1996.

[40] S. Bolte and F. P. Cordelieres, "A guided tour into subcellular colocalization analysis in light microscopy," *J. Microsc.*, vol. 224, pp. 213–232, 2006.

[41] J. Crank, *The Mathematics of Diffusion*, 2nd ed. New York: Oxford Univ. Press, 1980.

[42] B. M. Ohnesorge, *Multislice CT in Cardiac Imaging: Technical Principles, Clinical Application and Future Developments*. New York: Springer, 2002.

CHAPTER 3

DESIGN AND CHARACTERIZATION OF A MODIFIED T-FLASK BIOREACTOR FOR CONTINUOUS MONITORING OF ENGINEERED TISSUE STIFFNESS

Reprinted with permission from *Biotechnol Prog*. 2010;26(3):857-64.

AIChE

Design and Characterization of a Modified T-Flask Bioreactor for Continuous Monitoring of Engineered Tissue Stiffness

Richard A. Lasher, Jeffrey C. Wolchok, Monir K. Parikh, James P. Kennedy, and Robert W. Hitchcock
Dept. of Bioengineering, University of Utah, Salt Lake City, UT 84112

DOI 10.1002/btpr.380
Published online January 29, 2010 in Wiley InterScience (www.interscience.wiley.com).

Controlling environmental conditions, such as mechanical stimuli, is critical for directing cells into functional tissue. This study reports on the development of a bioreactor capable of controlling the mechanical environment and continuously measuring force-displacement in engineered tissue. The bioreactor was built from off the shelf components, modified off the shelf components, and easily reproducible custom built parts to facilitate ease of setup, reproducibility and experimental flexibility. A T-flask was modified to allow for four tissue samples, mechanical actuation via a LabView controlled stepper motor and transduction of force from inside the T-flask to an external sensor. In vitro bench top testing with instrumentation springs and tissue culture experiments were performed to validate system performance. Force sensors were highly linear ($R^2 > 0.998$) and able to maintain force readings for extended periods of time. Tissue culture experiments involved cyclic loading of polyurethane scaffolds seeded with and without (control) human foreskin fibroblasts for 8 h/day for 14 days. After supplementation with TGF-β, tissue constructs showed an increase in stiffness between consecutive days and from the acellular controls. These experiments confirmed the ability of the bioreactor to distinguish experimental groups and monitor tissue stiffness during tissue development. © 2010 American Institute of Chemical Engineers *Biotechnol. Prog.*, 26: 857–864, 2010
Keywords: bioreactor, tissue engineering, tissue stiffness, fibroblast

Introduction

Tissue engineering requires appropriate starting materials, environmental cues, and temporal orchestration to produce a tissue product that is effective for its intended use and safe if used for transplantation. Environmental cues, such as chemical and mechanical stimuli, play an essential role in the growth and development of engineered cells and tissues. Mammalian cells and in particular cardiac cells are subjected to external and intracellular mechanical forces in vivo, which determine the fundamental function of cell migration, proliferation, differentiation, and therefore tissue properties.[1–4] Appropriate mechanical stimuli direct various cells to develop into structurally and functionally mature tissue both in vivo and in vitro. Applying inappropriate stimuli can alter the cell phenotype, tissue properties and produce unorganized, stiff, fibrotic tissue that is implicated in various types of end stage organ failure.[5] Therefore it is important to not only control but also monitor mechanical stimuli in certain types of engineered tissue. This article reports on the development of a bioreactor designed to control the mechanical environment for engineered tissue constructs while continuously measuring their mechanical properties as a function of time. This type of bioreactor can be used to study tissue engineering variables and pathways associated with the development of normal and pathogenic tissue.

Correspondence concerning this article should be addressed to R. W. Hitchcock at r.hitchcock@utah.edu.

In cardiac tissue engineering the electromechanical environment plays an important role in defining the cardiac phenotype. These environmental variables can be used to direct tissue development and alter both structure and function. Electrical stimulation in two-dimensional myoblast cell cultures has been found to increase the expression of the gap junction protein, connexin43 (Cx43), which is the predominant connexin isoform in ventricular tissue.[6] Connexins are a hallmark of the cardiac phenotype and responsible for coupling the cytoplasmic compartments of adjacent myocytes to allow the rapid propagation of electrical signaling. Varying mechanical cues such as substrate stiffness and possibly overstretching can lead to expression of gap junctions in myofibroblasts which electrically couple to cardiomyocytes leading to irregular current propagation.[5,7] Mechanical stretching has also been found to enhance cell proliferation and matrix organization of neonatal rat myocytes[8] and human heart cells.[9] Likewise, in three-dimensional (3D) cell cultures, electrical stimulation was shown to induce myocyte alignment and increase electrical coupling via Cx43 upregulation,[10] while mechanical stimulation was shown to increase the contractile force of engineered tissue constructs.[3] These studies demonstrate the importance of environmental conditions on directing the growth and development of cells towards useful tissue.

To understand the effects of external stimuli, researchers in the field of cardiac tissue engineering have developed unique and elegant tools for developing and studying engineered cardiac tissue.[4,11–13] A variety of bioreactor systems have been developed to directly control environmental cues

while overcoming limitations inherent in static culture platforms. Spinner-flask bioreactors overcome the mass-transfer limitations of static culture environments and have shown improved cell seeding and development of cardiac tissue constructs.[14] Similarly, rotating wall vessels are capable of producing low levels of shear stress while improving mass-transfer rates, and have demonstrated the ability to create elongated myocytes and spontaneously contracting cardiac tissue constructs.[14] Direct perfusion systems have overcome limitations of poor cell infiltration and nonuniform cell coverage in 3D tissue constructs and have been shown to enhance cell survival, growth, and function in many engineered tissue types.[15,16]

Bioreactors capable of applying mechanical stimulation to 3D cardiac tissue to direct myocyte development have been developed.[12,17] Moreover, a bioreactor capable of applying both mechanical and electrical stimulation to cardiomyocytes and measuring their mechanical properties has been developed.[1] Although these tools meet their intended function, they are typically developed to meet the needs of a single laboratory and targeted towards a specific series of experiments. Therefore, there is a need to develop a more robust bioreactor capable of handling experimental flexibility, reproducibility, and economy. Although these goals are still on the horizon, we believe that the use of common cell culture equipment, open source designs and integrated sensing will enable life science labs without device fabrication capabilities to utilize these tools in tissue engineering, drug discovery, and basic science research. In addition, these types of designs can motivate future generations of bioreactors and take advantage of plate and fluid handling equipment that is routinely used for high throughput assays.

In this study, a next generation bioreactor capable of continuously measuring mechanical properties of cultured tissue was developed based on a previous design.[18] The previous bioreactor was designed specifically for engineering vocal fold tissue from primary human laryngeal fibroblasts. The bioreactor was capable of applying mechanical stimulation via a stepper motor controlled with LabView. To continuously monitor mechanical properties of cultured tissue, the bioreactor was significantly modified to incorporate force sensors for real time monitoring of force-displacement. This characterization of mechanical properties during tissue development provides nondestructive, real time feedback that can be used to control culture variables and assess experimental endpoints. Furthermore, the bioreactor was designed such that future modifications specific towards cardiac tissue engineering, such as perfusion and electrical stimulation, could be easily implemented without redesigning the system.

The central goal of this study was to develop a bioreactor capable of controlling the mechanical environment and continuously measuring force-displacement in engineered tissue. In addition, we specified that the bioreactor be built from off the shelf components, was easy to setup, reproducible, and flexible in its experimental capabilities. To accomplish this goal, we designed the bioreactor to meet these needs and performed in vitro bench top and tissue culture experiments to validate its performance.

Materials and Methods

Bioreactor design

A cell culture flask (T-75, Corning, Lowell, MA) was modified using a custom built fixture and CNC machine (MAXNC 15, Gilbert, AZ) to allow easy access to four tissue samples, linear actuation, and a magnetically coupled diaphragm assembly to measure applied forces. The top and force sensing sides of the flask were modified using a 0.32 cm diameter end mill at a motor speed of 1000 rpm and feed rate of 10.2 cm/min. The linear actuation side was modified using a 0.48 cm diameter end mill at a motor speed of 1000 and feed rates ranging from 1.3 to 10.2 cm/min. To secure the T-flask to the bioreactor base, extruded acrylic strips (Ridout Plastics, San Diego, CA) were mounted to the bottom (0.64 cm x 1.3 cm x 6.1 cm) and sides (0.64 cm x 1.3 cm x 2.6 cm) using UV curable adhesive (Loctite 3201). To maintain sterility during tissue culture, the modified culture flask was sealed on the three modified sides. A replaceable, self adhesive, clear polyester lid (mylar, Fralock, Valencia, CA) was designed to cover the flask's top opening and allow access to tissue. The linear actuation port holes are equal to the diameter of the stainless steel access rods, and the force sensing surface has elastomeric polyurethane diaphragms (described later).

Linear actuation was accomplished using a two phase bipolar stepping motor (PK244-04A, Oriental Motor, Torrance, CA), microstep motor drive (G201, Geckodrive, Tustin, CA), linear slide (NSK, Clarinda, IA), and belt-pulley system (SDP/SI, New Hyde Park, NY). Tissue forces were measured using four full bridge strain gauge force sensors (SMD, Wallingford, CT) secured in custom built aluminum housings with overload stops. Each load sensor is a double cantilever, stainless steel beam with a silicon nitride passivation layer and laser lithographed thin film nichrome sensing layer. The sensor is configured as a full Wheatstone bridge with four leads attached for providing excitation and signal voltages. The sensor is rated at 100 gf with a symmetric bridge resistance of 10 kΩ. Miniature neodymium magnets were used to magnetically couple each sensor to the tissue sample across flexible 0.05 mm polyurethane diaphragms (Converters, Huntingdon Valley, PA) attached to the side of the T-flask. The elastomeric diaphragms allow force from within the culture environment to be translated to an external transducer. This novel feature allows for noninvasive and nondestructive characterization of mechanical properties during tissue development. The stepper motor was controlled using a custom LabView program (version 8.2) and a multifunction data acquisition (DAQ) card (PCI-6221, National Instruments, Austin, TX).

Bioreactor characterization and testing

Before bioreactor assembly, force sensors were characterized for sensitivity, DC offset, and linearity. Forces ranging from 0 to 100 gf were applied in increments of 20 gf. Sensors were powered with 10 V excitation (as in the all the following tests) using a DC power supply (E3648A, Agilent Technologies, Santa Clara, CA). Output voltages were recorded using a data acquisition unit (34970A, Agilent Technologies, Santa Clara, CA).

Once sensors were characterized, the bioreactor was assembled and system verification was performed using instrumentation springs to mimic tissue constructs (~3 gf/mm, McMaster-Carr, Atlanta, GA). The stiffness of the instrumentation springs (~3 gf/mm) was similar to that of the elastomeric polyurethane scaffolds used in this study. The bioreactor was placed in an incubator at 37°C and sensor drift, linearity and repeatability were tested using

LabView controlled motion patterns for 62 h. Displacements of 2, 4, 6, 8, and 10 mm were held for 2 h each in both ascending and descending motion paths. This displacement profile was repeated three times over the 62 h test period. Force was measured every minute over the duration of the study. The average of each force plateau was calculated and linear regression was performed on the ascending and descending sides. Furthermore, the intra- and inter-plateau range was calculated to yield a maximum variation for each plateau.

The ability of the sensors to record force at multiple displacements and speeds was assessed in a two stage experiment. First, speeds of 1, 2, 4, 8, and 16 mm/s (0.25, 0.50, 1, 2, and 4 Hz, respectively) were used to cyclically displace springs to 2 mm (4% strain). In the second experiment, springs were cyclically displaced to 1, 2, 5, and 10 mm (2%, 4%, 10%, and 20% strain) at a fixed speed of 2 mm/s. Force readings at minimum and maximum displacements were used to calculate spring constants.

Forces were recorded at a sampling rate of 1,000 Hz on the DAQ and analyzed using MATLAB (Mathworks, Natick, MA). Recordings were baseline corrected and filtered with a 10- to 20-point moving average. Sensor noise levels were also determined in the postrecording processing by calculating the standard deviation of a constant force reading.

Scaffold fabrication and characterization

Porous polyurethane scaffolds were selected for preliminary tissue culture experiments to validate the bioreactor's capability of distinguishing experimental groups. The polyurethane scaffolds have elastomeric properties, allowing them to be mechanically stretched during tissue culture.[19] To fabricate the porous polyurethane scaffolds, we adapted a previously described method from Titze et al.[18] Polyurethane pellets (Tecoflex SG-8, Lubrizol, Wickliffe, OH) were mixed with the solvent dimethylacetamide (DMAC) at a concentration of 0.4 g/mL and dissolved overnight at 60°C. Poloxamer (33% v/v) (Pluronic 10R5, BASF, Ludwigshafen, Germany) was added and the solution thoroughly mixed. The polymer solution was cooled to 46°C and poured into polymer molds. Polymer filled molds were further cooled for 2.5 min through surface contact with a dry-ice/ethanol bath and precipitated overnight in a room temperature DI water bath. Precipitated scaffolds were separated from the molds, rinsed in DI water for 48 hours, frozen to −80°C, and lyophilized. Lyophilized scaffolds were sectioned into strips (30 mm x 10 mm x 2 mm) and attached to 0.30 mm thick polyester (mylar, Fralock, Valencia, CA) mounts using medical grade UV curable adhesive (MD 1180, Dymax, Torrington, CT). Mounted scaffolds were ethylene oxide sterilized, soaked for 20 min in 70% ethanol to promote wetting, rinsed in DI water, and incubated at 37°C for 2 h in a fibronectin solution (20 μg/mL in PBS) (Invitrogen, Carlsbad, CA) to promote cell attachment.

Mechanical properties of the scaffolds were characterized using an Instron 3342 (Instron, Norwood, MA) at a gauge length of 20 mm ($n = 5$). The samples were tested to failure at a strain rate of 2 mm/s. The elastic modulus was calculated by plotting stress (force divided by cross-sectional area) and strain data. Scaffold porosity was calculated by the ratio of the void space to total volume of the scaffold ($n = 10$).[20] Total volume was calculated by multiplying the length, width, and height of rectangular samples. The mass of the samples were multiplied by the specific gravity of Tecoflex SG-8 (1.04 g/cm^3) to determine the volume of polyurethane material. The total volume minus the volume of polyurethane determined the volume of void space. Porosity was the ratio of void space to total volume.

Tissue culture experiment

Human foreskin fibroblasts (HFFs, ATCC, Manassas, VA) were selected because they are primary cells capable of secreting human ECM.[21] Deposition of ECM proteins is known to influence mechanical properties of the tissue construct during culture.[22] One of the bioreactor design goals was to characterize these mechanical property changes with our built in force sensor. Cells were passaged no more than three times before seeding. In preparation for scaffold seeding, frozen HFFs were thawed, plated onto T-175 flasks, and grown to confluency in DMEM/F12 (Gibco) with 10% FBS (Gibco) and 25 μg/mL gentamicin (Sigma). Confluent cultures were disassociated with 0.25% trypsin and 1 mM EDTA, centrifuged, and resuspended in DMEM/F12. Cells were counted with a hemocytometer using the trypan blue exclusion method and seeded onto scaffolds at a density of 2 million cells/scaffold.

Tissue constructs were placed in the bioreactor and pretensioned to 3 gf. The tissue constructs were cultured for 14 days and subjected to 10% strain (2 mm displacement) for 8 h a day followed by 16 h of rest. The strain profile consisted of an active phase of 2 sec and a resting phase of 2 sec. The active phase consisted of straining the construct at a speed of 2 mm/s and returning to 0% strain for 2 sec. Samples were maintained in a growth medium consisting of DMEM F12 supplemented with 10% FBS, gentamicin, and 1 mM ascorbic acid. Beginning on day 8 the growth medium was supplemented with recombinant human transforming growth factor beta 1 (rhTGF-β1, Peprotech, Rocky Hill, NJ) at a concentration of 4 ng/mL. Nonseeded scaffolds were maintained as controls. Stiffness of tissue samples ($n = 4$) and acellular controls ($n = 4$) were measured daily during the 14 days of culture. Stiffness was defined as force divided by displacement, which is analogous to a spring constant and reported as grams of force per millimeter of displacement. Stiffness values for each construct were normalized to day 1 and averaged to obtain a mean and standard deviation of the percent change in stiffness. Media was changed every 2–3 days. Instrumentation springs were placed in the bioreactor before and after the 14-day culture period and the spring constants were measured to verify sensor response.

Histological analysis

At day 14, samples from each tissue construct were stained with fluorescein diacetate (FDA) and propidium iodide (PI) to characterize cell viability according to the manufacturer's guidelines (Invitrogen, Carlsbad, CA). Following FDA-PI staining, samples were washed with PBS and fixed with 4% paraformaldehyde for 20 min. Triton X-100 was used to permeabilize the cell membrane and cells were trilabeled for α-smooth muscle actin, F-actin, and nuclei. Cells were stained for α-smooth muscle actin using an IgG2a conjugated anti-actin α-SMA primary antibody (Sigma-Aldrich, St. Louis, MO) as previously described.[23] Alexa Fluor 594 goat anti-mouse IgG (H+L) was used as a fluorescing secondary antibody (Invitrogen, Carlsbad, CA).

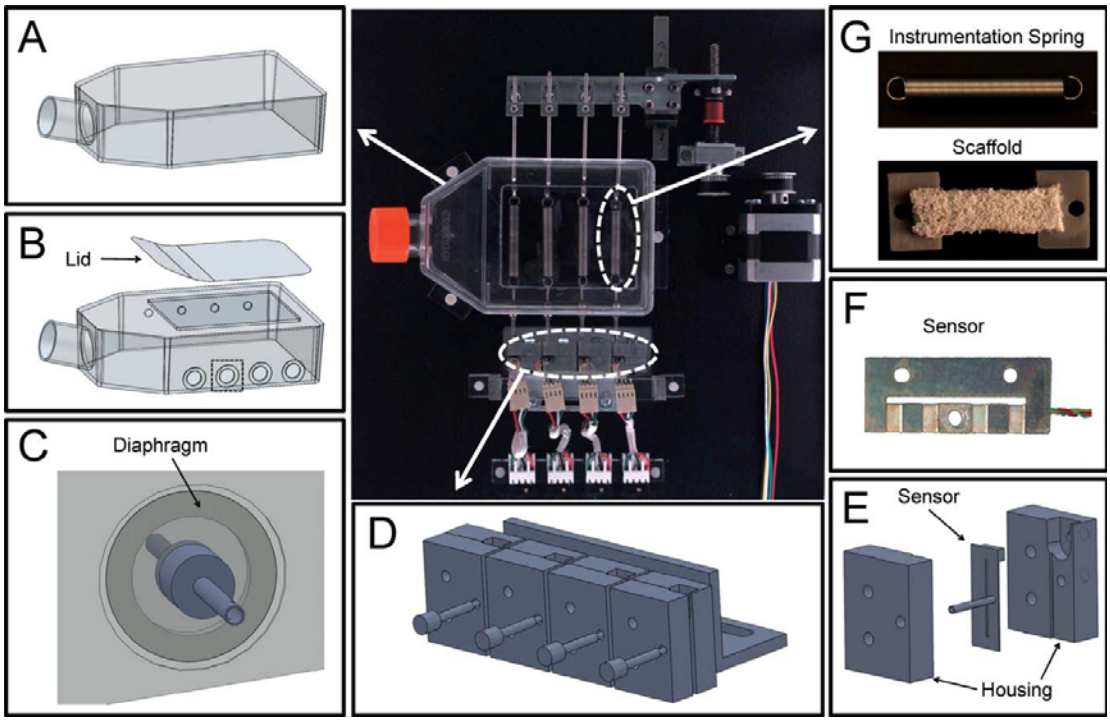

Figure 1. Assembled bioreactor (center photograph) with zoomed regions.

(A) Unmodified culture flask. (B) Exploded view of modified culture flask showing polyester lid (top) and side ports for linear actuation (back) and force transduction (front). (C) Zoomed view of magnet-diaphragm assembly shown by dashed box in panel B. Force is transferred across diaphragm through magnets. (D) Sensor overload housings. (E) Exploded view of sensor sandwiched between overload housing. (F) Full bridge strain gauge force sensor. (G) Spring (top) for system verification testing and tissue scaffold (bottom) attached to polyester mounts for tissue culture experiments.

F-actin was stained with phalloidin conjugated to Alexa Fluor 488 (Invitrogen, Carlsbad, CA). DAPI was used as a counterstain to visualize cell nuclei. Images were acquired using an FV1000 confocal microscope using a 40x objective and a field of view of 1024 x 1024 pixels (Olympus, Center Valley, PA).

Statistical analysis

ANOVA and post-hoc *t*-tests were performed to determine statistical significance with an $\alpha = 0.05$.

Results

Bioreactor assembly

The bioreactor was assembled with a combination of off the shelf components, modified off the shelf components, and easily reproducible custom built parts (Figure 1). The programmable CNC machine allowed for rapid, accurate, and repeatable modification of the T-75 flask (Figures 1A,B). The machined aluminum sensor housing prevented overload and provided a rigid structure to secure the sensor (Figures 1D,E). Flexible polyurethane diaphragms (Figure 1C) were used to mechanically couple the force sensors (Figure 1F) to the tissue constructs (Figure 1G).

Bioreactor characterization

All four sensors exhibited high linearity with $R^2 > 0.998$ (Figure 2A). Sensor sensitivity ranged from 7.79×10^{-3} to 9.87×10^{-3} mV/V/gf with DC offsets ranging from 0.0599 to 0.183 mV/V. Sensors exhibited approximately ± 0.31 gf of noise in the raw signals and was reduced to approximately ± 0.08 gf in the filtered signals.

Sensors maintained linearity ($R^2 > 0.999$) after bioreactor assembly and spring attachment. Furthermore, sensors maintained force readings over extended periods of time and returned to the same force for a given displacement (Figure 2B). The maximum range of force values recorded within a specified displacement (i.e. intra-plateau variation) was 0.22 gf. The maximum range of force values recorded between a specified displacement (i.e. interplateau variation) was 0.58 gf.

Sensors A, B, and C showed significantly different measured spring constants with varying speeds at a fixed displacement (ANOVA, $p < 0.05$ for all sensors) (Figure 3A). However, sensor D showed no statistically significant difference between measured spring constants in the same experimental conditions (ANOVA, $p > 0.078$ for all sensors). Post-hoc *t*-tests showed many speed groups being different from one another. All sensors displayed a statistically significant difference in spring constants for varying displacements at a fixed speed (ANOVA, $p < 0.05$ for all sensors) (Figure 3B). Post-hoc *t*-tests showed many displacements being different from one another. Although there were statistically significant differences between the measured spring constants, the standard deviation was less than 0.10 gf/mm for all sensors. Moreover, the maximum range for measured spring constants was 0.21 gf/mm ($\approx$8% of measured spring constant) for a fixed displacement and varying speeds, and

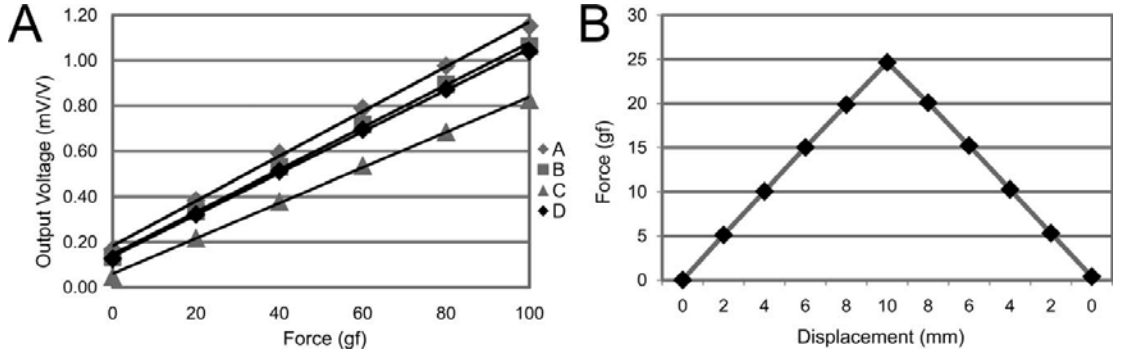

Figure 2. (A) Sensor characterization for four sensors A, B, C, and D.

Output voltage was normalized to constant input voltage. (B) Drift and repeatability of sensor A in assembled bioreactor showing first 22 hours of 62 h experiment (note: error bars smaller than data points).

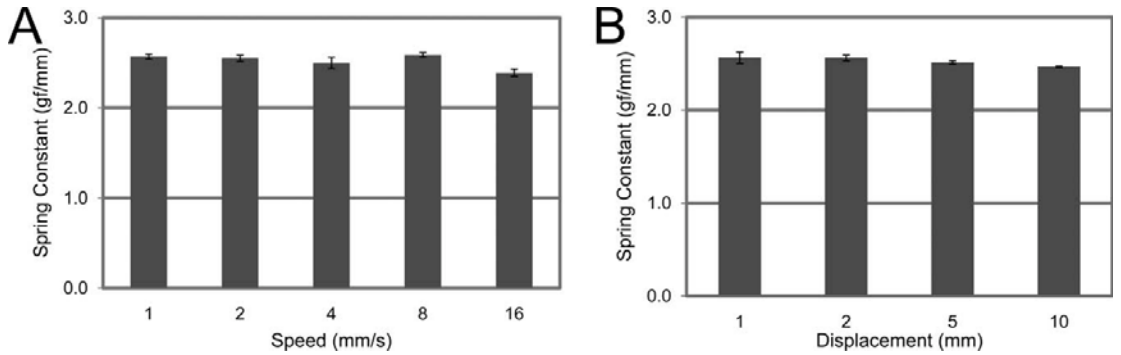

Figure 3. (A) Measured spring constants for sensor A with varying speeds of 1, 2, 4, 8, and 16 mm/s at a cyclic displacement of 2 mm (error bars denote standard deviation); (B) measured spring constants for sensor A with cyclic displacements of 1, 2, 5, and 10 mm at a fixed speed of 2 mm/s (error bars denote standard deviation).

0.16 gf/mm (≈6% of measured spring constant) for a fixed speed and varying displacements.

Scaffold characterization

The elastic modulus of the scaffold was 38.9 ± 8.9 kPa, calculated from the linear range of the stress–strain curve, which corresponded to 0–40% for all samples. The scaffolds were highly elastic, displaying a strain to failure at 301.0 ± 51.4% with an ultimate stress of 88.6 ± 23.5 kPa. Scaffolds porosity was 95.3 ± 0.8 %.

Tissue culture

Tissue constructs showed an increase in tissue stiffness over the 14 day culture duration (Figure 4). Following supplementation with TGF-β on day 8, statistically significant differences between consecutive days were observed ($p < 0.05$). Furthermore, the tissue constructs were statistically different from the acellular control ($p < 0.05$) on days 10 to 14. The porous polyurethane scaffolds (Figure 5A) showed excellent coverage by the fibroblasts (Figure 5B). Live/Dead imaging resulted in 100% observable cell viability with no dead cells or necrotic zones at the end of cell culture (Figure 5B). Fibroblasts stained positive for α-smooth muscle actin and filamentous actin (F-actin) (Figure 5C). To ensure sensor sensitivity was preserved during tissue culture, spring constants were measured before and after the experiments. Measured spring constants before and after the 14-day culture period were within 4%.

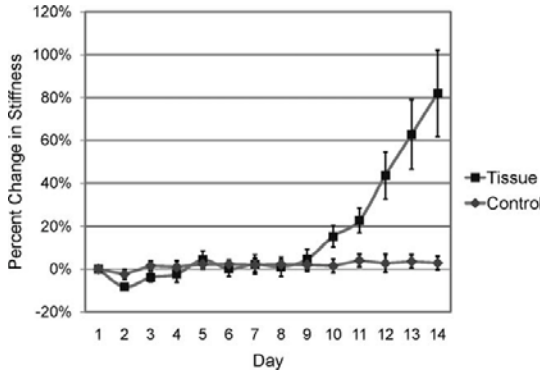

Figure 4. Percent change in stiffness of tissue constructs normalized to day 1.

Error bars denote standard deviation. TGF-β added on day 8.

Discussion

Controlling environmental conditions, such as the chemical and mechanical stimuli, is important in guiding cells into

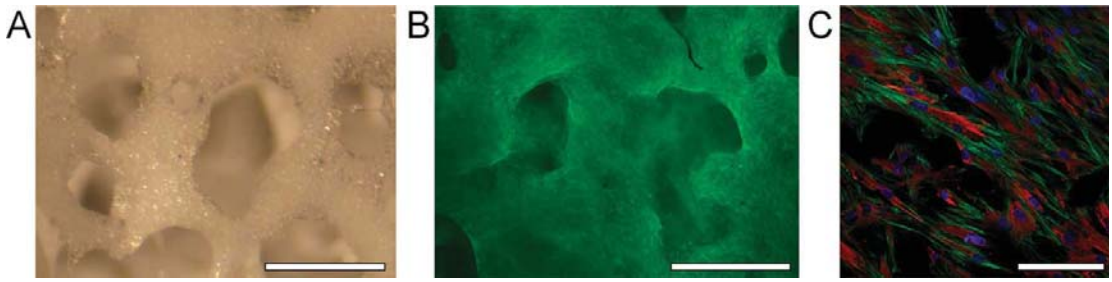

Figure 5. Scaffold before (A) and after (B,C) after 14 days of culture.

(A) Scaffold before cell seeding. (B) Live/Dead staining viable cells green and nonviable cells red. (C) Immunofluorescence staining of α-SMA (red) counterstained with phalloidin (green) and DAPI (blue). Scale 400 μm (A, B) and 100 μm (C).

functional tissue.[1–4] In this study, a bioreactor capable of controlling the mechanical environment and interrogating mechanical properties of engineered tissue was developed and verified through bench top testing and tissue culture experiments. The bioreactor is an open source tool and access to the assembly drawings, bill of materials, machined part drawings, LabView programs, and G-codes for the CNC machine are available by contacting the corresponding author.

A novelty of our bioreactor is the magnet-diaphragm assembly used to translate force from within the culture environment to an external transducer. This novel feature allows for nondestructive characterization of mechanical properties during tissue development, which is important in high throughput monitoring techniques needed in pharmaceutical testing.[24,25] Furthermore, the force of contraction is an important parameter for assessing the functional properties of engineered cardiac tissue.[1,3] Using magnets coupled across a thin polyurethane diaphragm reduces the moment applied to the transducer. Computer modeling and bench testing (data not shown) support the performance of the diaphragm/magnet coupling assembly in maintaining sensitivity and linearity when transmitting forces out of the culture chamber to an externally located force sensor. Other methods for mechanical coupling that include moving parts and seals were considered, but excluded due to inherent nonlinearity and hysteresis, which leads to inaccuracy and lack of precision.

The sensors were highly linear before and maintained linearity after bioreactor assembly (Figure 2). The drift and repeatability test demonstrated that the sensors were able to maintain force readings for extended periods of time and return to the same force reading for a given displacement. The maximum range of force values for intra- and inter-plateau was 0.22 and 0.58 gf, respectively. Furthermore, the measured spring constants at varying speeds and displacements were within a range of approximately 8% and 6% of the average spring constant, respectively (Figure 3). To address this limitation, lower speeds (2 mm/s), which increased spring constant reproducibility to within 2.9% were used to measure tissue stiffness during tissue culture. In this study, tissue constructs were stretched 2 mm, which resulted in a maximum force reading of approximately 8 gf. Therefore, only approximately 8% of the full range (100 gf full range) of the sensor was utilized during tissue culture. Using only 8% of the total range of the sensor leads to measurement inaccuracies, which is one limitation of the current study, however, the bioreactor was designed such that the sensor can be easily replaced to incorporate sensors with desired ranges.

The polyurethane scaffolds were highly elastic and allowed for seeding, proliferation, and mechanical conditioning of cells during the tissue culture experiments. Previous studies using the same material demonstrated that polyurethane scaffolds can be fabricated with tunable mechanical properties.[26] The ability to tune the mechanical properties and create thicknesses ranging from 50–5000 μm provides a tissue engineering scaffold material that can be used for both bench top and implant applications. Although this material is nondegradable, it can serve as a sacrificial template for a biosynthetic scaffold material. In this application, cells are seeded and secrete a continuous extracellular matrix consisting primarily of fibrillar collagen. The cultured construct can then be processed with fixatives, detergents, and an organic solvent, leaving a material that is similar in form to the original template but containing only secreted ECM products.[22]

The tissue culture experiment with fibroblasts demonstrated the ability of the bioreactor to control the mechanical environment and measure mechanical properties of the tissue during development. Furthermore, the bioreactor was able to measure differences between the acellular control and tissue constructs seeded with fibroblasts, demonstrating the utility of the bioreactor in distinguishing experimental groups.

Fibroblasts stained positive for α-smooth muscle actin and F-actin (Figure 5C). Previous studies have demonstrated that mechanical tension can promote fibroblasts to differentiate into proto-myofibroblasts, and the addition of TGF-β with mechanical tension can promote proto-myofibroblasts to differentiate into myofibroblasts.[5] Myofibroblasts play an important role in connective tissue remodeling and wound healing due to their specialized contractile ability, which includes the organization of α-smooth muscle actin into stress fibers.[23] In our tissue culture experiments, α-smooth muscle actin did not appear to organize into distinct stress fibers and was not co-localized with phalloidin suggesting that the α-smooth muscle actin was not in F-actin form.[27] However, TGF-β is known to enhance extracellular matrix formation by fibroblasts,[28] suggesting that our increase in stiffness was due to increased ECM production, however this was not evaluated in this study. In addition, the baseline force of the constructs did not change (data not shown) over the 14-day culture period which further suggests the stiffness

increase was due to ECM production rather than intracellular contractile mechanisms.

One limitation of the current bioreactor for cardiac tissue engineering is the lack of electrical stimulation and perfusion. Other studies have demonstrated the importance of the electromechanical environment in cardiac myocytes.[6,10] Future directions will include incorporating electrical stimulation to mimic environmental conditions for native cardiac tissue. Another limitation is the bioreactor's size and more specifically the culture density. The 3D tissue samples are capable of culturing several times more cells than a confluent monolayer in a similar culture vessel, however, each T-75 flask contains four tissue constructs that are each grown in the same culture and stimulation environment. Although different substrates and additional samples can be used in the same bioreactor, each reactor provides a similar environment. Intrareactor sample variables that can be adjusted in future designs include electrical stimulation and perfusion. The reactor has a modest footprint of 30.5 cm x 30.5 cm x 5.4 cm, which allows the placement of eight reactors in a standard sized incubator. We foresee that the current design requirements including 3D culture, mechanical strain, and tissue mechanical property interrogation can be scaled down to increase culture density and sample size.

In summary, we report here the development of a next generation bioreactor assembled from off the shelf and easily reproducible components that includes real time interrogation of cultured tissue mechanical properties using a magnetically coupled force transducer. The reactor has been characterized for sensor drift, linearity, and repeatability as well as system level measurement changes in response to strain rate. Although the measured spring forces change in response to strain rate, these changes can be used to both design the experiment and develop strategies that decrease strain rates during measurement cycles. Our 14-day test verified system stability and reliability as well as the ability to routinely measure engineered tissue mechanical properties using a completely automated system. The design and testing of this system provides insight into future designs that can increase sample size and culture density while providing a current design that can be used for studies related to the replacement of diseased/injured myocardium as well as pharmaceutics, genomics, and physiology research.

Acknowledgments

We gratefully acknowledge the advice of Patrick Tresco, Ph.D. and the use of the Keck Center for Tissue Engineering resources in assisting with the in vitro portion of this project. Funding for this work was provided through the Department of Bioengineering start-up support for R. Hitchcock.

Literature Cited

1. Feng Z, Matsumoto T, Nomura Y, Nakamura T. An electro-tensile bioreactor for 3-D culturing of cardiomyocytes. *IEEE Eng Med Biol Mag*. 2005;24:73–79.
2. Raimondi T. Engineered tissue as a model to study cell and tissue function from a biophysical perspective. *Curr Drug Discov Technol*. 2006;3:245–268.
3. Fink C, Ergun S, Kralisch D, Remmers UTE, Weil J, Eschenhagen T. Chronic stretch of engineered heart tissue induces hypertrophy and functional improvement. *FASEB J*. 2000;14:669–679.
4. Bursac N. Cardiac tissue engineering using stem cells. *IEEE Eng Med Biol Mag*. 2009;28:80–89.
5. Tomasek JJ, Gabbiani G, Hinz B, Chaponnier C, Brown RA. Myofibroblasts and mechano-regulation of connective tissue remodelling. *Nat Rev Mol Cell Biol*. 2002;3:349–363.
6. Kawahara Y, Yamaoka K, Iwata M, Fujimura M, Kajiume T, Magaki T, Takeda M, Ide T, Kataoka K, Asashima M. Novel electrical stimulation sets the cultured myoblast contractile function to 'on'. *Pathobiology*. 2006;73:288–294.
7. Zlochiver S, Munoz V, Vikstrom KL, Taffet SM, Berenfeld O, Jalife J. Electrotonic myofibroblast-to-myocyte coupling increases propensity to reentrant arrhythmias in two-dimensional cardiac monolayers. *Biophys J*. 2008;95:4469–4480.
8. Zhuang J, Yamada KA, Saffitz JE, Kleber AG. Pulsatile stretch remodels cell-to-cell communication in cultured myocytes. *Circ Res*. 2000;87:316–322.
9. Akhyari P, Fedak PWM, Weisel RD, Lee TYJ, Verma S, Mickle DAG, Li RK. Mechanical stretch regimen enhances the formation of bioengineered autologous cardiac muscle grafts. *Circulation*. 2002;106:137–142.
10. Radisic M, Park H, Shing H, Consi T, Schoen FJ, Langer R, Freed LE, Vunjak-Novakovic G. Functional assembly of engineered myocardium by electrical stimulation of cardiac myocytes cultured on scaffolds. *Proc Natl Acad Sci USA*. 2004;101:18129–18134.
11. Radisic M, Park H, Gerecht S, Cannizzaro C, Langer R, Vunjak-Novakovic G. Biomimetic approach to cardiac tissue engineering. *Philos Trans R Soc Lond B Biol Sci*. 2007;362:1357–1368.
12. Zimmermann WH, Schneiderbanger K, Schubert P, Didie M, Munzel F, Heubach JF, Kostin S, Neuhuber WL, Eschenhagen T. Tissue engineering of a differentiated cardiac muscle construct. *Circ Res*. 2002;90:223–230.
13. Freed LE, Guilak F, Guo XE, Gray ML, Tranquillo R, Holmes JW, Radisic M, Sefton MV, Kaplan D, Vunjak-Novakovic G. Advanced tools for tissue engineering: scaffolds, bioreactors, and signaling. *Tissue Eng*. 2006;12:3285–3305.
14. Carrier RL, Papadaki M, Rupnick M, Schoen FJ, Bursac N, Langer R, Freed LE, Vunjak-Novakovic G. Cardiac tissue engineering: cell seeding, cultivation parameters, and tissue construct characterization. *Biotechnol Bioeng*. 1999;64:580–589.
15. Martin I, Wendt D, Heberer M. The role of bioreactors in tissue engineering. *Trends Biotechnol*. 2004;22:80–86.
16. Chen HC, Hu YC. Bioreactors for tissue engineering. *Biotechnol Lett*. 2006;28:1415–1423.
17. Birla RK, Huang YC, Dennis RG. Development of a novel bioreactor for the mechanical loading of tissue-engineered heart muscle. *Tissue Eng*. 2007;13:2239–2248.
18. Titze IR, Hitchcock RW, Broadhead K, Webb K, Li W, Gray SD, Tresco PA. Design and validation of a bioreactor for engineering vocal fold tissues under combined tensile and vibrational stresses. *J Biomech*. 2004;37:1521–1529.
19. Mulder MM, Hitchcock RW, Tresco PA. Skeletal myogenesis on elastomeric substrates: Implications for tissue engineering. *J Biomater Sci Polym Ed*. 1998;9:731–748.
20. Papenburg BJ, Vogelaar L, Bolhuis-Versteeg LAM, Lammertink RGH, Stamatialis D, Wessling M. One-step fabrication of porous micropatterned scaffolds to control cell behavior. *Biomaterials*. 2007;28:1998–2009.
21. Karamichos D, Brown RA, Mudera V. Collagen stiffness regulates cellular contraction and matrix remodeling gene expression. *J Biomed Mater Res A*. 2007;83:887–894.
22. Wolchok JC, Brokopp C, Underwood CJ, Tresco PA. The effect of bioreactor induced vibrational stimulation on extracellular matrix production from human derived fibroblasts. *Biomaterials*. 2009;30:327–335.
23. Hinz B, Celetta G, Tomasek JJ, Gabbiani G, Chaponnier C. Alpha-smooth muscle actin expression upregulates fibroblast contractile activity. *Mol Biol Cell*. 2001;12:2730–2741.
24. Allen DD, Caviedes R, Cárdenas AM, Shimahara T, Segura-Aguilar J, Caviedes PA. Cell lines as in vitro models for drug screening and toxicity studies. *Drug Dev Ind Pharm*. 2005;31:757–768.

25. Donato MT, Lahoz A, Castell JV, Gomez-Lechon MJ. Cell lines: a tool for in vitro drug metabolism studies. *Curr Drug Metab*. 2008;9:1–11.
26. Kennedy JP, McCandless SP, Lasher RA, Hitchcock RW. The mechanically enhanced phase separation of sprayed polyurethane scaffolds and their effect on the alignment of fibroblasts. *Biomaterials*. 2010;31:1126–1132.
27. Langevin HM, Storch KN, Cipolla MJ, White SL, Buttolph TR, Taatjes DJ. Fibroblast spreading induced by connective tissue stretch involves intracellular redistribution of alpha- and beta-actin. *Histochem Cell Biol*. 2006;125:487–495.
28. Lawrence DA. Transforming growth factor-beta: a general review. *Eur Cytokine Netw*. 1996;7:363–374.

Manuscript received Aug 19, 2009, and revision received Nov. 30, 2009.

CHAPTER 4

MICROSTRUCTURAL COMPARISON OF ENGINEERED AND NATIVE CARDIAC TISSUE BASED ON THREE-DIMENSIONAL CONFOCAL MICROSCOPY

4.1 Abstract

Quantifying and establishing structural features of native myocardium in engineered tissue is essential for creating functional tissue that can serve as a surrogate for *in-vitro* testing or the eventual replacement of diseased or injured myocardium. Here, we applied three-dimensional confocal imaging and image analysis to quantitatively describe features of native and engineered cardiac tissue, focusing on myocyte geometry and spatial distribution of the major gap junction protein connexin-43 (Cx43). Quantitative analysis methods were developed and applied to test the hypothesis that environmental cues direct engineered tissue towards a phenotype resembling that of age-matched native myocardium. The analytical approach was applied to engineered cardiac tissue with and without the application of electrical stimulation as well as to age-matched and adult native tissue. Individual myocytes were segmented from confocal image stacks and assigned a coordinate system from which measures of cell geometry and Cx43 spatial distribution were calculated. Data were collected from 9 nonstimulated and 12 electrically stimulated engineered tissue constructs and 5 postnatal day 12 (P12) and 7

adult hearts. The myocyte volume fraction was nearly double in stimulated engineered tissue compared to nonstimulated (0.34±0.14 vs. 0.18±0.06, $p<0.01$), but less than half of native P12 (0.90±0.06) and adult (0.91±0.04) myocardium. Myocytes under electrical stimulation were more elongated compared to nonstimulated myocytes, and exhibited similar lengths, widths and heights as in age-matched myocardium. Furthermore, the percentage of membrane positive for Cx43 was similar in the electrically stimulated, P12 and adult myocytes, whereas it was significantly lower in nonstimulated myocytes. Cx43 was found to be primarily located at cell ends for adult myocytes and irregularly but densely clustered over the membranes of nonstimulated, stimulated and P12 myocytes. These findings support our hypothesis and reveal that the application of environmental cues produce tissue with structural features more representative of age-matched native myocardium than adult myocardium. We suggest that the presented approach can be applied to quantitatively characterize developmental processes and mechanisms in engineered tissue.

4.2 Introduction

Establishing hallmarks of the native myocardium in engineered tissue is essential for creating functional tissue that can serve as a surrogate for *in-vitro* testing or the eventual replacement of diseased or injured myocardium [1]. Quantitative measures of structural and functional tissue characteristics form a technical cornerstone for the development and testing of engineered cardiac tissue. Native tissue is complex and exhibits a three-dimensional (3D) multicellular structure and function. This 3D microenvironment has profound effects on the properties, behavior and functions of

resident cells [1-3]. Furthermore, native tissue exhibits astonishing variation in the quantity, density, and morphology of cardiac cells during development, amongst species, between tissue types and in disease [4-6]. Most engineered cardiac tissue aims to replicate left ventricular myocardium, which is heterogeneous and comprised of densely packed myocytes, fibroblasts and other cell types.

Fibroblasts account for the majority of cells in the heart and play important roles in normal cardiac function and disease [7, 8]. Although myocytes only account for 20-40% of cells that make up cardiac tissue, they occupy approximately 80-90% of the tissue volume and are the contractile cells solely responsible for pump function [9, 10]. Alterations in myocyte geometry and structure are known to occur during development and in disease states [11-13]. Myocyte structures that are critical for cardiac function include sarcomeres and gap junctions. Sarcomeres, the fundamental unit of contraction, occupy a large fraction of the intracellular volume and are highly aligned in healthy myocytes. Gap junctions allow for rapid electrical signaling between myocytes necessary for synchronous cardiac contraction. Connexin-43 (Cx43), the predominant isoform of gap junction channels in ventricular myocytes [14, 15], has a half-life of 2 hours. The continuous turnover allows Cx43 to redistribute along the cell surface in response to environmental conditions [16, 17]. The distribution of Cx43 is known to vary during development and in disease states [18, 19]. For example, in rat cardiac tissue, Cx43 redistributes in response to tissue maturity. In neonatal tissue Cx43 clusters are found to be distributed over the myocyte membrane. As the tissue matures, Cx43 slowly becomes organized and at approximately 90 days after birth concentrates at the cell ends (i.e. polarized) [18]. Gap junctions also remodel due to disease. For example, as human

cardiac hypertrophy progresses into heart failure Cx43 expression decreases and accumulates at the lateral sides of myocytes instead of the ends (i.e. lateralized) [4, 14, 20]. Gap junctions can be coerced to rearrange *in-vitro*. A recent study in 2D monolayers of neonatal rat myocytes indicated polarization of Cx43 localization by stretching [21]. The functional importance and dynamic nature of Cx43 makes it a target for analysis, and these types of responses may indicate some level of control over engineered cardiac tissue.

Several approaches have been developed to produce 3D engineered cardiac tissue including seeding preformed scaffold materials with cells [22], entrapping cells in a 3D environment [23], stacking cell sheets [24], and decellularizing and recellularizing tissue [25] (Reviewed in detail in refs [26, 27]). The application of electrical stimulation [22, 28, 29], mechanical stimulation [30-32], or perfusion [33] has been shown to aid in the tissue development. To investigate the structure of these engineered tissues most reported methods rely on qualitative interpretation of 2D images. A more comprehensive analysis of structure can be accomplished through 3D confocal microscopy [34, 35]. Confocal microscopy is based on fluorescent labeling and has the ability to control the depth of field (slice resolution of <1 μm), reject out-of-focus light and collect sequential optical sections from thick specimens [36, 37]. The application of 3D confocal imaging to quantitatively characterize structure has not been widely performed on engineered tissue.

The hypothesis of this study is that the application of environmental cues directs engineered tissue towards a phenotype resembling that of age-matched native myocardium. The hypothesis was tested by applying 3D confocal imaging and image analysis to characterize hallmarks of cardiac tissue, including myocyte geometry and

spatial distribution of Cx43, in engineered cardiac tissue with and without the application of electrical stimulation. The results of the study support our hypothesis and reveal that the application of environmental cues produce tissue with structural features resembling age-matched native myocardium as opposed to adult tissue.

4.3 Methods

4.3.1 Cell Isolation

All animal procedures were performed in accordance with an approved protocol by the University of Utah Institutional Animal Use and Care Committee. Ventricular cardiac cells were harvested from 1-day old Sprague-Dawley rats (Charles River, MA) using a protocol and supplies from Worthington Biochemical (Lakewood, NJ). Briefly, hearts were aseptically removed and collected in calcium-and magnesium-free Hank's balanced salt solution. Atria were removed and the ventricles were finely minced and digested in 50 µg/mL trypsin at 4°C overnight. Further digestion was performed the following day with collagenase (1500 units) in Leibovitz L-15 media. Cell suspensions were triturated, filtered, centrifuged and resuspended in culture medium. Culture medium was made following Hansen *et al.* [38] using DMEM F12 (Thermo Fisher Scientific, Waltham, MA), 10% equine serum (Thermo Fisher Scientific, Waltham, MA), 2% chick embryo extract (Gemini Bioproducts, West Sacramento, CA), 50 µg/mL human insulin (Sigma-Aldrich, St. Louis, MO), 2 mM L-glutamine (Thermo Fisher Scientific, Waltham, MA), 20 U/mL penicillin (MP Biomedicals, Solon, OH), 50 µg/mL streptomycin (MP Biomedicals, Solon, OH), 63 µg/mL tranexamic acid (Sigma-Aldrich, St. Louis, MO) and 33 µg/mL aprotinin (Sigma-Aldrich, St. Louis, MO).

4.3.2 Sample Preparation and Culture

Fibrin-based engineered tissue samples were fabricated using methods described by Hansen *et al.* [38]. Briefly, a reconstitution mixture was prepared on ice comprising of 4.1 x 10^6 cells/mL, 5 mg/mL bovine fibrinogen (Sigma-Aldrich, St. Louis, MO), and 100 µL/mL Matrigel (BD Biosciences, San Jose, CA). For each sample, 485 µL of reconstitution mixture was mixed with 15 µL thrombin (100 U/mL, Sigma-Aldrich, St. Louis, MO) and transferred to a custom mold (Fig. 4.1). The custom mold was contained in a Petri-dish and consisted of a Delrin® (McMaster-Carr, Los Angeles, CA) housing and base each containing two neodymium magnets (Applied Magnets, Plano, TX), which allowed for easy coupling and uncoupling of the mold and base. The housing had a center channel 4.8 mm in width and 20 mm in length with 6.35 mm holes centered with the silicone posts and contained cylinder-shaped (1.6 mm diameter × 6.4 mm length) magnets. The base was 34 × 20 mm and contained disc-shaped (4.8 mm diameter × 1.6 mm thick) magnets that aligned with the housing. Rectangular frames (34 × 12 mm) were cut from 0.30 mm thick polyester sheets (Mylar®, Fralock, Valencia, CA) using a cutting plotter (Graphtech FC7000, Irvine, CA) and AutoCAD (San Rafael, CA), and sandwiched between the housing and base. Frames had a rectangular center (10 × 4.8 mm) and two 4 mm through holes spaced 26 mm apart (center-to-center). Silicone rods (2 mm diameter x 7 mm length) were fabricated from a platinum cured silicone elastomer (VST-50, Factor II, Lakeside, AZ) and attached to either side of the frame window (spaced 12 mm center-to-center). The silicone posts served to suspend the fibrin-based gel (Fig. 4.1D). Samples were allowed to polymerize at 37°C for 90 min. After 30 min of polymerization, 500 µL of culture medium were added to keep the sample hydrated and

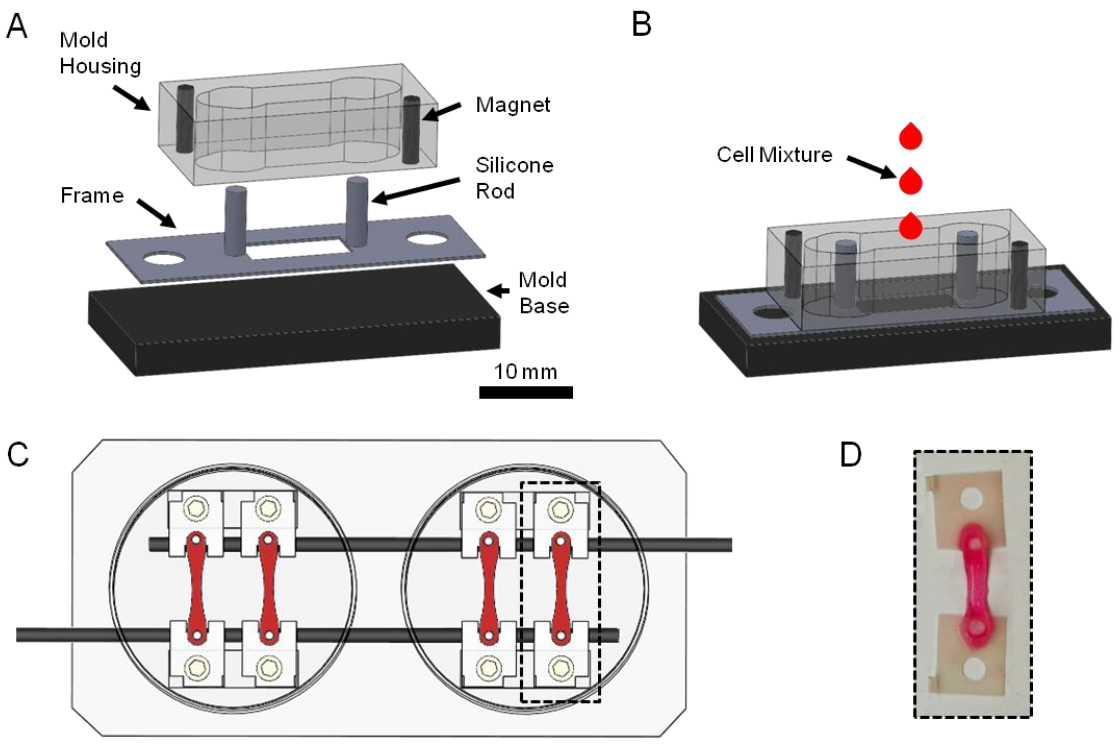

Figure 4.1 – Sample preparation and bioreactor. (A) Exploded and (B) assembled view of mold for producing tissue samples. (C) Bioreactor comprised of two Petri-dishes and carbon rods for electrical stimulation. (D) Tissue sample.

aid in removal of the mold from the tissue sample. The frame was cut on both sides and the sample was elongated by 40% and secured with nylon screws into a custom bioreactor comprised of two Petri-dishes outfitted with carbon rods spaced 2 cm apart for electrical stimulation (Fig. 4.1C) [39].

Engineered tissue samples were precultured for 3 days before onset of electrical stimulation [22]. Following preculture, samples were subjected to electrical field stimulation (2 ms symmetric biphasic square pulses, 4 V/cm, 1 Hz) for 9 days. Nonstimulated samples served as controls for stimulated samples. Bright field images of central regions of the engineered tissue samples were obtained at days 3, 6, 9 and 12 of culture. The diameter was measured and the cross-sectional area was estimated assuming a cylindrical cross-section. The percent decrease in sample size was calculated normalized to the start of stimulation, i.e., day 3 of culture. At the end of culture samples were fixed with 4% paraformaldehyde and stored in PBS at 4°C.

4.3.3 ET and MCR

The excitation threshold (ET) and maximum capture rate (MCR) were measured at days 6, 9 and 12 of culture and for postnatal day 3 (P3) rat hearts following methods described previously [29, 33]. ET was defined as the minimum voltage required to elicit synchronous contractions over the entire sample and MCR as the maximum frequency for synchronous contractions at 150% of the ET. For engineered tissue samples, measurements were made following 30 min of media exchange. For P3 hearts, rats (n=4) were anesthetized with isofluorane inhalation. Following thoracotomy hearts were quickly excised and placed in a modified oxygenated Tyrode's solution (in mM: 126

NaCl, 11 Dextrose, 0.1 $CaCl_2$, 13.2 KCl, 1 $MgCl_2$, 12.9 NaOH, 24 HEPES) at room temperature. Strips of left ventricular myocardium (≈2 × 2 × 4 mm) were excised and placed in the same bioreactors used for tissue culture. For all samples, ET was measured by applying square 2 ms monophasic pulses starting at 0 V/cm and incrementally increasing until the sample was observed to beat synchronously. MCR was measured by setting the voltage to 150% of the ET and increasing the frequency until the contractions became asynchronous, irregular or ceased.

4.3.4 Native Tissue Preparation and Sectioning

P12 and adult rat hearts were used for comparison to the engineered tissue samples. Tissue was processed as previously described [35]. Briefly, rats were anesthetized through methoxyflurane and hearts quickly removed. Hearts were perfused with a zero calcium Tyrode's solution for 5 min followed by 2% paraformaldehyde for 15 min for fixation using the retrograde Langendorff method [40]. Whole hearts and engineered tissue samples were stored in 30% sucrose in preparation for sectioning. For adult hearts, biopsies were obtained with a 5 mm diameter biopsy punch through the left ventricular wall. P12 hearts were maintained as whole hearts. Biopsied adult hearts, whole P12 hearts and engineered tissue samples were frozen in tissue freezing medium (Triangle Biomedical Sciences, Durham, NC) and sectioned using a cryostat (Leica CM1950, Wetzlar, Germany). Adult heart biopsies were sectioned parallel to the epicardial surface and P12 hearts from the top of the ventricles to approximately 2 mm from the apex to produce 80-100 μm thick sections. Longitudinal and transverse cross-sections with a thickness of 100 μm were produced for engineered tissue samples.

4.3.5 Fluorescent Labeling

Fluorescent labeling was performed before sectioning for engineered tissue and after sectioning for native tissue samples. Tissue samples were labeled as described previously [35]. Samples were either quad-labeled with wheat germ agglutinin (WGA) to identify cell borders, for α-sarcomeric actinin to identify myocytes, for Cx43 to identify gap junction channels and with 4',6-Diamidino-2-phenylindole dihydrochloride (DAPI) to identify nuclei, or tri-labeled for α-sarcomeric actinin to identify myocytes, for vimentin to identify nonmyocytes (mostly fibroblasts) and with DAPI to identify nuclei.

All labeling was performed on a laboratory platform rocker at room temperature (Thermo Fisher Scientific, Waltham, MA). Antibodies were diluted in blocking solution consisting of 4% goat serum (Invitrogen, Carlsbad, CA) and 0.5% Triton X-100 (Fisher Scientific, Pittsburgh, PA) diluted in PBS. Rinsing was performed between all incubation steps and included three 15 min rinses. For quad-labeling samples were incubated for 16 h with WGA-conjugated CF488 (20-40 µg/mL in PBS, 29022, Biotium, Hayward, CA), 16 h with mouse IgG_1 anti-α-sarcomeric actinin (1:100, ab9465, Abcam, Cambridge, MA) followed by 6 h with goat anti-mouse IgG_1-conjugated Alexa Fluor 633 (1:200, A21126, Invitrogen, Carlsbad, CA), 1 h with Image-iT® FX signal enhancer (Alexa Fluor 555 Goat Anti-Rabbit SFX Kit, A31630, Invitrogen, Carlsbad, CA) to block nonspecific antibody binding, 16 h with rabbit anti-GJA1 (1:100, SAB4300504, Sigma-Aldrich, St. Louis, MO) followed by 6 h with goat anti-rabbit IgG-conjugated Alexa Fluor 555 (1:200, A31630, Invitrogen, Carlsbad, CA), and 3 h with 4',6-Diamidino-2-phenylindole dihydrochloride (DAPI) (1:500, Sigma-Aldrich, St. Louis, MO). For tri-labeling samples were incubated for 16 h with mouse IgG_1 anti-α-sarcomeric actinin

(1:100, ab9465, Abcam, Cambridge, MA) followed by 6 h with goat anti-mouse IgG_1-conjugated Alexa Fluor 633 (1:200, A21126, Invitrogen, Carlsbad, CA), 16 h with mouse monoclonal anti-vimentin-conjugated Cy3 (1:50, C9080, Sigma-Aldrich, St. Louis, MO) and 3 h with DAPI (1:500, Sigma-Aldrich, St. Louis, MO). Tissue samples were stored in PBS.

4.3.6 Confocal Imaging

Three-dimensional image stacks were acquired for samples labeled with WGA, α-sarcomeric actinin, Cx43 and DAPI on a Zeiss LSM 5 Duo confocal microscope (Carl Zeiss, Jena, Germany) using a 40x oil-immersion objective lens with a numerical aperture of 1.3 [35]. Sectioned tissue samples were placed on a glass slide and surrounded by 15-30 µL of Fluoromount-G™ Slide Mounting Medium (Electron Microscopy Sciences, Hatfield, PA). The tissue sample was covered with a coverslip (#0) and placed on the imaging stage. The x-axis of the image stack was aligned with the long-axis of the myocytes by visual inspection and adjustment of the scan direction. For engineered tissue samples, sections were briefly scanned using a 10x objective lens to locate dense regions of myocytes. Only regions with high cell density were imaged in this study.

Image stacks were acquired with a spatial resolution of 200 × 200 × 200 nm and a typical field of view of 1024 × 768 × 200 voxels using a multitrack protocol for quasi-simultaneous imaging of fluorophores in each 2D image slice. Laser lines with a wavelength of 364, 488, 543 and 633 nm were alternately applied to excite their associated fluorophores and collected using long pass 385 nm, band pass 505-555 nm, long pass 560 nm and band pass 630-650 nm filters, respectively. The dwell time was

typically 1.3-1.5 μs/pixel resulting in a total imaging time of approximately 1 h per image stack. Signal-to-noise ratio (SNR) of each image stack was measured as described previously [35]. Image stacks with a SNR below 3 were rejected. For whole sample examination of engineered tissue, 2D images were acquired using a 10x objective of central transverse and longitudinal tissue sections stained with α-sarcomeric actinin, vimentin and DAPI. Higher magnification (40x) 2D images were also acquired for engineered and native tissue samples stained with α-sarcomeric actinin, vimentin and DAPI.

4.3.7 Image Processing

Image stacks were processed to improve image quality as previously described [34, 35]. Briefly, image stacks were processed to remove background, correct for depth-dependent attenuation and deconvolved using the iterative Richardson-Lucy algorithm with measured point spread functions. Cross-reactivity was corrected in image protocols where a primary antibody reacted with two secondary antibodies. The cross-reactivity was characterized by colocalization of Cy3 and α-sarcomeric actinin associated signal and removed by subtraction of Cy3-associated intensities. Individual myocytes were segmented using a manual deformable triangle mesh fitted in three image planes (XY, XZ and YZ) using the WGA, α-sarcomeric actinin, Cx43 and DAPI image data [34, 35, 41]. The manual segmentation was refined using the WGA image data. Principal component analysis was performed for each segmented myocyte to yield eigenvectors e_1, e_2 and e_3. A bounding box was created for each segmented myocyte using the coordinate system spanned by the eigenvectors. Length, width and height were determined from the

dimensions of the bounding box. Myocyte volume was defined as the volume of voxels within the segmented myocyte and surface area was estimated from the surface area of the triangle mesh.

4.3.8 Cx43 Analysis

The percentage of the membrane stained positive with Cx43 was calculated for each segmented myocyte using projections of Cx43 intensities onto the myocyte surface. An illustration of this method is shown in Fig. 4.2. The membrane was approximated by surface voxels around the perimeter of the segmented myocyte. A 3D distance map was calculated from both the inside and outside of the membrane. Gradient vectors were calculated from the distance map. Cx43 intensities within 1 μm of the membrane were projected onto the membrane using the calculated distance map and vectors. The percentage of the membrane positive for Cx43 ($Mem_{Cx43Pos}$) was calculated for each myocyte:

$$Mem_{Cx43Pos} = \frac{nv_{Mem,Cx43>0}}{nv_{Mem}}$$

with the number of membrane voxels (nv_{Mem}) and the number of membrane voxels with nonzero Cx43 intensity ($nv_{Mem,Cx43>0}$).

The spatial distribution of Cx43 was characterized through projections of Cx43 intensities on the eigenvectors of the myocyte [35]. Profiles were normalized with respect to total intensities and the range of arguments was transformed to [-1, 1] (i.e., centered with respect to the respective bounding box dimension). For each eigenvector, polarization ($Pol_{25\%}$) was characterized through summation of Cx43 intensities from 25%

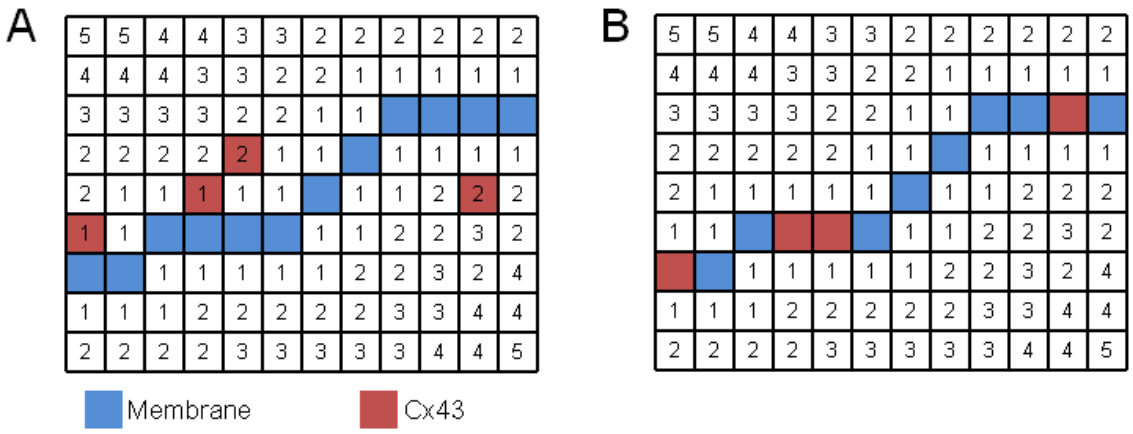

Figure 4.2 – Simplified schematic for calculating percentage of membrane positive for Cx43. Voxels are represented on a grid with blue indicating membrane and red indicating Cx43 staining. The integer values represent distance in voxels from the membrane. Gradient vectors were calculated from the distance map and Cx43 intensities were mapped to the membrane as shown in B.

of either end of the myocyte. The minimal polarization ($Pol_{25\%min}$), maximum polarization ($Pol_{25\%max}$), and the sum of $Pol_{25\%min}$ and $Pol_{25\%max}$ ($Pol_{25\%total}$) were reported. Uniform Cx43 distributions for a profile would lead to $Pol_{25\%total}$ of 50%. Higher order statistical moments, skewness (γ_1) and kurtosis (γ_2), were calculated for the Cx43 intensity profiles. Skewness and kurtosis are measures of asymmetry and peakedness, respectively. A skewness of zero indicates that intensities are evenly distributed on both sides of the mean, whereas positive and negative values of skewness indicate that intensities are concentrated in the negative ($x<0$) and positive ($x>0$) domain, respectively. The kurtosis of a normal or uniform distribution is 0 and -1.2, respectively.

4.3.9 Myocyte Volume Fraction

The myocyte volume fraction (MVF) was calculated by down-sampling the processed 3D image data for the α-sarcomeric actinin labeling. Original voxels with dimensions of 0.2 × 0.2 × 0.2 μm were resampled to 1.6 × 1.6 × 1.6 μm using the maximum value in a 26-voxel neighborhood relation [42]. This effectively "blurred" the sarcomeres and filled gaps between adjacent z-discs. Histograms of voxel intensities associated with actinin-positive regions were generated and thresholds were defined as mode intensity minus one standard deviation. Voxels above the threshold were considered actinin positive. MVF was defined as the sum of actinin positive voxels divided by the sum of all voxels within the image stack.

4.3.10 Statistical Analysis

Data were reported as mean±standard deviations. Statistical significance was determined with a one-way ANOVA for each measure, followed by post-hoc Tukey-Kramer tests with an $\alpha=0.05$. Where appropriate, F-tests were performed to determine differences in variances with an $\alpha=0.05$.

4.4 Results

4.4.1 Visual Inspection of Engineered Tissue Preparations

Bright field images of the engineered tissue samples showed that samples progressively condensed during culture (Fig. 4.3). Engineered tissue sample cross-sectional area estimated from the measured diameter was found to decrease to 17±3% and 16±5% for nonstimulated and stimulated samples at the end of culture from the onset of stimulation. No significant differences in cross-sectional area were observed between the nonstimulated and stimulated samples. Central transverse and longitudinal cross-sections of whole tissue samples exhibited dense regions of aligned myocytes and fibroblasts (Fig. 4.4). Although nuclei appeared to be homogeneously distributed through the sample thickness, elongated myocytes were located approximately 200 μm from the sample periphery. Higher magnification confocal images showed that fibroblasts were in close spatial proximity to myocytes, however, P12 and adult native tissue samples exhibited a higher density of fibroblasts and myocytes (Fig. 4.5).

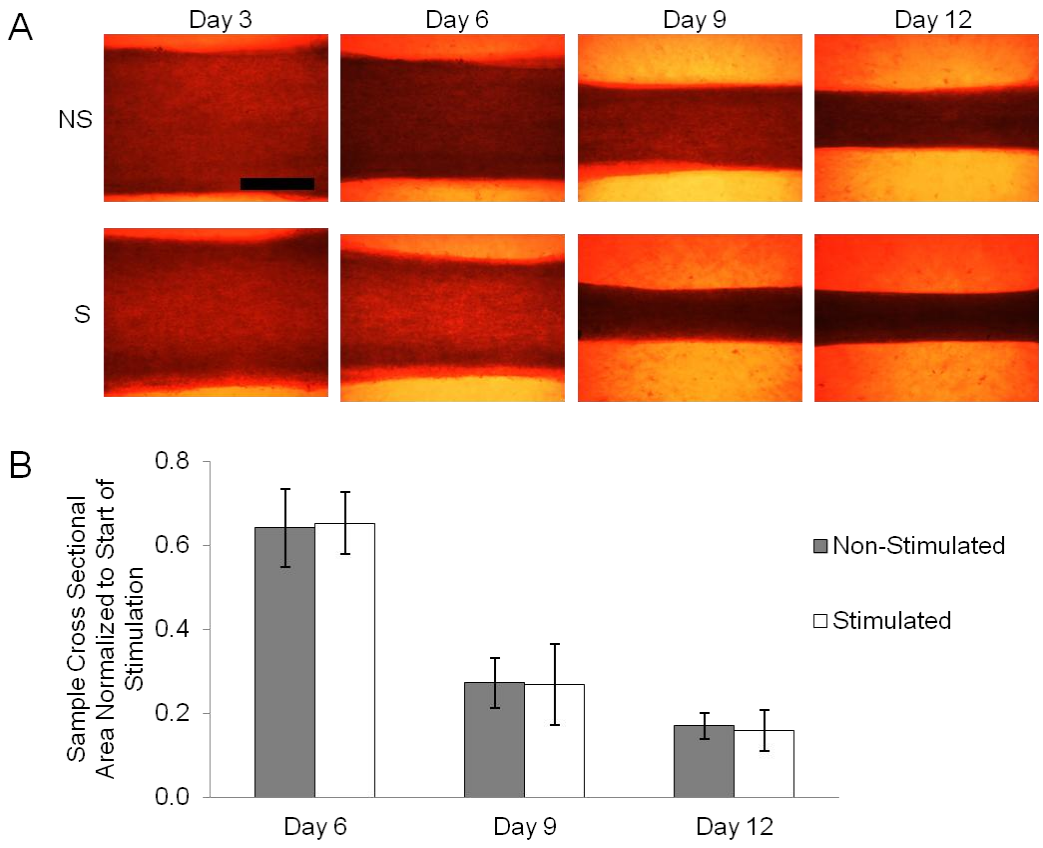

Figure 4.3 – Engineered tissue size. (A) Images showing progression of engineered cardiac tissue size during culture (nonstimulated (n=9) and stimulated (n=12)). Scale bar 1 mm. (B) Cross sectional area normalized to start of electrical stimulation (Day 3). Error bars denote standard deviation. Engineered cardiac tissue progressively decreases in volume as a function of time in culture; however, there is no statistically significant difference between nonstimulated and stimulated.

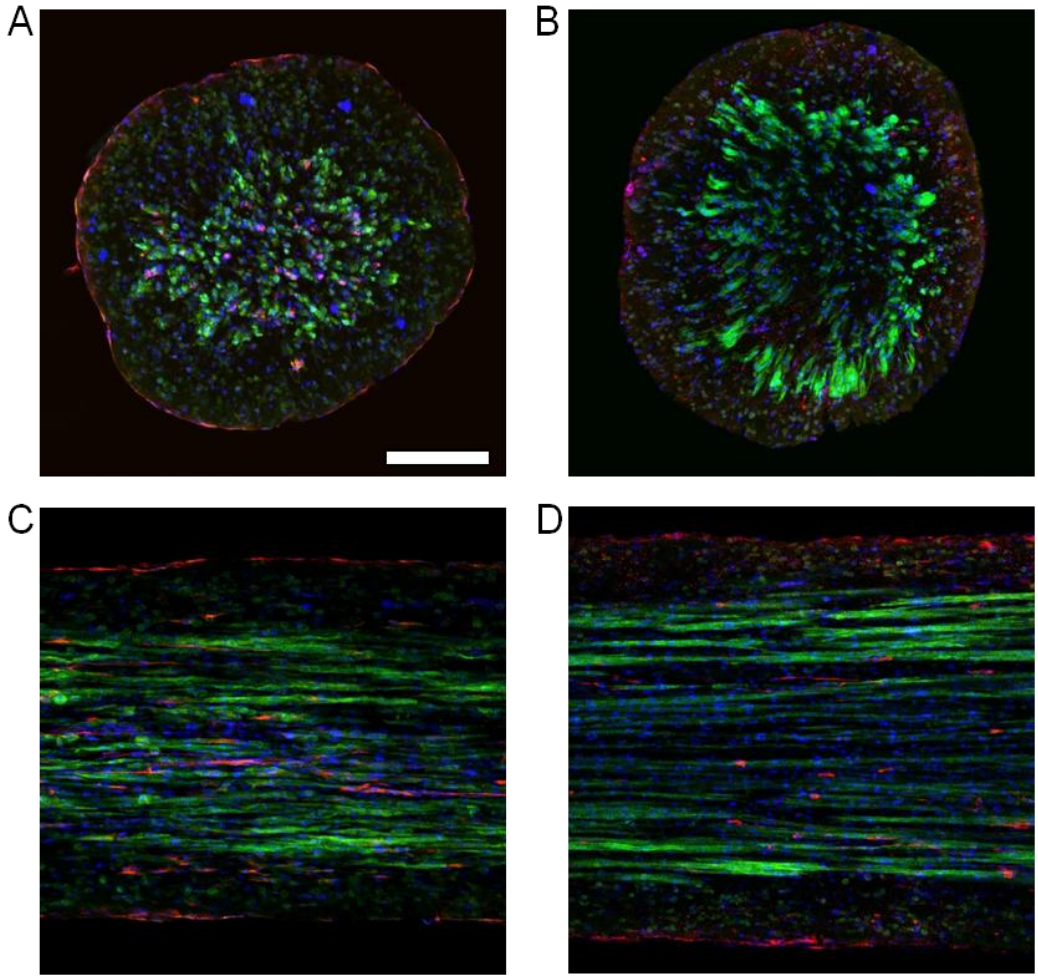

Figure 4.4 – Typical central confocal images of nonstimulated (A, C) and stimulated (B,D) engineered tissue stained with actinin (green) to identify myocytes, vimentin (red) to identify fibroblasts, and DAPI (blue) to identify nuclei. (A-B) Transverse and (C-D) longitudinal cross-sections. Dense regions of myocytes were found approximately 200 μm from the periphery of the sample. Fibroblasts were found in close spatial proximity to myocytes. Scale bar: (A) 200 μm applies to all.

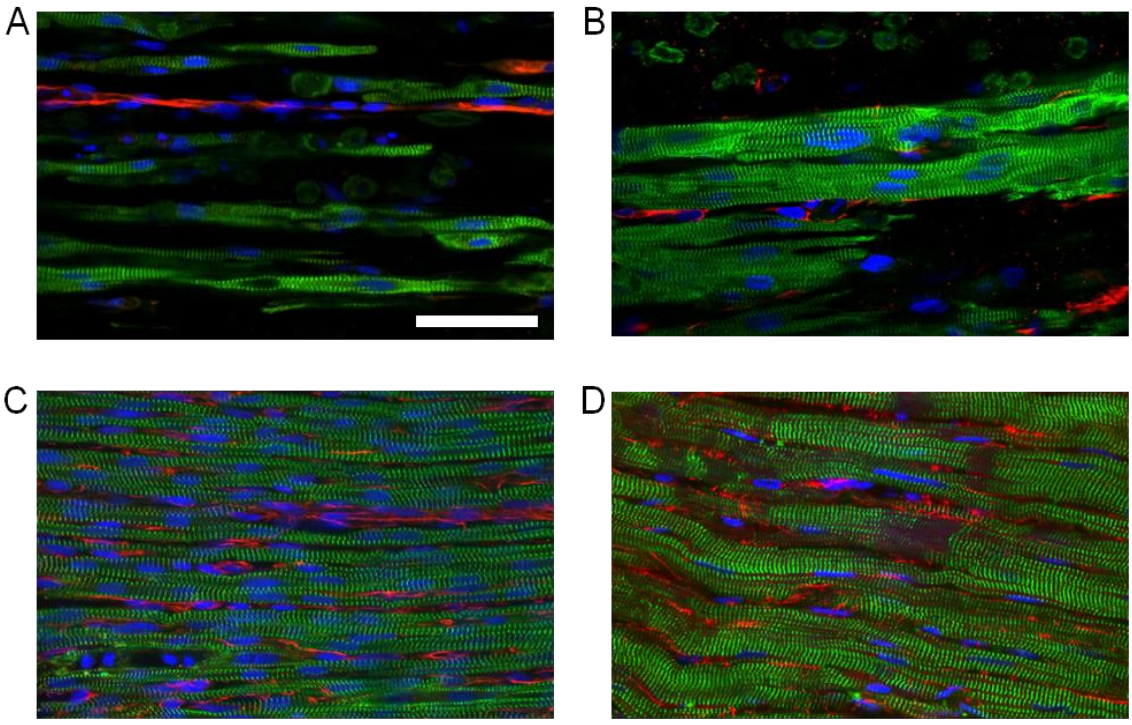

Figure 4.5 – Typical confocal images of cardiac tissue samples stained with actinin (green) to identify myocytes, vimentin (red) to identify fibroblasts, and DAPI (blue) to identify nuclei. Engineered tissue from nonstimulated (A) and stimulated (B) samples cultured for 12 days. Left ventricular myocardium from P12 (C) and adult (D) rats. Myocytes and fibroblasts are in close spatial proximity. Visually, the stimulated sample (B) has more densely packed myocytes compared to the nonstimulated sample (A). P12 and adult rat myocardium has densely packed myocytes and fibroblasts. Scale bar: (A) 50 μm applies to all.

4.4.2 Functional Analysis

ET and MCR were measured at days 6, 9 and 12 of culture and for isolated strips of P3 left ventricular myocardium. ET and MCR were not measurable at day 3 of culture as the samples did not respond to pacing. The ET decreased as a function of time in culture for both nonstimulated and stimulated samples, and the stimulated samples nearly approached the ET of P3 rat myocardium (Fig. 4.6). Stimulated samples had significantly lower ET at day 6 (2.79±0.15 vs. 3.85±0.29 V/cm), 9 (1.78±0.13 vs. 2.93±0.13 V/cm) and 12 (1.00±0.12 vs. 2.46±0.08 V/cm) of culture compared to nonstimulated samples ($p<0.01$). MCR increased as a function of time in culture for the stimulated group and exceeded that of P3 native myocardium by the end of culture ($p<0.01$). Nonstimulated samples exhibited an increase in MCR between days 6 and 9 ($p<0.01$), but not between days 9 and 12 ($p>0.05$). Furthermore, the stimulated samples had significantly higher MCR at days 6 (374±51 vs. 273±25 beats/min), 9 (569±40 vs. 379±33 beats/min) and 12 (645±39 vs. 393±18 beats/min) of culture compared to nonstimulated samples ($p<0.01$).

4.4.3 3D Confocal Imaging

Three-dimensional confocal imaging and image analysis were applied to 9 nonstimulated and 12 electrically stimulated engineered tissue constructs and 5 P12 hearts and 7 adult hearts. The approach was applied to preparations stained with WGA, α-sarcomeric actinin, Cx43 and DAPI. Seventy-one image stacks from the 4 experimental groups were obtained. Image stacks with low SNR or motion artifact were removed for further analysis. Final data were obtained from 7 nonstimulated samples (n=11 image stacks), 7 stimulated samples (n=13 stacks), 5 P12 hearts (n=8 image stacks) and 7 adult

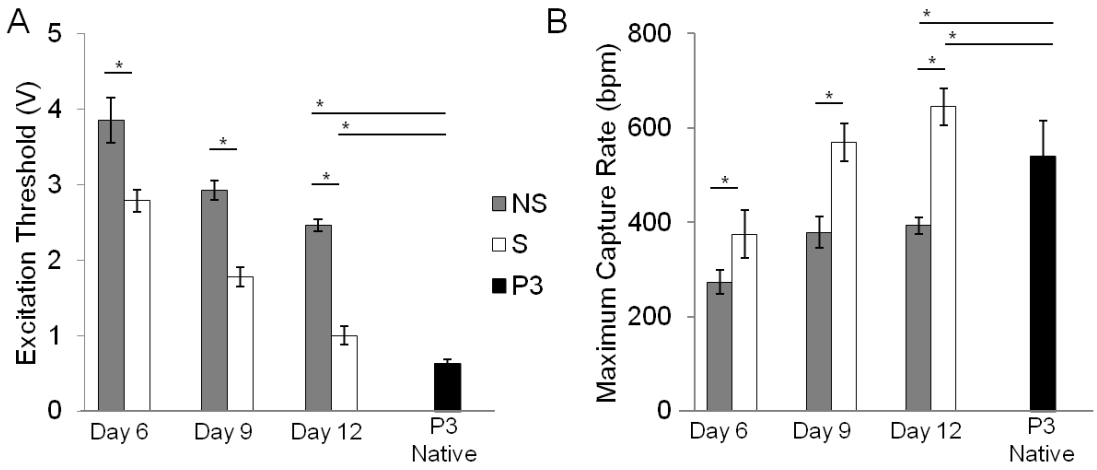

Figure 4.6 – (A) Excitation threshold and (B) maximum capture rate at Days 6, 9, and 12 of culture and postnatal day 3 rat hearts. Excitation threshold progressively decreased and maximum capture rate progressively increased as a function of time in culture. * Denotes statistical difference in means determined by post-hoc Tukey-Kramer tests (α=0.05).

hearts (n=13 image stacks). Raw image data for engineered tissue samples are presented in Fig. 4.7. These stacks originate from ~1 μm outside the tissue surface and extend ~50 μm into the tissue sample.

Processed image stacks from all groups confirmed that myocytes exhibited an elongated morphology (Figs. 4.8 and 4.9). Marked differences between the nonstimulated and stimulated samples were visually noticeable in the 3D image stacks. The stimulated group exhibited more densely packed myocytes with a more pronounced elongated morphology (Fig 4.8A, E), aligned sarcomeres in registry (Fig 4.8C, G), and more Cx43 plaque formation on the myocyte membrane (Fig 4.8D, H). Marked differences between P12 and adult tissue were also apparent by visual observation (Fig. 4.9). P12 myocytes appeared smaller in size (Fig 4.9A, D) and had Cx43 plaque formation around the lateral sarcolemma (Fig 4.9D), whereas adult myocytes had Cx43 plaque formation primarily at cell ends (Fig. 4.9H).

4.4.4 Myocyte Volume Fraction

MVF was quantified by down-sampling the processed 3D image data for the α-sarcomeric actinin labeling (Fig. 4.10). Down-sampling of the original images (Fig. 4.10A-B) resulted in "blurring" of the actinin-associated intensities (Fig. 4.10C-D). Thresholding of the down-sampled images resulted in identification of the intracellular space of myocytes (Fig. 4.10E-F). The MVF was nearly double for the stimulated engineered tissue compared to nonstimulated (0.34±0.14 vs. 0.18±0.06, $p<0.01$). However, the MVF for both nonstimulated (0.18±0.06) and stimulated (0.34±0.14)

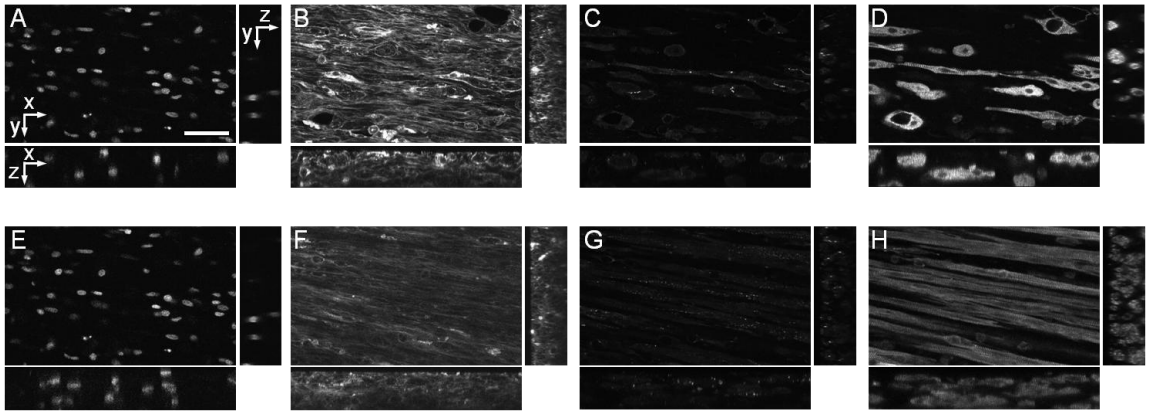

Figure 4.7 – Raw 3D image data of nonstimulated (A-D) and stimulated (E-H) engineered cardiac tissue. (A, E) DAPI, (B, F) WGA, (C, G) Cx43 and (D, H) α-sarcomeric actinin. Scale bar: (A) 50 μm applies to all.

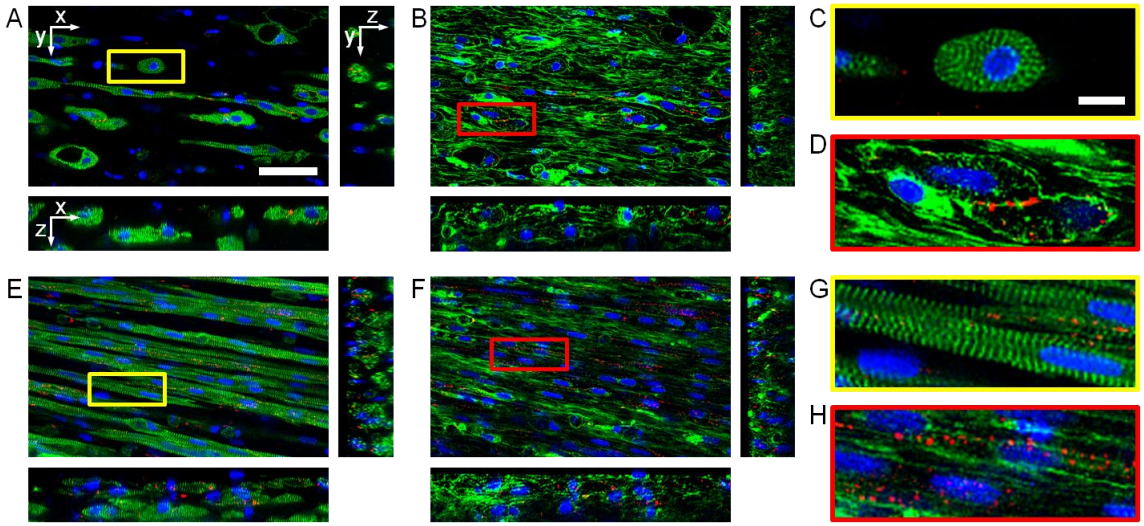

Figure 4.8 – Processed 3D image data of nonstimulated (A-D) and electrically stimulated (E-H) engineered cardiac tissue. (A, E) DAPI (blue), α-sarcomeric actinin (green) and Cx43 (red). (B, F) DAPI (blue), WGA (green) and Cx43 (red). (C, D, G, H) Zoomed region of (A, B, E, F, respectively) indicated by box. Scale bar: (A) 50 µm also applies to B, E and F, and (C) 10 µm also applies to D, G and H.

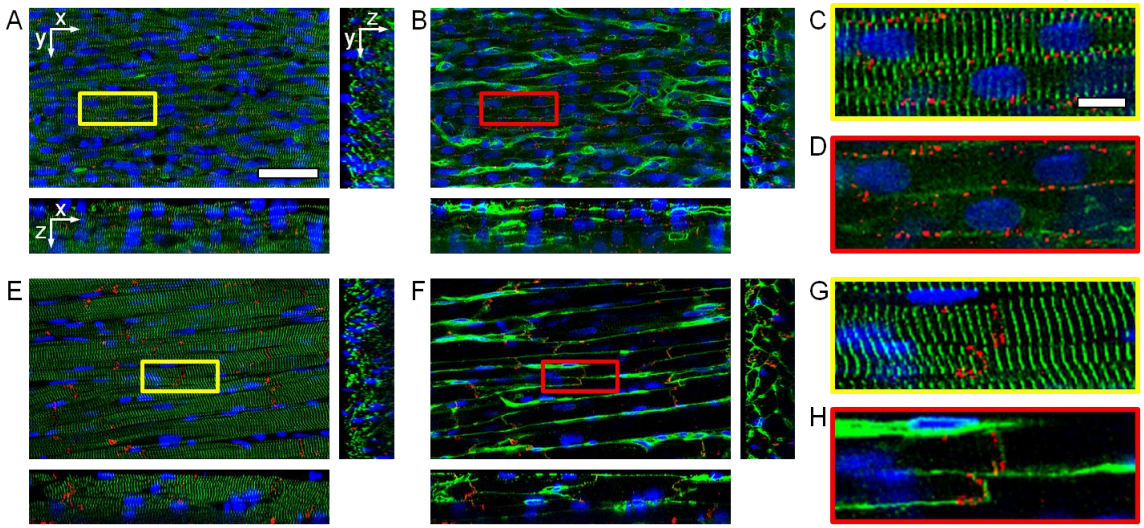

Figure 4.9 – Processed 3D image data of P12 (A-D) and adult (E-H) native left ventricular cardiac tissue. (A, E) DAPI (blue), α-sarcomeric actinin (green) and Cx43 (red). (B, F) DAPI (blue), WGA (green) and Cx43 (red). (C, D, G, H) Zoomed region of (A, B, E, F, respectively) indicated by box. Scale bar: (A) 50 µm also applies to B, E and F, and (C) 10 µm also applies to D, G and H.

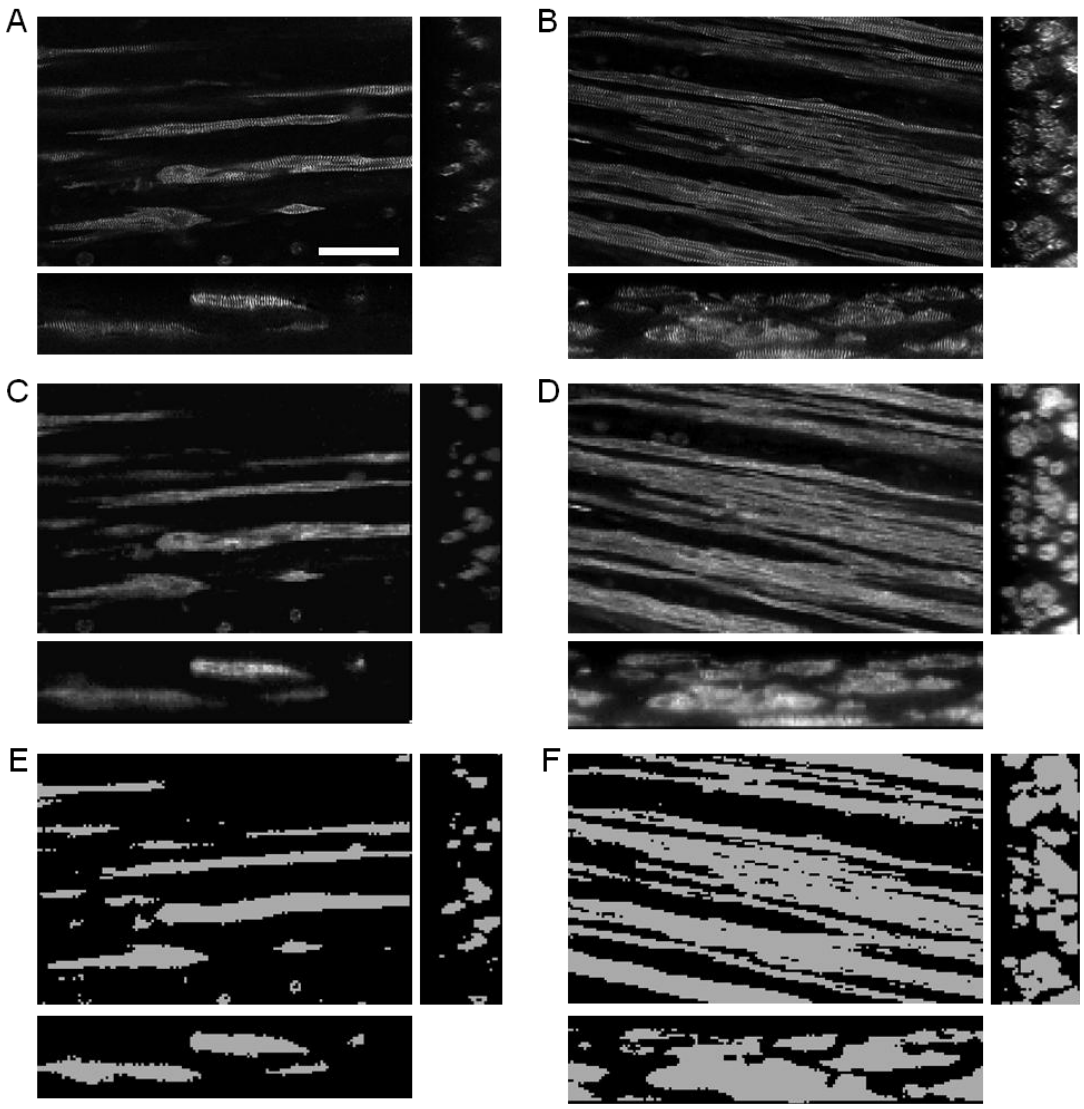

Figure 4.10 – Calculating myocyte volume fraction (MVF) in 3D image stacks. Actinin labeling (A, B) is resampled at 1.6 μm resolution (C, D) and thresholded (E, F) to estimate MVF. Nonstimulated (A, C, E) and stimulated (B, D, F). Scale bar: (A) 50 μm applies to B-F.

engineered tissue was significantly lower than that of P12 (0.90±0.06) and adult (0.91±0.04) myocardium ($p<0.01$).

4.4.5 Myocyte Segmentation and Cx43 Analysis

Myocyte geometry was quantified through segmentation of individual cells from the 3D image stacks. The segmentation process is shown in Fig. 4.11 with example myocytes from the four experimental groups. Manual manipulation of 3D triangle meshes and thresholding of the WGA channel were used to create 3D reconstructions of myocytes. Central cross-sections of the reconstructed myocytes (Figs. 4.11A, D, G and J) served for masking the WGA and Cx43 image data (Figs. 4.11B, E, H and K). 3D visualizations of the segmented myocytes and associated Cx43 labeling are shown in Figs. 4.11C, F, I and L. Myocyte geometry was calculated from the segmented cells (Fig. 4.12). Adult myocytes were significantly larger in length, width, height, surface area and volume compared to nonstimulated and stimulated engineered tissue and P12 native rat myocardium. Length, width, height, surface area and volume were not statistically different between myocytes from electrically stimulated tissue samples and P12 native myocardium. However, nonstimulated myocytes had more often a rounded morphology as indicated by a smaller mean length compared to stimulated and P12 myocytes and higher widths and heights compared to stimulated myocytes.

The spatial distribution of Cx43 was characterized through projections of Cx43 intensities on myocyte eigenvectors e_1, e_2 and e_3 and measures of polarization and higher-order statistical moments. Fig. 4.13 shows the profile projections for the segmented example cells in Fig. 4.11. In the nonstimulated myocyte there was little Cx43 plaque

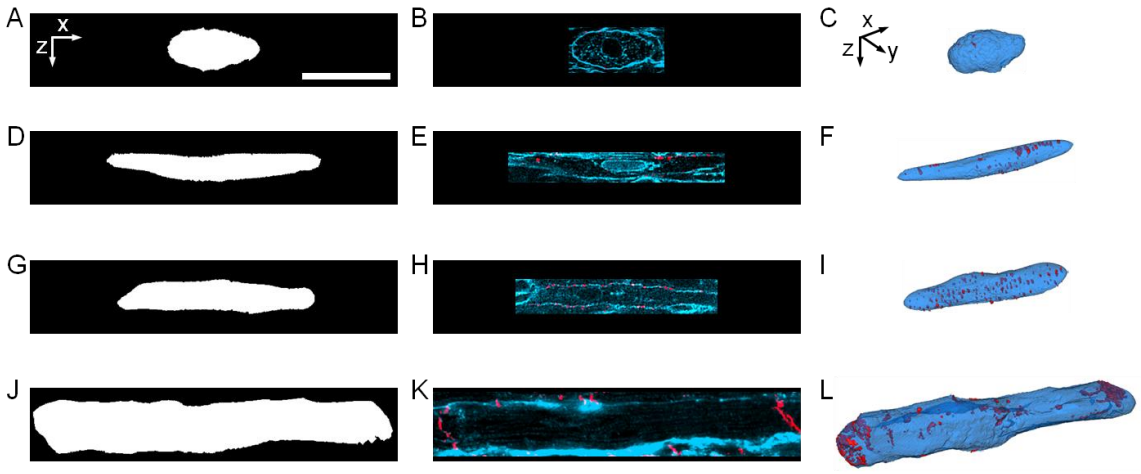

Figure 4.11 – Myocyte segmentation and visualization. (A-C) Nonstimulated, (D-F) stimulated, (G-I) P12 rat and (J-L) adult rat. (A, D, G, J) Central XZ-section of segmented myocyte (white) from image stack. (B, E, H, K) Corresponding central XZ-section of image stack with WGA (blue) and Cx43 (red). (C, F, I, L) 3D visualization of segmented cells (blue) and Cx43 (red). Scale bar: (A) 30 µm applies to all.

A

	Length (μm)	Width (μm)	Height (μm)	Volume ($μm^3$)	Surface Area ($μm^2$)	Myocyte Volume Fraction
Nonstimulated samples n=7 segmented cells n=64	58.8 ± 21.8	13.0 ± 2.7	10.1 ± 2.5	2647 ± 790	1400 ± 381	0.18 ± 0.06
Stimulated samples n=7 segmented cells n=58	81.5 ± 19.7	11.3 ± 2.0	8.6 ± 1.6	2968 ± 1296	1775 ± 585	0.34 ± 0.14
Postnatal Day 12 (P12) rats n=5 segmented cells n=41	72.0 ± 10.9	11.5 ± 1.6	9.1 ± 1.3	3167 ± 783	1732 ± 344	0.90 ± 0.06
Adult rats n=7 segmented cells n=51	120.1 ± 31.3	29.4 ± 5.9	19.6 ± 3.3	26916 ± 11550	7431 ± 2555	0.91 ± 0.04

B

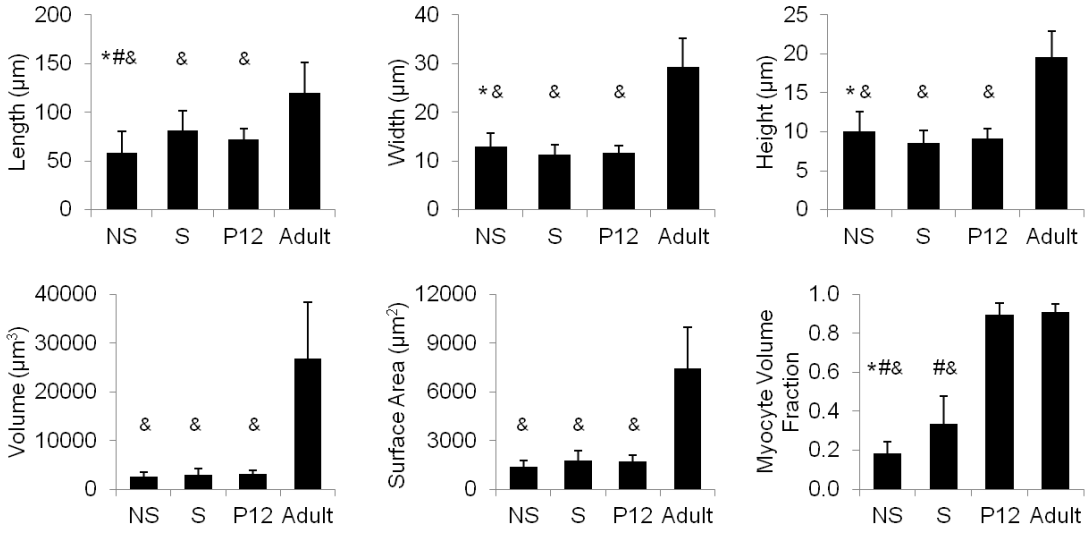

Figure 4.12 – Myocyte geometry and volume fraction. (A) Table showing mean ± standard deviation. (B) Graphical representation of data from (A). Statistical difference in means determined by post-hoc Tukey-Kramer tests (α=0.05). Symbols denote difference from *Stimulated, #P12 and &Adult.

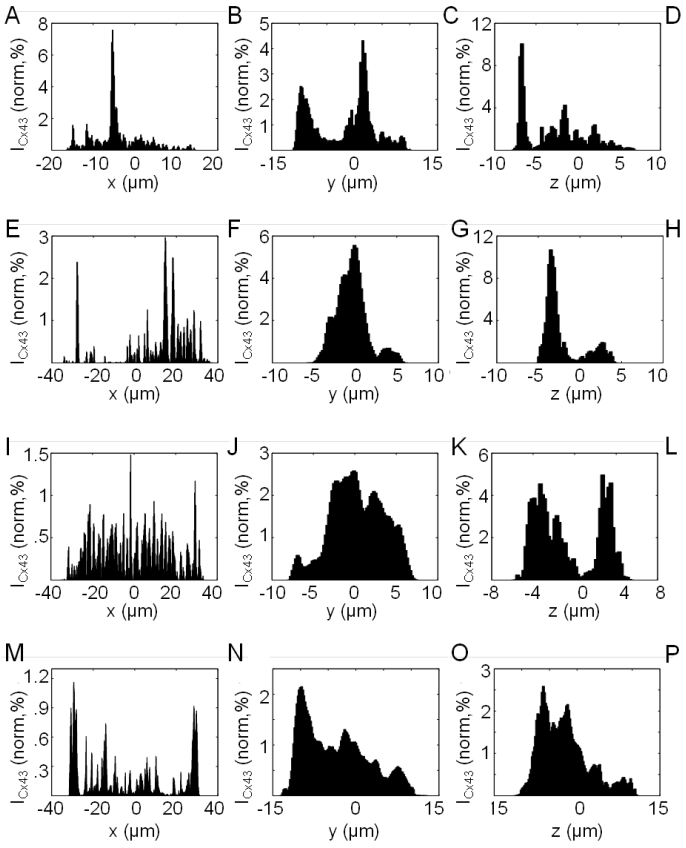

Measure	Value
Membrane Cx43 Positive	2.5%
$Pol_{25\%e1}$ min, max, total	3.5%, 20.2%, 23.7%
$Pol_{25\%e2}$ min, max, total	7.2%, 33.4%, 40.6%
$Pol_{25\%e3}$ min, max, total	4.9%, 37.4%, 42.3%
Skewness γ_{1e1}, γ_{1e2}, γ_{1e3}	0.61, -0.13, 0.36
Kurtosis γ_{2e1}, γ_{2e2}, γ_{2e3}	0.70, -1.19, -0.93

Measure	Value
Membrane Cx43 Positive	5.5%
$Pol_{25\%e1}$ min, max, total	14.4%, 32.1%, 46.5%
$Pol_{25\%e2}$ min, max, total	4.2%, 6.9%, 11.0%
$Pol_{25\%e3}$ min, max, total	10.1%, 67.1%, 77.2%
Skewness γ_{1e1}, γ_{1e2}, γ_{1e3}	-1.24, 0.66, 1.27
Kurtosis γ_{2e1}, γ_{2e2}, γ_{2e3}	0.49, 0.77, 0.15

Measure	Value
Membrane Cx43 Positive	6.3%
$Pol_{25\%e1}$ min, max, total	16.2%, 19.2%, 35.4%
$Pol_{25\%e2}$ min, max, total	7.6%, 14.5%, 22.2%
$Pol_{25\%e3}$ min, max, total	23.5%, 27.5%, 51.0%
Skewness γ_{1e1}, γ_{1e2}, γ_{1e3}	0.12, -0.13, 0.29
Kurtosis γ_{2e1}, γ_{2e2}, γ_{2e3}	-1.00, -0.51, -1.51

Measure	Value
Membrane Cx43 Positive	10.6%
$Pol_{25\%e1}$ min, max, total	26.7%, 37.3%, 64.0%
$Pol_{25\%e2}$ min, max, total	7.3%, 37.4%, 44.7%
$Pol_{25\%e3}$ min, max, total	7.0%, 25%, 32.0%
Skewness γ_{1e1}, γ_{1e2}, γ_{1e3}	0.31, 0.50, 0.83
Kurtosis γ_{2e1}, γ_{2e2}, γ_{2e3}	-1.42, -0.78, 0.22

Figure 4.13 – Cx43 intensity profiles from cells in Fig. 4.11. (A-D) Nonstimulated, (E-H) stimulated, (I-L) P12 rat and (M-P) adult rat. Profiles were produced by projection of Cx43 intensities on the principal axes e_1 (A, E, I, M), e_2 (B, F, J, N) and e_3 (C, G, K, O). Respective quantitative results from example cells are shown in D, H, L and P.

formation indicated by the low percent membrane positive for Cx43 (Fig. 4.13D), and a large plaque dominated the profiles as indicated by a sharp peak in the Cx43 projection profiles (Figs. 4.13A-C). The stimulated myocyte had the majority of Cx43 plaque formation on one end of the cell as can be seen in the profile on eigenvector e_1 (Fig. 4.13D) and the large difference between $Pol_{25\%e1min}$ and $Pol_{25\%e1max}$ and strong negative skewness (γ_{1e1}) (Fig. 4.13H). The P12 myocyte had an approximately uniform distribution of Cx43 around the lateral membrane as can be seen in the profile for eigenvector e_1 (Fig. 4.13I). The distribution had a skewness (γ_{1e1}) near zero and a kurtosis near -1.2 which indicates a uniform distribution (Fig. 4.13L). Furthermore, the profile for eigenvector e_3 (Fig. 4.13K) for the P12 myocyte showed a bimodal distribution, which indicates that Cx43 plaques were concentrated on the lateral sarcolemma as opposed to cell ends as seen in the adult myocyte. The adult myocyte had the majority of Cx43 associated intensities at cell ends which can be seen from projections for eigenvector e_1 (Fig. 4.13M) and a $Pol_{25\%e1total}$ greater than 50%. The Cx43 distribution was weakly asymmetric as indicated by a small difference in $Pol_{25\%e1min}$ and $Pol_{25\%e1max}$ and a small positive skewness (γ_{1e1}).

The extent of Cx43 plaque formation was assessed through calculating the percentage of membrane positive for Cx43 staining on segmented myocytes. Nonstimulated engineered tissue had a significantly lower percentage of the membrane area stained positive for Cx43 (3.5±3.4%) compared to stimulated engineered tissue (6.9±3.8%) and that of P12 (7.1±2.3%) and adult (8.3±4.8%) rat myocardium (Fig. 4.14) ($p<0.01$).

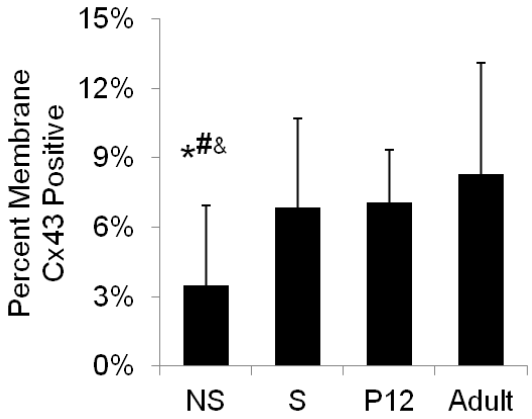

Figure 4.14 – Percentage of membrane stained positive for Cx43. Statistical difference in means determined by post-hoc Tukey-Kramer tests (α=0.05). Symbols denote difference from *Stimulated, $^{\#}$P12 and $^{\&}$Adult.

Statistical results of Cx43 profiles for all segmented cells are presented in Fig. 4.15. Myocytes from nonstimulated and stimulated engineered tissue and P12 native myocardium exhibited no polarization of Cx43, whereas adult myocytes had the majority of their Cx43 concentrated at cell ends (Fig. 4.15A). Nonstimulated myocytes had a large difference in $Pol_{25\%e1min}$ and $Pol_{25\%e1max}$ (Fig. 4.15A) and a high standard deviation of skewness (Fig. 4.15B) indicating that most cells had Cx43 plaques concentrated on one side of the myocyte. Furthermore, the measured skewness (Fig. 4.15B, E, H) and kurtosis (Fig. 4.15C, F, I) was highly variable for the nonstimulated group compared to all other groups for all three eigenvector profiles.

4.5 Discussion

In this study we applied 3D confocal imaging and analysis to test the hypothesis that environmental cues direct engineered tissue towards a phenotype resembling that of age-matched native myocardium. We characterized effects of electrical stimulation on myocyte geometry and the spatial distribution of Cx43 in engineered cardiac tissue, and applied the same techniques for characterization to age-matched and adult native tissue. The results of the study support the hypothesis that electrical stimulation directs engineered cardiac tissue towards a phenotype resembling that of age-matched native myocardium. Adult myocytes were found to have significantly different geometries and Cx43 distributions compared to both engineered tissue constructs and P12 myocardium (Figs. 4.12, 4.14, and 4.15). This suggests that age-matched native tissue serves as a more realistic target for both analytical comparison and development of design specifications for engineered tissue samples.

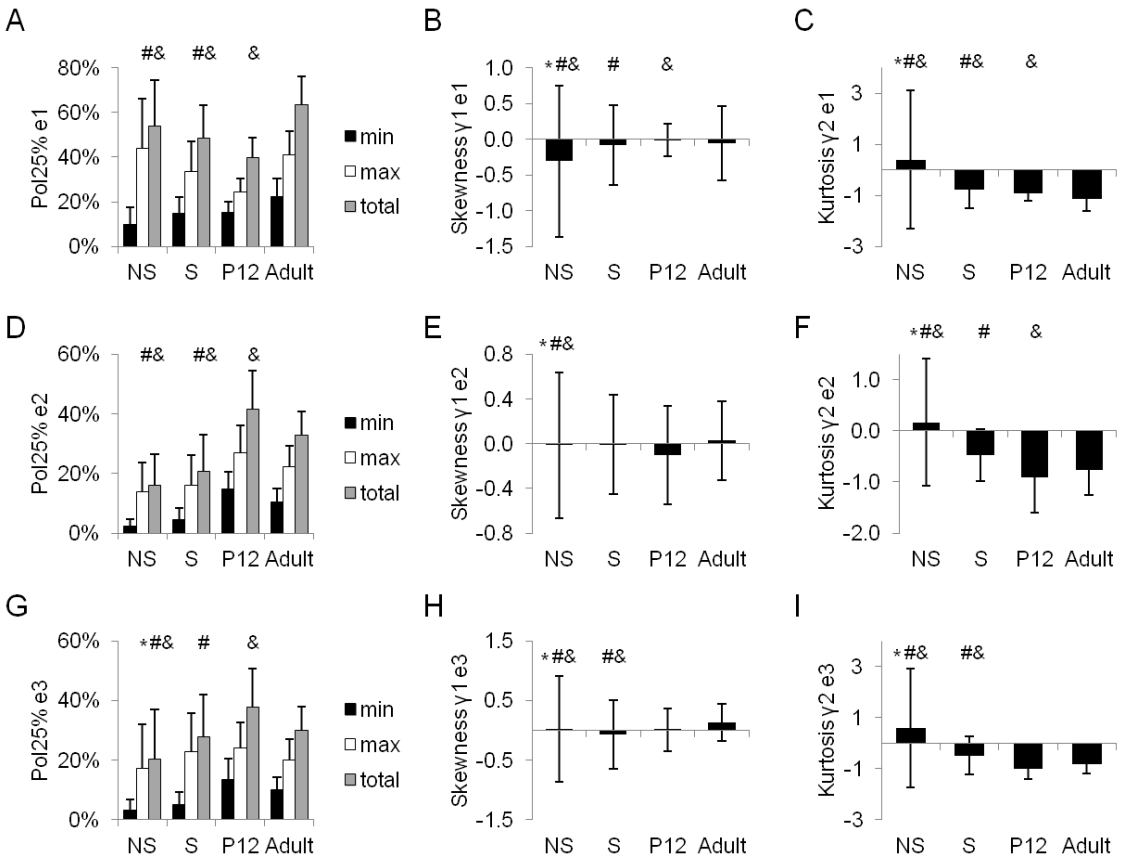

Figure 4.15 – Quantitative results of Cx43 analysis. Polarization ($Pol_{25\%}$) (A, D, G), skewness (B, E, H) and kurtosis (C, F, I) for principal axes e_1 (A-C), e_2 (D-F) and e_3 (G-I). Statistical difference in means of total Cx43 polarization ($Pol_{25\%}$) (A, D, G) determined by post-hoc Tukey-Kramer tests (α=0.05) and variance of skewness (B, E, H) and kurtosis (C, F, I) determined by F-tests (α=0.05). Symbols denote difference from *Stimulated, $^{\#}$P12 and $^{\&}$Adult.

Although other studies have elucidated some of the effects of electrical stimulation on the development of engineered cardiac tissue [22, 28, 29]. A novelty of our study is in the comprehensive 3D imaging and analysis approach and quantitative comparison to native tissue. A key feature of the approach is the ability to extract individual myocytes from the image data and assign a reliable coordinate system from which measures of geometry and Cx43 are computed. The common approach of 2D imaging produces a single cross-section through a cell, which increases the chances of misinterpreting or overlooking data and introducing variability.

The approach for fabricating tissue samples was based on methods described by Hansen *et al.* [38] and selected because of its success in producing tissue samples with densely packed, aligned myocytes. Both nonstimulated and stimulated engineered tissue samples showed dense regions of myocytes and fibroblasts, the two most abundant cell types in the heart (Fig. 4.4). Our observations of tissue sample development are in agreement with Hansen *et al.* [38]. Samples condensed to approximately 20% of their initial cross-sectional area (Fig. 4.3), and this process was independent of electrical stimulation. Cells appeared to have a rounded morphology and be homogeneously distributed through the sample at the beginning of culture. After 3-6 days in culture cells began to elongate, align and contract in isolated regions of the sample. Contracting regions increased in size between 6-9 days of culture and whole samples were macroscopically observed to contract by the end of culture (day 12).

In this study, electrical stimulation had a high impact on MVF. Although the MVF for the electrically stimulated group was less than half of that of P12 and adult myocardium, it was nearly double compared to nonstimulated samples. We suggest that

the increase in MVF in the electrically stimulated group is caused by more myocytes developing and maturing. This notion is supported by the fact that both the nonstimulated and stimulated samples started with the same number of cells, construct sizes were not statistically different at the end of culture (Fig. 4.3), and myocytes did not differ in volume (Fig. 4.12).

Myocytes subjected to electrical stimulation had geometries and Cx43 distributions which more closely matched P12 myocardium compared to nonstimulated myocytes and native adult myocytes. Under electrical stimulation myocytes were found to assume an elongated morphology as opposed to their nonstimulated counterparts, which often had a rounded morphology. This is consistent with previous studies [22]. Furthermore, sarcomeres were often disorganized in nonstimulated myocytes (Fig. 4.8C) compared to stimulated samples, P12 and adult tissue (Fig. 4.8G and Fig 4.9C, G, respectively). Moreover, electrical stimulation was found to increase the percentage of membrane positive for Cx43 plaques compared to nonstimulated samples (Fig 4.14). In fact, the percentage of membrane positive for Cx43 in the electrically stimulated group was not statistically different from P12 or adult rat myocardium.

Previous studies have reported the spatiotemporal dynamics of Cx43 in postnatal development of rat [18] and human cardiac tissue [19]. In neonatal rat cardiac tissue, Cx43 plaques were found to be uniformly distributed over the myocyte membrane and remodeled to become concentrated at cell ends (i.e., polarization) at approximately 90 days. In adult rat myocytes, Cx43 is mostly located at cell ends which was found in our previous [35] and other studies [15, 43]. Thus, our findings in this study are in agreement as P12 myocytes had no preference for Cx43 plaques at cell ends ($Pol_{25\%}$=40±9%)

compared to adult myocytes which showed the majority of Cx43 plaques were found at cell ends ($Pol_{25\%}$=63±13%). Myocytes from both engineered tissue groups were similar to P12 myocytes and had no significant Cx43 polarization. Cx43 profiles showed that myocytes from all groups had significant variability with respect to symmetry and polarization. Projections of Cx43 intensities on eigenvector e_1 indicated that the nonstimulated myocytes had the largest difference between $Pol_{25\%min}$ and $Pol_{25\%max}$, which was reflected in the large standard deviation of the skewness. Projections on eigenvectors e_2 and e_3 showed that the P12 myocytes had significant polarization indicating that Cx43 plaques were located along the lateral sarcolemma as opposed to centralized regions of cell ends as in adult tissue. The nonstimulated myocytes had the highest standard deviation in both measures of skewness and kurtosis for intensity profiles on all axes, suggesting high variability with respect to Cx43 distributions.

Functional measures of ET and MCR were found to be influenced by electrical stimulation (Fig. 4.6). The lower ET and higher MCR found in the electrically stimulated group are in agreement with other studies which have applied electrical stimulation [22, 29, 33]. The measured ET of 0.63±0.05 V/cm and MCR of 541±75 beats/min for P3 neonatal ventricles measured in this study were in close agreement with other studies which ranged from 0.74±0.2 to 1.6±0.1 V/cm for ET and 413±7 to 475±25 beats/min for MCR [33, 44].

4.5.1 Applications of Developed Approaches

An application of the developed approach is to define specifications for tissue engineering. Specifications are paramount to the engineering paradigm and tissue

engineering is no exception. In this study, specifications were derived from normal age-matched and adult left ventricular myocardium of rat since a central goal of tissue engineering is reestablishing features of the native myocardium. However, specifications can be derived for any requirement, for example, diseased cardiac tissue where the focus may be to understand the effects of pharmaceutical agents [1, 38].

Another application of the imaging approach and analysis is to characterize structural features of stem cell-based engineered tissue samples. Induced pluripotent human stem cells have the potential to differentiate into any cell type [45, 46], and have been specifically differentiated to cardiomyocytes [47]. However, their application in developing 3D tissue constructs is in its infancy [48].

The imaging approach can also be applied to characterize other structural features of cardiac tissue. Sarcomeric actinin staining revealed that many myocytes in the nonstimulated group had sarcomeres that appeared to be disorganized compared to the stimulated, P12 and adult myocytes, which had well defined sarcomeres in registry. Fibroblasts, the majority of cells in the heart, play an important role in normal cardiac function such as maintaining the extracellular matrix, paracrine signaling, and cell-cell communication with myocytes and other fibroblasts [7, 8, 49]. Quantifying sarcomere organization and the spatial relationship of myocytes and fibroblast is of interest for future studies. Furthermore, measurements of function could be used in conjunction with the structural features quantified in this study to elucidate the complex structure-function relationships found in cardiac tissue. Moreover, the application of other environmental conditions, such as the combinational effects of electrical and mechanical stimulation, is of interest for future work.

4.5.2 Limitations

Limitations relating to the preparation of native cardiac tissue are described in our previous study [35]. Our approach for structural characterization did not determine if the Cx43 labeling resulted in functional gap junctions. Assessment of phosphorylation [50] and colocalization with N-cadherin [51, 52] can offer insight into the potential functionality, but were not performed in this study. Furthermore, the total Cx43 expression was not quantified in this study. Instead measures of the percent membrane positive for Cx43 were characterized, which can serve as indirect measure Cx43 expression. Furthermore, the phenotype of the fibroblasts found in our engineered tissue constructs was not characterized. Fibroblasts can differentiate into myofibroblasts in culture, and the myofibroblastic phenotype can be present in injured myocardium [53]. Myofibroblasts are responsible for remodeling the ECM and paracrine signaling, however, their effects on engineered tissue have not been studied [54].

Functional analyses were limited to measures of ET and MCR. Although these measures are well established in the field [22, 29, 33], other functional measures of, for instance, electrical conduction and excitation-contraction coupling, would be beneficial for comprehensive assessment of tissue constructs. However, the focus of this study was on characterizing structure through 3D confocal imaging and not on functional analyses. Measures of cardiac structure are not limited to myocyte geometry and Cx43 distributions. However, those were selected because they are known to influence functional properties and undergo significant changes during development and diseased states [11-13].

Some of our image data required cross-talk correction, which is an a posteriori method based on detailed investigation of signal intensities. Images co-stained with α-sarcomeric actinin and vimentin exhibited cross-reactivity of vimentin secondary (Cy3) with α-sarcomeric actinin primary, i.e., actinin exhibited both Alexa Fluor 633 and Cy3 fluorophores. The cross-reactivity is due to the same species and isotype (mouse IgG_1) of the antibodies. Vimentin antibodies raised in different species do exist and were tried in this study (e.g. Anti-Vimentin, C-Terminal antibody produced in rabbit, Sigma-Aldrich, St. Louis, MO, SAB4503083), however, without success.

The described method for myocyte segmentation requires 3D confocal imaging and manual manipulation of triangle meshes, both of which are inherently time consuming and tedious. Automated methods for image acquisition and myocyte segmentation are a possible solution to this issue and will be addressed in future work. A further limitation of the presented approach is related to the volume of imaged regions. Each image stack spans approximately 200 × 150 × 50 μm of the sample volume. To overcome the relatively small volume of the image stack, several image stacks were obtained and only regions dense with myocytes were imaged. Dense regions were identified by scanning the sample with a 10x objective lens.

4.6 References

[1] N. T. Elliott and F. Yuan, "A review of three-dimensional in vitro tissue models for drug discovery and transport studies," *J Pharm Sci,* vol. 100, pp. 59-74, 2011.

[2] L. G. Griffith and M. A. Swartz, "Capturing complex 3D tissue physiology in vitro," *Nat Rev Mol Cell Biol,* vol. 7, pp. 211-224, 2006.

[3] A. G. Mikos, S. W. Herring, P. Ochareon, J. Elisseeff, H. H. Lu, R. Kandel, F. J. Schoen, M. Toner, D. Mooney, and A. Atala, "Engineering complex tissues," *Tissue Eng,* vol. 12, pp. 3307-3339, 2006.

[4] J. A. Hill and E. N. Olson, "Cardiac plasticity," *N Engl J Med,* vol. 358, pp. 1370-1380, 2008.

[5] P. Ahuja, P. Sdek, and W. R. MacLellan, "Cardiac myocyte cell cycle control in development, disease, and regeneration," *Physiol Rev,* vol. 87, pp. 521-544, 2007.

[6] I. Banerjee, J. W. Fuseler, R. L. Price, T. K. Borg, and T. A. Baudino, "Determination of cell types and numbers during cardiac development in the neonatal and adult rat and mouse," *Am J Physiol Heart Circ Physiol,* vol. 293, pp. H1883-1891, 2007.

[7] C. A. Souders, S. L. K. Bowers, and T. A. Baudino, "Cardiac fibroblast: the renaissance cell," *Circ Res,* vol. 105, pp. 1164-1176, 2009.

[8] R. Kakkar and R. T. Lee, "Intramyocardial fibroblast myocyte communication," *Circ Res,* vol. 106, pp. 47-57, 2010.

[9] A. C. Nag, "Study of non-muscle cells of the adult mammalian heart: a fine structural analysis and distribution," *Cytobios,* vol. 28, pp. 41-61, 1980.

[10] P. Camelliti, T. K. Borg, and P. Kohl, "Structural and functional characterisation of cardiac fibroblasts," *Cardiovasc Res,* vol. 65, pp. 40-51, 2005.

[11] H. W. Vliegen, A. Laarse, J. A. N. Huysman, E. C. Wijnvoord, M. Mentar, C. J. Cornelisse, and F. Eulderink, "Morphometric quantification of myocyte dimensions validated in normal growing rat hearts and applied to hypertrophic human hearts," *Cardiovasc Res,* vol. 21, pp. 352-357, 1987.

[12] S. E. Campbell, B. Korecky, and K. Rakusan, "Remodeling of myocyte dimensions in hypertrophic and atrophic rat hearts," *Circ Res,* vol. 68, pp. 984-996, 1991.

[13] B. Swynghedauw, "Molecular mechanisms of myocardial remodeling," *Physiol Rev,* vol. 79, pp. 215-262, 1999.

[14] B. E. J. Teunissen, H. J. Jongsma, and M. F. A. Bierhuizen, "Regulation of myocardial connexins during hypertrophic remodelling," *Eur Heart J,* vol. 25, pp. 1979-1989, 2004.

[15] N. J. Severs, E. Dupont, S. R. Coppen, D. Halliday, E. Inett, D. Baylis, and S. Rothery, "Remodelling of gap junctions and connexin expression in heart disease," *Biochim Biophys Acta,* vol. 1662, pp. 138-148, 2004.

[16] H. A. Fozzard, "Gap junctions and liminal length in hypertrophy: something old and something new," *J Cardiovasc Electrophysiol,* vol. 12, pp. 836-837, 2001.

[17] M. A. Beardslee, J. G. Laing, E. C. Beyer, and J. E. Saffitz, "Rapid turnover of connexin43 in the adult rat heart," *Circ Res,* vol. 83, pp. 629-635, 1998.

[18] B. D. Angst, L. U. R. Khan, N. J. Severs, K. Whitely, S. Rothery, R. P. Thompson, A. I. Magee, and R. G. Gourdie, "Dissociated spatial patterning of gap junctions and cell adhesion junctions during postnatal differentiation of ventricular myocardium," *Circ Res,* vol. 80, pp. 88-94, 1997.

[19] N. S. Peters, N. J. Severs, S. M. Rothery, C. Lincoln, M. H. Yacoub, and C. R. Green, "Spatiotemporal relation between gap junctions and fascia adherens junctions during postnatal development of human ventricular myocardium," *Circulation,* vol. 90, pp. 713-725, 1994.

[20] S. Kostin, S. Dammer, S. Hein, W. P. Klovekorn, E. P. Bauer, and J. Schaper, "Connexin 43 expression and distribution in compensated and decompensated cardiac hypertrophy in patients with aortic stenosis," *Cardiovasc Res,* vol. 62, pp. 426-436, 2004.

[21] A. Salameh, A. Wustmann, S. Karl, K. Blanke, D. Apel, D. Rojas-Gomez, H. Franke, F. W. Mohr, J. Janousek, and S. Dhein, "Cyclic mechanical stretch induces cardiomyocyte orientation and polarization of the gap junction protein connexin43," *Circ Res,* vol. 106, pp. 1592-1602, 2010.

[22] M. Radisic, H. Park, H. Shing, T. Consi, F. J. Schoen, R. Langer, L. E. Freed, and G. Vunjak-Novakovic, "Functional assembly of engineered myocardium by electrical stimulation of cardiac myocytes cultured on scaffolds," *Proc Natl Acad Sci U S A,* vol. 101, pp. 18129-18134, 2004.

[23] T. Eschenhagen, C. Fink, U. Remmers, H. Scholz, J. Wattchow, J. Weil, W. Zimmermann, H. H. Dohmen, H. Schafer, and N. Bishopric, "Three-dimensional reconstitution of embryonic cardiomyocytes in a collagen matrix: a new heart muscle model system," *FASEB J,* vol. 11, pp. 683-694, 1997.

[24] T. Shimizu, M. Yamato, Y. Isoi, T. Akutsu, T. Setomaru, K. Abe, A. Kikuchi, M. Umezu, and T. Okano, "Fabrication of pulsatile cardiac tissue grafts using a novel 3-dimensional cell sheet manipulation technique and temperature-responsive cell culture surfaces," *Circ Res,* vol. 90, p. e40, 2002.

[25] H. C. Ott, T. S. Matthiesen, S. K. Goh, L. D. Black, S. M. Kren, T. I. Netoff, and D. A. Taylor, "Perfusion-decellularized matrix: using nature's platform to engineer a bioartificial heart," *Nat Med,* vol. 14, pp. 213-221, 2008.

[26] W. H. Zimmermann and R. Cesnjevar, "Cardiac tissue engineering: implications for pediatric heart surgery," *Pediatr Cardiol*, vol. 30, pp. 716-723, 2009.

[27] G. Vunjak-Novakovic, K. O. Lui, N. Tandon, and K. R. Chien, "Bioengineering heart muscle: A paradigm for regenerative medicine," *Annu Rev Biomed Eng*, vol. 15, pp. 245-267, 2011.

[28] N. Tandon, A. Marsano, R. Maidhof, L. Wan, H. Park, and G. Vunjak Novakovic, "Optimization of electrical stimulation parameters for cardiac tissue engineering," *J Tissue Eng Regen Med*, vol. 5, pp. e115-125, 2011.

[29] L. L. Chiu, R. K. Iyer, J. P. King, and M. Radisic, "Biphasic electrical field stimulation aids in tissue engineering of multicell-type cardiac organoids," *Tissue Eng Part A*, vol. 17, pp. 1465-1477, 2008.

[30] C. Fink, S. Ergun, D. Kralisch, U. T. E. Remmers, J. Weil, and T. Eschenhagen, "Chronic stretch of engineered heart tissue induces hypertrophy and functional improvement," *FASEB J*, vol. 14, pp. 669-679, 2000.

[31] P. Akhyari, P. W. M. Fedak, R. D. Weisel, T. Y. J. Lee, S. Verma, D. A. G. Mickle, and R. K. Li, "Mechanical stretch regimen enhances the formation of bioengineered autologous cardiac muscle grafts," *Circulation*, vol. 106, pp. I137-I142, 2002.

[32] W. H. Zimmermann, K. Schneiderbanger, P. Schubert, M. Didie, F. Munzel, J. F. Heubach, S. Kostin, W. L. Neuhuber, and T. Eschenhagen, "Tissue engineering of a differentiated cardiac muscle construct," *Circ Res*, vol. 90, pp. 223-230, 2002.

[33] M. Radisic, L. Yang, J. Boublik, R. J. Cohen, R. Langer, L. E. Freed, and G. Vunjak-Novakovic, "Medium perfusion enables engineering of compact and contractile cardiac tissue," *Am J Physiol Heart Circ Physiol*, vol. 286, pp. H507-H516, 2004.

[34] R. A. Lasher, R. W. Hitchcock, and F. B. Sachse, "Towards modeling of cardiac micro-structure with catheter-based confocal microscopy: a novel approach for dye delivery and tissue characterization," *IEEE Trans Med Imaging*, vol. 28, pp. 1156-64, 2009.

[35] D. P. Lackey, E. D. Carruth, R. A. Lasher, J. B. Boenisch, F. B. Sachse, and R. W. Hitchcock, "Three-dimensional modeling and quantitative analysis of gap junction distributions in cardiac tissue," *Ann Biomed Eng*, vol. 39, pp. 2683-2694, 2011.

[36] J. A. Conchello and J. W. Lichtman, "Optical sectioning microscopy," *Nat Methods*, vol. 2, pp. 920-931, 2005.

[37] A. Diaspro, *Confocal and Two-Photon Microscopy: Foundations, Applications, and Advances*. New York: Wiley, 2002.

[38] A. Hansen, A. Eder, M. Bonstrup, M. Flato, M. Mewe, S. Schaaf, B. Aksehirlioglu, A. Schworer, J. Uebeler, and T. Eschenhagen, "Development of a drug screening platform based on engineered heart tissue," *Circ Res,* vol. 107, pp. 35-44, 2010.

[39] N. Tandon, C. Cannizzaro, P. H. G. Chao, R. Maidhof, A. Marsano, H. T. H. Au, M. Radisic, and G. Vunjak-Novakovic, "Electrical stimulation systems for cardiac tissue engineering," *Nat Protoc,* vol. 4, pp. 155-173, 2009.

[40] O. Langendorff, "Untersuchungen am überlebenden Säugetierherzen," *Pflügers Arch,* vol. 61, pp. 291-332, 1895.

[41] E. Savio-Galimberti, J. Frank, M. Inoue, J. I. Goldhaber, M. B. Cannell, J. H. Bridge, and F. B. Sachse, "Novel features of the rabbit transverse tubular system revealed by quantitative analysis of three-dimensional reconstructions from confocal images," *Biophys J,* vol. 95, pp. 2053-2062, 2008.

[42] B. Jahne, *Digital Image Processing: Concepts, Algorithms, and Scientific Applications*. Secaucus: Springer-Verlag New York, Inc., 1993.

[43] P. C. Dolber, E. C. Beyer, J. L. Junker, and M. S. Spach, "Distribution of gap junctions in dog and rat ventricle studied with a double-label technique," *J Mol Cell Cardiol,* vol. 24, pp. 1443-1457, 1992.

[44] N. Bursac, M. Papadaki, R. J. Cohen, F. J. Schoen, S. R. Eisenberg, R. Carrier, G. Vunjak-Novakovic, and L. E. Freed, "Cardiac muscle tissue engineering: toward an in vitro model for electrophysiological studies," *Am J Physiol,* vol. 277, pp. 433-444, 1999.

[45] Y. Shiba, K. D. Hauch, and M. A. Laflamme, "Cardiac applications for human pluripotent stem cells," *Curr Pharm Des,* vol. 15, pp. 2791-2806, 2009.

[46] S. S. Nunes, H. Song, C. K. Chiang, and M. Radisic, "Stem cell-based cardiac tissue engineering," *J Cardiovasc Transl Res,* vol. 4, pp. 592-602, 2011.

[47] J. Zhang, G. F. Wilson, A. G. Soerens, C. H. Koonce, J. Yu, S. P. Palecek, J. A. Thomson, and T. J. Kamp, "Functional cardiomyocytes derived from human induced pluripotent stem cells," *Circ Res,* vol. 104, pp. e30-41, 2009.

[48] B. Liau, N. Christoforou, K. W. Leong, and N. Bursac, "Pluripotent stem cell-derived cardiac tissue patch with advanced structure and function," *Biomaterials,* vol. 32, pp. 9180-9187, 2011.

[49] S. Zlochiver, V. Muñoz, K. L. Vikstrom, S. M. Taffet, O. Berenfeld, and J. Jalife, "Electrotonic myofibroblast-to-myocyte coupling increases propensity to reentrant arrhythmias in two-dimensional cardiac monolayers," *Biophys J,* vol. 95, pp. 4469-4480, 2008.

[50] M. A. Beardslee, D. L. Lerner, P. N. Tadros, J. G. Laing, E. C. Beyer, K. A. Yamada, A. G. Kleber, R. B. Schuessler, and J. E. Saffitz, "Dephosphorylation and intracellular redistribution of ventricular connexin43 during electrical uncoupling induced by ischemia," *Circ Res,* vol. 87, pp. 656-62, 2000.

[51] I. Kostetskii, J. Li, Y. Xiong, R. Zhou, V. A. Ferrari, V. V. Patel, J. D. Molkentin, and G. L. Radice, "Induced deletion of the N-cadherin gene in the heart leads to dissolution of the intercalated disc structure," *Circ Res,* vol. 96, pp. 346-354, 2005.

[52] J. Li, M. D. Levin, Y. Xiong, N. Petrenko, V. V. Patel, and G. L. Radice, "N-cadherin haploinsufficiency affects cardiac gap junctions and arrhythmic susceptibility," *J Mol Cell Cardiol,* vol. 44, pp. 597-606, 2008.

[53] S. Rohr, "Cardiac Fibroblasts in Cell Culture Systems: Myofibroblasts All Along?," *J Cardiovasc Pharmacol,* vol. 57, pp. 389-99, 2011.

[54] J. J. Tomasek, G. Gabbiani, B. Hinz, C. Chaponnier, and R. A. Brown, "Myofibroblasts and mechano-regulation of connective tissue remodelling," *Nat Rev Mol Cell Biol,* vol. 3, pp. 349-363, 2002.

CHAPTER 5

SUMMARY, CONCLUSIONS, AND FUTURE WORK

5.1 Summary and Conclusions

In this research, an engineering approach was applied to develop and utilize tools and methods to produce engineered cardiac tissue, characterize both native and engineered cardiac tissue and test the hypothesis that the structure of age-matched native cardiac tissue serves as a representative control for engineered cardiac tissue. Three phases of research were conducted to address unmet needs in the field of cardiac tissue engineering.

In Chapter 2, a framework based on confocal microscopy was developed and utilized to characterize the microstructure in living cardiac tissue. Our developed framework includes a method for local dye delivery to living cardiac tissue, confocal microscopy techniques and image processing tools for the 3D analysis of myocyte geometry and the extracellular space. The developed framework for image processing and analysis served as a foundation for the research performed in Chapter 4. An important perspective of the developed imaging approach and analysis is the future application to diagnosis and patient-specific modeling of cardiac tissue structure.

In Chapter 3, a bioreactor capable of continuously monitoring force-displacement in engineered tissue was developed. Our bioreactor was designed with common cell

culture equipment and off the shelf and easily reproducible components. A full bill of materials and associated engineering drawings are available for our bioreactor. A novelty of the developed bioreactor is in the ability to nondestructively characterize tissue samples during development. Our ability to quickly design and implement custom bioreactors was key to the work described in Chapters 3 and 4. This capability comes at a low cost and high value due to using standard off the shelf cultureware as starting material.

In Chapter 4, approaches for confocal imaging and image analysis were developed and applied to quantitatively describe features of the native myocardium, focusing on myocyte geometry and spatial distribution of a major gap junction protein Cx43, in both engineered tissue and native tissue. We addressed the hypothesis that the application of environmental cues directs engineered tissue towards a phenotype resembling that of age-matched native myocardium. The results of the study support this hypothesis and reveal that electrical stimulation produces tissue with myocyte geometries and the spatial distributions of Cx43 which more closely resemble age-matched native myocardium as opposed to mature adult tissue.

5.2 Applications and Future Work

The developed bioreactor and imaging techniques have applications in engineering and characterizing stem-cell based cardiac tissue constructs. Induced pluripotent stem cells have been developed from human origin and resemble many features of embryonic stem cells [1, 2]. Induced pluripotent stem cells have the potential to differentiate into any cell type [3, 4] and have been specifically differentiated to

cardiomyocytes [5]. Although reprogramming efficiency is low and costly [6], enriched populations of cardiac myocytes can be collected through cell sorting techniques by recently identified cell surface markers [7]. However, the application of induced pluripotent stem cells to developing 3D tissue constructs is in its infancy [8]. The ability of induced pluripotent stem cells to form structural hallmarks of the native myocardium can be characterized and analyzed through the 3D confocal imaging and analysis techniques developed in this body of work.

An important perspective of the developed imaging approach and analysis is the application to diagnosis and patient-specific modeling of cardiac tissue structure. Fiber-optics based confocal imaging systems are being applied clinically for cellular-level characterization and detection of neoplasms [9-12]. The combination of our developed dye delivery approach with fiber-optics based confocal imaging and clinical catheterization techniques are a step towards extracting patient-specific microstructural data of cardiac tissue. These data, as well as the quantitative features extracted from native myocardium in the presented studies, can serve as definitions and inputs for computational modeling and simulation of cardiac tissue. Image data have been used to develop models of both physical and physiological properties of cardiac tissue [13, 14]. The 3D reconstructions of Cx43 distributions, myocytes and extracellular space can serve as inputs for mono- or bidomain models of cardiac conduction [15, 16] and discrete multidomain models that currently use idealized geometry [17]. Most models describe tissue properties with lumped parameters, homogenization approaches and analytical descriptions of microstructure or 2D image data [13, 18-20]. More realistic model inputs may create better predictive tools for analysis of cardiac function.

The imaging and tissue engineering approaches developed in this work can also be applied to better understand cell therapy strategies to treat heart disease. Cell therapy has been in the clinical arena since early 2000 with most studies reporting little to no change in cardiac function despite higher levels of success in small animal models [21, 22]. A key limitation of cell therapy is the lack of a mechanistic understanding of how the delivered cells improve cardiac function [23-25]. A better understanding of how the delivered cells improve function may aid in translating positive results found in small animal models to clinical application in human patients. In fact, a recent study reports on utilizing engineering cardiac tissue as a platform for studying the fate of undifferentiated embryonic stem cells [26]. This study along with others support the application that engineered cardiac tissue can serve as a substrate for studying disease progression and tissue development, therapeutic intervention, drug discovery and mechanisms of cell therapy [27-29].

The addition of mechanical [30-35] or electrical stimulation [36-38] has been shown to produce favorable structural features and functional performance of engineered cardiac tissue constructs. However, the application of both mechanical and electrical stimulation to engineered cardiac tissue has not been implemented. Although they have been applied independently, it is difficult to conclude if one is more beneficial or if the combination of both will outperform the application of just one. In one study, electrical stimulation was applied with the addition of verapamil, an L-type calcium channel blocker [36], and similar expression levels of Cx43 were maintained compared to the drug-free control. This result suggests that electrical stimulation, even without mechanical contraction, promotes formation of gap junction channels. Future work will

involve outfitting the developed bioreactor with electrical stimulation capabilities to enable the application of both mechanical and electrical stimulation and elucidate their combinational effects.

The force-sensing capabilities of the bioreactor allow for nondestructive characterization of mechanical properties during tissue culture. In principle, the developed confocal imaging and analysis of living tissue developed in the first phase of this research could be applied for the nondestructive characterization of microstructure in engineered cardiac tissue. Current analyses of structure and function are commonly constrained to endpoint analyses [39]. The combination of nondestructive characterization techniques for mechanical properties and structure can be used to obtain immediate feedback of tissue response and possibly adjust the specific mechanical or electrical conditioning regime to guide tissue towards a specific phenotype. Although applying confocal imaging to living tissue while maintaining sterility and not damaging tissue samples is technically challenging, strategies towards this direction are of interest in future work.

The approach for segmenting myocytes from 3D confocal images requires manual manipulation of triangle meshes. This is an inherently time consuming and tedious process. Automated methods for myocyte segmentation, such as region growing, are possible solutions to increase throughput for myocyte segmentation. Future work will involve developing algorithms and processing techniques to increase myocyte segmentation throughput. Finally, functional parameters such as the force of contraction, electrical conduction and excitation-contraction coupling in engineered tissue could be measured and compared to structural changes. The characterization of both structure and

function can be utilized to better understand and elucidate structure-function relationships in cardiac tissue.

5.3 References

[1] J. Yu, M. A. Vodyanik, K. Smuga-Otto, J. Antosiewicz-Bourget, J. L. Frane, S. Tian, J. Nie, G. A. Jonsdottir, V. Ruotti, and R. Stewart, "Induced pluripotent stem cell lines derived from human somatic cells," *Science,* vol. 318, pp. 1917-1920, 2007.

[2] K. Takahashi, K. Tanabe, M. Ohnuki, M. Narita, T. Ichisaka, K. Tomoda, and S. Yamanaka, "Induction of pluripotent stem cells from adult human fibroblasts by defined factors," *Cell,* vol. 131, pp. 861-872, 2007.

[3] Y. Shiba, K. D. Hauch, and M. A. Laflamme, "Cardiac applications for human pluripotent stem cells," *Curr Pharm Des,* vol. 15, pp. 2791-2806, 2009.

[4] S. S. Nunes, H. Song, C. K. Chiang, and M. Radisic, "Stem cell-based cardiac tissue engineering," *J Cardiovasc Transl Res,* vol. 4, pp. 592-602, 2011.

[5] J. Zhang, G. F. Wilson, A. G. Soerens, C. H. Koonce, J. Yu, S. P. Palecek, J. A. Thomson, and T. J. Kamp, "Functional cardiomyocytes derived from human induced pluripotent stem cells," *Circ Res,* vol. 104, pp. e30-41, 2009.

[6] K. Malliaras, M. Kreke, and E. Marbán, "The stuttering progress of cell therapy for heart disease," *Clin Pharmacol Ther,* vol. 90, pp. 532-541, 2011.

[7] N. C. Dubois, A. M. Craft, P. Sharma, D. A. Elliott, E. G. Stanley, A. G. Elefanty, A. Gramolini, and G. Keller, "SIRPA is a specific cell-surface marker for isolating cardiomyocytes derived from human pluripotent stem cells," *Nat Biotechnol,* vol. 29, pp. 1011-1018, 2011.

[8] B. Liau, N. Christoforou, K. W. Leong, and N. Bursac, "Pluripotent stem cell-derived cardiac tissue patch with advanced structure and function," *Biomaterials,* vol. 32, pp. 9180-9187, 2011.

[9] H. Inoue, S. Kudo, and A. Shiokawa, "Novel endoscopic imaging techniques toward in vivo observation of living cancer cells in the gastrointestinal tract," *Dig Dis,* vol. 22, pp. 334-337, 2004.

[10] S. Anandasabapathy, "Endoscopic imaging: emerging optical techniques for the detection of colorectal neoplasia.," *Curr Opin Gastroenterol,* vol. 24, pp. 64-69, 2008.

[11] M. Goetz, A. Hoffman, P. R. Galle, M. F. Neurath, and R. Kiesslich, "Confocal laser endoscopy: new approach to the early diagnosis of tumors of the esophagus and stomach," *Future Oncol.,* vol. 2, pp. 469-476, 2006.

[12] R. Kiesslich and M. F. Neurath, "Endoscopic confocal imaging," *Clin Gastroenterol Hepato,* vol. 3, pp. 58-60, 2005.

[13] F. B. Sachse, *Computational Cardiology: Modeling Of Anatomy, Electrophysiology, And Mechanics*. Heidelberg: Springer, 2004.

[14] A. J. Pullan, L. K. Cheng, and M. L. Buist, *Mathematically Modelling the Electrical Activity of the Heart: From Cell to Body Surface and Back Again*: World Scientific, 2005.

[15] B. H. Smaill, I. J. LeGrice, D. A. Hooks, A. J. Pullan, B. J. Caldwell, and P. J. Hunter, "Cardiac structure and electrical activation: Models and measurement," *Clin Exp Pharmacol Physiol,* vol. 31, pp. 913-919, 2004.

[16] D. A. Hooks, K. A. Tomlinson, S. G. Marsden, I. J. LeGrice, B. H. Smaill, A. J. Pullan, and P. J. Hunter, "Cardiac microstructure implications for electrical propagation and defibrillation in the heart," *Circ Res,* vol. 91, pp. 331-338, 2002.

[17] S. F. Roberts, J. G. Stinstra, and C. S. Henriquez, "Effect of nonuniform interstitial space properties on impulse propagation: a discrete multidomain model," *Biophys J,* vol. 95, pp. 3724-3737, 2008.

[18] J. P. Keener and J. Sneyd, *Mathematical Physiology*. New York: Springer, 1998.

[19] M. S. Spach, J. F. Heidlage, P. C. Dolber, and R. C. Barr, "Extracellular discontinuities in cardiac muscle: evidence for capillary effects on the action potential foot," *Circ Res,* vol. 83, pp. 1144-1164, 1998.

[20] M. S. Spach, J. F. Heidlage, R. C. Barr, and P. C. Dolber, "Cell size and communication: Role in structural and electrical development and remodeling of the heart," *Heart Rhythm,* vol. 1, pp. 500-515, 2004.

[21] P. Menasché, "Stem cell therapy for chronic heart failure. Lessons from a 15-year experience," *C R Biol,* vol. 334, pp. 489-496, 2011.

[22] P. Menasché, "Cardiac cell therapy: Lessons from clinical trials," *J Mol Cell Cardiol,* vol. 50, pp. 258-265, 2011.

[23] V. F. M. Segers and R. T. Lee, "Stem-cell therapy for cardiac disease," *Nature,* vol. 451, pp. 937-942, 2008.

[24] M. A. Laflamme and C. E. Murry, "Regenerating the heart," *Nat Biotechnol,* vol. 23, pp. 845-856, 2005.

[25] S. Dimmeler, A. M. Zeiher, and M. D. Schneider, "Unchain my heart: the scientific foundations of cardiac repair," *J Clin Invest,* vol. 115, pp. 572-583, 2005.

[26] J. Dengler, H. Song, N. Thavandiran, S. Massé, G. A. Wood, K. Nanthakumar, P. W. Zandstra, and M. Radisic, "Engineered heart tissue enables study of residual undifferentiated embryonic stem cell activity in a cardiac environment," *Biotechnol Bioeng,* vol. 108, pp. 704-719, 2011.

[27] D. D. Allen, R. Caviedes, A. M. Cárdenas, T. Shimahara, J. Segura-Aguilar, and P. A. Caviedes, "Cell lines as in vitro models for drug screening and toxicity studies," *Drug Dev Ind Pharm,* vol. 31, pp. 757-768, 2005.

[28] M. T. Donato, A. Lahoz, J. V. Castell, and M. J. Gomez-Lechon, "Cell lines: a tool for in vitro drug metabolism studies," *Curr Drug Metab,* vol. 9, pp. 1-11, 2008.

[29] Y. Zhang, R. B. Sekar, A. D. McCulloch, and L. Tung, "Cell cultures as models of cardiac mechanoelectric feedback," *Prog Biophys Mol Biol,* vol. 97, pp. 367-382, 2008.

[30] C. Fink, S. Ergun, D. Kralisch, U. T. E. Remmers, J. Weil, and T. Eschenhagen, "Chronic stretch of engineered heart tissue induces hypertrophy and functional improvement," *FASEB J,* vol. 14, pp. 669-679, 2000.

[31] H. Naito, I. Melnychenko, M. Didie, K. Schneiderbanger, P. Schubert, S. Rosenkranz, T. Eschenhagen, and W. H. Zimmermann, "Optimizing engineered heart tissue for therapeutic applications as surrogate heart muscle," *Circulation,* vol. 114, pp. I72-I78, 2006.

[32] W. H. Zimmermann, K. Schneiderbanger, P. Schubert, M. Didie, F. Munzel, J. F. Heubach, S. Kostin, W. L. Neuhuber, and T. Eschenhagen, "Tissue engineering of a differentiated cardiac muscle construct," *Circ Res,* vol. 90, pp. 223-230, 2002.

[33] R. K. Birla, Y. C. Huang, and R. G. Dennis, "Development of a novel bioreactor for the mechanical loading of tissue-engineered heart muscle," *Tissue Eng,* vol. 13, pp. 2239-2248, 2007.

[34] J. Zhuang, K. A. Yamada, J. E. Saffitz, and A. G. Kleber, "Pulsatile stretch remodels cell-to-cell communication in cultured myocytes," *Circ Res,* vol. 87, pp. 316-322, 2000.

[35] M. Gonen-Wadmany, L. Gepstein, and D. Seliktar, "Controlling the cellular organization of tissue-engineered cardiac constructs," *Ann NY Acad Sci,* vol. 1015, pp. 299-311, 2004.

[36] M. Radisic, H. Park, H. Shing, T. Consi, F. J. Schoen, R. Langer, L. E. Freed, and G. Vunjak-Novakovic, "Functional assembly of engineered myocardium by electrical stimulation of cardiac myocytes cultured on scaffolds," *Proc Natl Acad Sci U S A,* vol. 101, pp. 18129-18134, 2004.

[37] M. Radisic, V. G. Fast, O. F. Sharifov, R. K. Iyer, H. Park, and G. Vunjak-Novakovic, "Optical mapping of impulse propagation in engineered cardiac tissue," *Tissue Eng Part A,* vol. 15, pp. 851-860, 2009.

[38] N. Tandon, A. Marsano, R. Maidhof, L. Wan, H. Park, and G. Vunjak Novakovic, "Optimization of electrical stimulation parameters for cardiac tissue engineering," *J Tissue Eng Regen Med,* vol. 5, pp. e115-125, 2011.

[39] J. J. Pancrazio, F. Wang, and C. A. Kelley, "Enabling tools for tissue engineering," *Biosens Bioelectron,* vol. 22, pp. 2803-2811, 2007.